Gas-Vapor Bubble Dynamics
in Therapeutic Ultrasound

Wayne Kreider

A dissertation submitted in partial fulfillment of
the requirements for the degree of

Doctor of Philosophy

University of Washington

2008

Program Authorized to Offer Degree: Bioengineering

UMI Number: 3303380

INFORMATION TO USERS

The quality of this reproduction is dependent upon the quality of the copy submitted. Broken or indistinct print, colored or poor quality illustrations and photographs, print bleed-through, substandard margins, and improper alignment can adversely affect reproduction.

In the unlikely event that the author did not send a complete manuscript and there are missing pages, these will be noted. Also, if unauthorized copyright material had to be removed, a note will indicate the deletion.
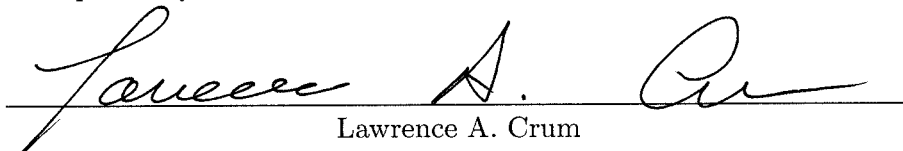
UMI®

University of Washington

Graduate School

This is to certify that I have examined this copy of a doctoral dissertation by
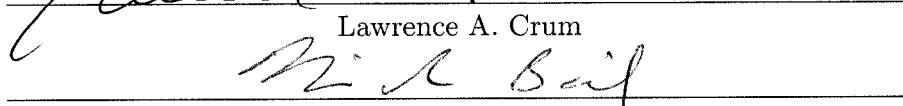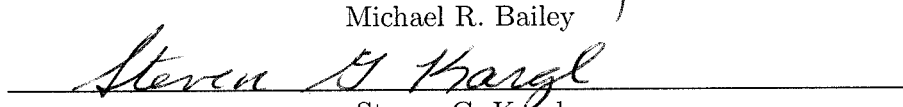
Wayne Kreider

and have found that it is complete and satisfactory in all respects,
and that any and all revisions required by the final
examining committee have been made.

Chair of the Supervisory Committee:

_____

Lawrence A. Crum

Reading Committee:

_____

Lawrence A. Crum

_____

Michael R. Bailey

_____

Steven G. Kargl

Date: _____3/17/2008_____

In presenting this dissertation in partial fulfillment of the requirements for the doctoral degree at the University of Washington, I agree that the Library shall make its copies freely available for inspection. I further agree that extensive copying of this dissertation is allowable only for scholarly purposes, consistent with "fair use" as prescribed in the U.S. Copyright Law. Requests for copying or reproduction of this dissertation may be referred to Proquest Information and Learning, 300 North Zeeb Road, Ann Arbor, MI 48106-1346, 1-800-521-0600, to whom the author has granted "the right to reproduce and sell (a) copies of the manuscript in microform and/or (b) printed copies of the manuscript made from microform."

Signature_____

Date_____3/17/2008_____

University of Washington

Abstract

Gas-Vapor Bubble Dynamics
in Therapeutic Ultrasound

Wayne Kreider

Chair of the Supervisory Committee:
Research Professor Lawrence A. Crum
Department of Bioengineering

In applications of therapeutic ultrasound such as shock wave lithotripsy (SWL) and high-intensity focused ultrasound (HIFU), cavitation and the associated bubble dynamics play an important role. Moreover, bubble dynamics have not been fully studied in the context of the large acoustic excitations, elevated temperatures, and gas-saturated conditions that characterize therapeutic ultrasound treatments. Because acoustic cavitation has been typically explored in the context of bubbles containing only non-condensable gases, relatively little is understood about the role of vapor under relevant conditions. Accordingly, the primary goal of this effort is to elucidate the role of vapor in the dynamics of gas-vapor bubbles. Given the large acoustic excitations of SWL and HIFU, the dynamics of violent inertial collapses are of particular interest.

To investigate the impact of vapor, both numerical modeling and experiments were utilized. The model was developed for a single, spherical bubble and was designed to capture behavior associated with the collapse and rebound of a gas-vapor bubble. Numerical difficulties in modeling violent collapses were addressed by using scaling principles to approximate the spatial gradients used for estimating heat and mass transport in both liquid and gaseous phases. Model predictions demonstrate thermal effects from vapor transport through the coupling of the saturated vapor pressure to temperature changes in the surrounding liquid. Also, the model suggests that vapor transport affects the dynamics mechanically when

vapor is diffusively trapped in the bubble interior. Moreover, predictions imply that the collapses of millimeter-sized lithotripsy bubbles are principally governed by the aforementioned mechanical effects. To test the model, collapses and rebounds of lithotripsy bubbles were experimentally observed using high-speed photography. Although bubble asymmetries added scatter to the data, experimental observations agree very well with the range of model predictions obtained with feasible length scales for mass diffusion in the bubble interior. Statistically significant variations observed in the experimental data imply that both temperature and dissolved gas concentration in the surrounding liquid affect mass diffusion inside the bubble. To complement experimental observations, bubble clusters in an incompressible liquid were modeled; simulations yielded insights related to bubble collapse times.

TABLE OF CONTENTS

LIST OF FIGURES

LIST OF TABLES

ACKNOWLEDGMENTS

DEDICATION

To my parents, Ruth and Harry Kreider, for their constant support of my return to school. Also, in completing this dissertation, I commemorate the lives lost in Norris Hall at Virginia Tech, where my engineering education began.

Chapter 1

INTRODUCTION

Therapeutic ultrasound comprises surgical techniques that use acoustic waves to effect changes in tissue. The therapeutic modalities of primary interest for this work are shock-wave lithotripsy (SWL) and high-intensity focused ultrasound (HIFU). In both modalities, acoustic energy is generated at a site remote from the treatment location and then focused to achieve very high intensities in a precise treatment volume. In SWL, the acoustic energy is delivered in a series of discrete shock waves that are used to break renal stones mechanically. For HIFU, acoustic waves are delivered to the treatment site more or less continuously, thereby heating the targeted tissue as the acoustic energy is continuously absorbed. Schematic illustrations of SWL and HIFU are provided in Figure 1.1.

Physical aspects shared by SWL and HIFU include the nonlinear propagation and focusing of acoustic waves, dissipation associated with this propagation, and cavitation.[1] In this context, the term 'cavitation' is considered to indicate the dynamic interaction of an acoustic field with gas bodies (*i.e.,* bubbles). Because therapeutic ultrasound typically involves large negative acoustic pressures, it is possible to excite very small gas bubbles. Moreover, observations of bubble activity during treatments are consistent with the literature related to decompression sickness in that sub-micron sized bubble nuclei are likely initiated and resolved in tissue under normal physiological conditions.[2]

Broadly, bubble dynamics are the focus of this effort. More specifically, cavitation behavior and the attendant thermodynamics are investigated under the intense acoustic fields characteristic of therapeutic ultrasound. In such acoustic fields, bubbles may grow to many times their original volume before collapsing violently. During such collapses, the inertia of the surrounding liquid controls the bubble motion; as this liquid mass flows quickly toward the bubble's geometric center, very high pressures and temperatures are produced
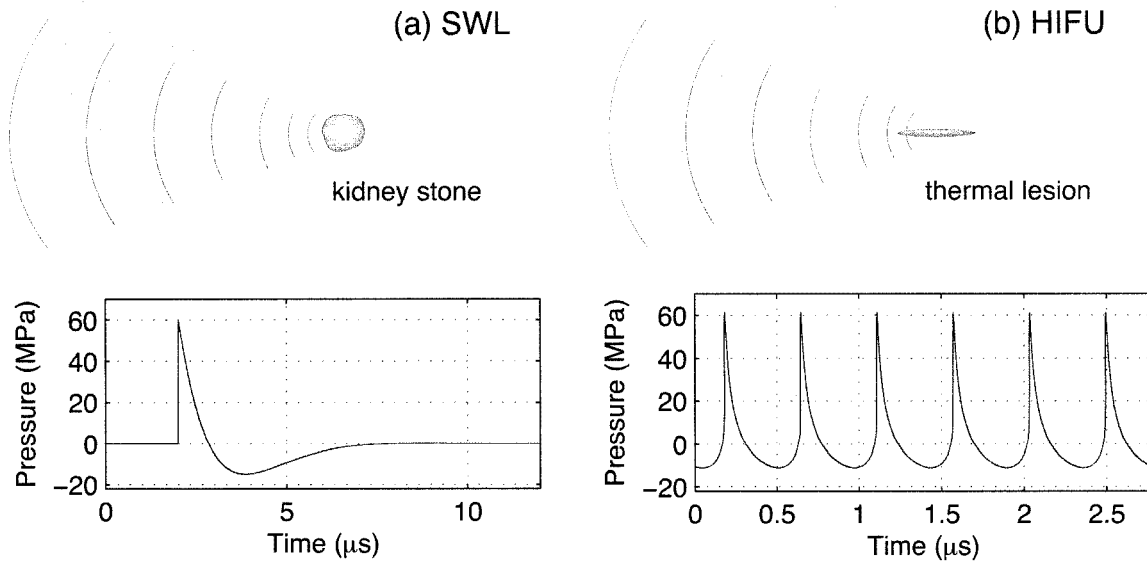
Figure 1.1. Schematic representations of the geometry and focal acoustics of (a) shock-wave lithotripsy and (b) high-intensity focused ultrasound.

inside the bubble. Because such inertial collapses (also called Rayleigh collapses[3]) represent a fundamental element of cavitation behavior in therapeutic ultrasound, they are the central topic of this dissertation. Moreover, because bubbles exposed to a lithotripter shock wave exemplify a pertinent and accessible subject for studying inertial cavitation, a primary focus of this dissertation comprises lithotripsy bubbles. Despite a particular focus here on individual bubble collapses and lithotripsy, the underlying bubble dynamics also apply to HIFU. For HIFU, the relevance of heat and vapor transport is readily apparent in that the therapeutic process involves rapid heating.

To provide a general context for this research, acoustics and bubbles in medical applications are discussed briefly below. Out of this context, further motivation for understanding bubble dynamics is identified and relevant literature are reviewed. Finally, the explicit scope of this effort is described.

1.1 General Background

1.1.1 Acoustics in Medicine

Many applications for acoustics in medicine have been developed in recent decades. Perhaps the most well known application is ultrasound (US) imaging. Other imaging techniques such as elastography and vibro-acoustography are also being developed to take advantage of specific acoustic properties. As discussed above, ultrasound can be used for therapeutic purposes in addition to diagnostics. Such therapies include SWL for the comminution of renal calculi and HIFU for treatment of tumors, hemostasis and possibly other surgical applications.[4] As reviewed by Bailey et al.,[1] these acoustic therapies involve various physical mechanisms that produce biological effects, including both localized heating and mechanical forces related to cavitation.

In considering SWL and HIFU, note the variety of treatment strategies denoted by these terms. In SWL, the goal of treatment is always to generate high mechanical stresses in renal stones, thereby breaking them into smaller pieces. These stresses may be induced by either the incident shock wave, the resulting cavitation activity, or both. In contrast, HIFU treatments may involve the utilization of various physical mechanisms to produce different physical and biological effects. For instance, treatment of tumors with HIFU relies mainly upon the generation of regions of thermal necrosis within the tumor.[5] However, other treatments have been designed to utilize only mechanical effects associated with cavitation to disrupt and homogenize tissue.[6,7] Meanwhile, using HIFU for hemostasis may involve some combination of thermal and mechanical effects.[8,9] Given the broad range of therapeutic medical applications, many of which explicitly seek either to utilize or avoid cavitation, it is clearly desirable to obtain a fundamental understanding of the related bubble dynamics.

1.1.2 Cavitation in Therapeutic Ultrasound

Bubbles in therapeutic ultrasound are of particular interest because they provide a very efficient means for reflecting acoustic energy and/or localizing mechanical effects. Depending upon the application, the physical interaction of bubbles with an intense sound field can be either beneficial or harmful. Below, both positive and negative effects of cavitation are

cited for illustrative purposes. Altogether, these examples demonstrate the practical utility of understanding how cavitation bubbles can reflect or concentrate mechanical and thermal energy.

Starting with undesirable effects, note that cavitation has been linked to renal injury in SWL.[10–12] Although the specific physical mechanisms that cause the observed vascular damage remain unclear, the collective data seem to indicate that cavitation plays a role. Aside from their association with unintended tissue injury, bubbles have also been shown to significantly distort the acoustic field delivered during both lithotripsy and HIFU treatments.[13–15] Because the field distortions are typically unpredictable, such effects are inherently troublesome. In SWL, a slower rate of shock-wave delivery produces fewer bubbles, thereby minimizing distortion of the focal waveform and enabling more efficient treatments.

While acoustic reflection and energy localization can be harmful, these same physical characteristics of bubbles can also be exploited. For instance, the reflective characteristics of bubbles may be utilized to assist in the targeting and/or dosimetry of HIFU with ultrasound imaging.[16,17] In addition to diagnostic functions, bubbles may also be utilized to contribute to the therapeutic effect. Specific examples include the following: improvement of gene transfection through the piercing of cell membranes,[18] enhancement of local heating for thermal therapies,[19,20] erosion of kidney stones,[21,22] and targeted erosion of tissue.[6,23] In further illustration of the beneficial role of bubbles, contrast agent microbubbles originally developed for ultrasound imaging are increasingly being adopted for therapeutic purposes.[9,24]

Given that bubbles play a significant role in therapeutic ultrasound, understanding the fundamental dynamics of bubbles excited by high-amplitude acoustic pressures remains a topic of significant research interest. Although cavitation behavior is very diverse across the aforementioned spectrum of therapeutic applications, a common aspect is the fundamental manner in which bubbles localize the mechanical energy of a strong sound field. It has been demonstrated that strongly excited bubbles radiate large acoustic pressures[25] and induce thermal effects in the surrounding medium.[20,26] These effects and others are dictated by the bubble motion and its implicit thermodynamics. Further demonstrating the intimate coupling between cavitation activity and the local thermodynamic state of the surroundings,

recent work on nonlinear heating mechanisms in HIFU has demonstrated that bubbles can be excited to superheated temperatures within milliseconds.[27]

In the above discussion of the relevance of bubble activity during therapeutic ultrasound, it is apparent that the thermodynamics associated with bubble oscillations are of direct import. Thus, understanding the pertinent dynamics requires consideration of the transport of heat and mass to/from the bubble (including both vapor and non-condensable gases). While a wealth of literature exists on the dynamics of gas and vapor bubbles, the fundamental physics under conditions pertinent to SWL and HIFU have not been fully explored. Although pertinent fluid mechanics equations can be formulated in a straightforward manner to model these conditions, direct numerical computations remain intractable when large acoustic excitations are present. Moreover, careful experiments to elucidate basic mechanisms under such extreme conditions are difficult. Further discussion of the relevant literature on bubbles dynamics is continued in the next section.

1.2 Literature Review

In the following sections, the research literature are reviewed with a particular focus on bubble modeling. Because the most useful starting point in developing a new model is the most recent literature, the subsequent review focuses largely on more recent work. Given the breadth of historical work on cavitation and bubble dynamics, the review contained in this section is certainly not comprehensive. However, additional literature can be found in the references of papers cited below.

1.2.1 Bubble Modeling Approaches

Given the complexity associated with the general problem of acoustic cavitation, it is insightful to first discuss methods that have been developed to model and understand bubble dynamics. For the most general case of cavitation, conservation of mass, momentum, and energy must be enforced in both liquid and gaseous phases. Moreover, liquid and gas regions must be considered to share a moving boundary across which heat and mass are exchanged. The most complete models require solution of the governing partial differential equations (PDEs) in both time and space. However, owing to the coupling of dynamics

across different temporal and spatial scales,[28] direct numerical solution of the full PDEs can be problematic. Hence, most models in the literature address bubble dynamics under simplifying assumptions.

A common assumption used to study bubble dynamics is geometric symmetry. If a single bubble remains spherical, equations of continuity and momentum for an incompressible liquid may be integrated to yield an ordinary differential equation (ODE) for the bubble radius as a function of time.[3,29] To close such a model formulation, it is then necessary only to specify how the pressure inside the bubble varies with its radius. Although liquid compressibility and other more complicated phenomena are often included, any such model that describes the underlying radial motion with a single ODE may be generically termed a 'Rayleigh-Plesset' model. As discussed further in Section 1.2.2 below, Rayleigh-Plesset models can successfully capture the basic features of very violent collapses despite their simplicity. Accordingly, individual spherical bubbles are the primary focus of the following discussion of the literature.

1.2.2 Modeling Limitations

As already mentioned, direct numerical simulation of the governing PDEs for bubble motion remains numerically intractable in many instances. Although several groups have successfully implemented direct simulations for inertial collapses,[30-32] difficulties remain for many of the conditions applicable to therapeutic ultrasound. More specifically, very steep spatial gradients develop during violent collapses. As noted by Preston,[32] the presence of such steep gradients requires the use of extremely small time steps to maintain stability during numerical integration. Ultimately, these calculations tend to become computationally intractable when micron-sized bubbles are excited by negative pressures on the order of a few bars.[32] Given that SWL and HIFU typically involve negative pressures on the order of tens of bars, direct simulations are generally not feasible.

Complementing the more complicated models and their numerical limitations, simpler models can be used to elucidate basic behaviors. As demonstrated by Lin et al.,[33] Rayleigh-Plesset models that assume a uniform pressure inside the bubble can capture the basic

features of the dynamics. Accordingly, such reduced-order models have been successfully used to investigate the inertial collapses of both sonoluminescence bubbles[34,35] and SWL bubbles.[36]

1.2.3 Bubble Dynamics in Therapeutic Ultrasound

The brief description of modeling approaches and limitations provided above is applicable to bubble dynamics in general. In this subsection, the relevant literature are explicitly related to understanding cavitation in therapeutic ultrasound. First, single-bubble sonoluminescence is considered. The intense interest in sonoluminescence during the 1990s led to many efforts for modeling violent collapses and experimentally testing these models. As a result, this literature is relevant because it represents a unique body of knowledge regarding the physics of inertial collapses. Similarly, the collapses of laser-induced bubbles have been studied carefully with both theory and experiments. Two relevant papers on laser-induced bubbles are discussed next. Finally, efforts to understand bubble dynamics under both HIFU and SWL conditions are reviewed and an overarching summary of the literature is provided.

Single-Bubble Sonoluminescence

In the study of single-bubble sonoluminescence, typical conditions involve a 5 μm bubble driven with acoustic pressures of about 1 bar and acoustic frequencies near 20 kHz. The 5 μm bubble expands to roughly ten times its initial radius and collapses violently during each acoustic cycle. High temperatures generated during collapse lead to the characteristic light emission. Because light emission can be physically related to temperature, models developed to understand this phenomenon evolved to address the thermodynamics of collapse.[37–40] Ultimately, these models included compressibility of the liquid and gas phases, heat transport to/from the bubble, mass diffusion, non-equilibrium evaporation and condensation of water at the liquid-gas interface, and chemical reactions in the gas phase.

Later sonoluminescence models became sophisticated enough to explain experimental observations. Perhaps the most comprehensive model was implemented by Storey and Sz-

8

eri.[39] Notably, they were able to capture heat transfer to/from the liquid phase of a violently collapsing bubble by using a boundary-layer approximation to the energy equation in the liquid. As described in more detail by Vuong and Szeri,[31] a key component of the model formulation was the inclusion of pressure inhomogeneities in the gas. Such consideration of shock waves in the gas phase enabled formulation of a numerically stable model for violent bubble collapses in the presence of diffusive transport. Toegel and Lohse[40] also included pressure inhomogeneities in their model, though they neglected the energy equation in the liquid. Moreover, they utilized reduced-order models for diffusive transport. Ultimately, this model was able to effectively predict the behavior of sonoluminescence bubbles across a range of experimental test conditions.[40]

As models for single-bubble sonoluminescence were refined to explain experimental observations, a very relevant general conclusion was reached. Although the specific numerical results of a given model depended upon details such as the equation of state in the gas phase and the uniformity of pressure inside the bubble, less complicated model formulations were able to capture the qualitative features of bubble collapse.[33,39] Moreover, several successful reduced-order models were presented.[34,35,41] A key aspect of these reduced-order models involved estimation of heat and mass transport behavior based upon characteristic length and time scales of the bubble motion. While Yasui[41] implicitly defined length scales by assuming temperature distributions in the surrounding liquid, others explicitly defined time and length scales for heat and mass transfer in the gas phase.[34,35,40]

Although the later models for single-bubble sonoluminescence do not consider temperature changes in the surrounding liquid, the approach of defining explicit length and time scales in a reduced-order model provides an appealing framework. Even though a more sophisticated approach that includes heat transfer in the liquid was developed by Szeri and others,[31,39] such an approach poses significant computational challenges. Hence, in the context of the range of acoustic and physiological conditions pertinent to HIFU and SWL, reduced-order models hold appeal for investigating the physical mechanisms that are most relevant to bubble dynamics in therapeutic ultrasound.

Collapse and Rebound of Laser-Induced Bubbles

If a pulsed laser is focused to a point in water, optical breakdown can be induced. Although rather complicated physics describe the optical breakdown and subsequent plasma recombination, these processes can ultimately produce a spherical bubble that grows to a maximum size on the order of millimeters before collapsing.[42,43] Such laser-induced bubbles have proven useful for studying the collapses of bubbles near solid boundaries because the location of the bubble can be precisely controlled with the laser.

Vogel and Lauterborn studied the collapse and rebound of laser-induced bubbles with maximum radii between 1 and 5 mm.[43,44] In particular, they analyzed these collapses from a macroscopic perspective, using the maximum radius attained before and after collapse to assess the total amount of energy lost. Using a combination of acoustical and optical techniques, they also measured the pressures radiated by collapsing bubbles. For spherical collapses, it was found that bubbles lose about 84% of their total energy during collapse. In addition, pressure measurements indicated that about 73% of the *lost* energy was radiated acoustically. Overall, this work provides excellent insight into the mechanisms for energy conversion in the collapse of millimeter-sized bubbles. However, it does not elucidate how these mechanisms might be affected by collapses under different conditions that may better represent therapeutic ultrasound.

In more recent work, the collapses and rebounds of laser-induced bubbles were investigated analytically and experimentally.[42] The model proposed in this work utilizes a unique formulation, but essentially includes the same physical characteristics described above for models of sonoluminescence bubbles. It is noteworthy that this model was successfully implemented to simulate the very violent collapses of millimeter-sized bubbles. A key conclusion of this work was that even though the bubble may initially be composed mainly of water vapor, the presence of a small amount of non-condensable gas greatly affected the resulting rebounds. Despite this noted sensitivity, the authors argue that the diffusion of dissolved gases into the bubble during its initial expansion are not sufficient to significantly affect the model predictions. Overall, this work represents an extension of models proposed for sonoluminescence to the inertial collapses of larger bubbles. However, key aspects of the

model as it might be applied to SWL or HIFU were not tested experimentally—*e.g.*, sensitivity to dissolved gases in the surrounding liquid as well as thermal transport behaviors.

HIFU Bubbles

In the context of this dissertation, HIFU describes a focused acoustic field with peak rarefactional pressures typically in the range of 1–15 MPa and acoustic frequencies from roughly 0.5–10 MHz. Although many researchers have reported experimental results that describe evidence of cavitation during application of HIFU, relatively few have explicitly explored the physical mechanisms that characterize the bubble activity. For example, acquired hydrophone measurements imply the presence of inertial cavitation under *in vivo*, *ex vivo*, and *in vitro* conditions during HIFU.[6,19,45] However, characterization of the bubble motions as inertial does not elucidate the mechanisms that govern the dynamics. To illustrate, inertial collapses can be observed both in vapor bubbles and in gas bubbles, even though the underlying mechanics of these types of bubbles are quite different.

An active area of HIFU research that does include mechanistic modeling involves bubble-mediated heating. Holt and Roy[19] experimentally discovered a correlation between cavitation activity and enhanced heating during HIFU. They attributed this behavior to acoustic radiation and viscous dissipation from oscillating bubbles. If controllable, this phenomenon suggests a means for improving HIFU treatment protocols; hence efforts to optimize and control bubble-mediated heating have continued.[20] As a part of this work, a model was developed to identify relevant bubble sizes by estimating thresholds at which shape instabilities and rectified diffusion would occur during HIFU.[46] However, the bubble model used in this work did not account for phase change and its attendant thermal effects. Because vapor was demonstrated to be important in other inertially collapsing bubbles, it is unclear how well such a model can capture the essential behavior of HIFU bubbles.

In related research, another group has utilized a more complete model that accounts for vapor dynamics to investigate therapeutic applications. Matsumoto et al.[26] analyzed single bubbles as well as bubble clouds and assessed the potential of bubbles to transduce energy from the acoustic excitation into thermal energy. They found that thermal transport from

the bubble (*i.e.*, both thermal conduction and the latent heat of vapor condensation) provides as much energy to the surrounding liquid as acoustic radiation and viscous dissipation. Though this work provides mechanistic insights, only modest excitation amplitudes on the order of 0.1 MPa were considered. From personal communication with Shin Yoshizawa, higher excitation amplitudes were not considered due to numerical difficulties similar to those described above in Section 1.2.2.

Lithotripsy Bubbles

In lithotripsy, cavitation is believed to contribute to both tissue injury[12] and stone fracture.[21] Accordingly, cavitation during lithotripsy remains an active area of research. For convenience, this research is loosely categorized here according to its focus on either single bubbles or bubble clusters. Because the research on bubble clusters typically examines the effects of bubble interactions rather than the explicit thermodynamics of bubble motion, it is not discussed further here.

As for single bubbles, some recent work has considered the effects of asymmetry on violent collapses in SWL. Johnsen et al.[47] and Sankin et al.[48] have looked at shock-induced bubble collapses. In research on other asymmetric effects, the dynamics of bubbles constrained by vessels have been explored.[49,50] Although these studies provide insight into real collapses that are not ideally symmetric, they focus only on the shape of the liquid-gas interface. Because the models used by Johnsen et al.[47] and by Qin et al.[50] do not include the details of heat and mass transport as described in Section 1.2.3, they cannot provide additional insight thereof.

Lastly, several modeling and experimental efforts have sought to characterize the spherical dynamics of individual bubbles exposed to a lithotripter shock wave. Church[51] introduced a numerical approach for calculating the diffusion of non-condensable gases into lithotripsy bubbles. Later, Sapozhnikov et al.[10] used this same approach to explore the effects of shock repetition rate on bubbles. Calculations along with experimental measurements suggested that gas diffusion into micron-sized gas bubbles excited by a single lithotripter shock wave can produce gas bubbles with equilibrium radii on the order of tens

of microns.

In addition to exploring gas diffusion, some researchers have studied the behavior of vapor in lithotripsy bubbles. Based on the fundamental works of Szeri, Matula et al.[36] implemented a reduced-order model based on scaling principles and compared model predictions with direct measurements of the bubble radius. They found that a significant amount of vapor was likely 'trapped' inside the bubble during collapse. Such vapor trapping is caused by diffusion between non-condensable gases and vapor, a process which limits the rate of vapor condensation. In addition, Matula et al.[52] recorded sonoluminescence data from lithotripsy bubbles and obtained results consistent with the vapor trapping analysis.

1.2.4 Summary Discussion

From a review of literature pertinent to the thermodynamics of violent bubble collapses, a consistent theme emerges. In particular, the dynamics of vapor have been implicated in significantly affecting collapses related to sonoluminescence bubbles, laser-induced bubbles, and lithotripsy bubbles. As for HIFU, Matsumoto et al.[26] have considered gas-vapor bubbles at relatively low excitation levels. However, no available models have simulated the dynamic interaction of vapor with bubble motion in the context of megapascal acoustic pressures and megahertz frequencies. It is reasonable to expect that vapor does play a role for HIFU bubbles, especially when boiling may occur within milliseconds.[27,53,54] Also, with regard to bubble-enhanced heating during HIFU, vapor at elevated temperatures is thought to soften bubble collapses and reduce the heating effect.[55] Early components of this effort sought to begin a more thorough consideration of the role of vapor in HIFU bubbles.[56,57]

For a complete evaluation of the impact of vapor dynamics, both mass transport and attendant heat transfer processes must be considered. Heat and mass transport of vapor are coupled through the enthalpy of vaporization as well as through the dependence of the saturated vapor pressure on the liquid temperature. While the mass transport of vapor is primarily governed by the kinetics of phase change, diffusive effects can also become important if non-condensable gases are also present. Generally speaking, these diffusive effects can limit the rate of vapor condensation; such trapping of additional mass inside the

bubble during collapse alters both the pressure inside the bubble and the damping from acoustic radiation.

Despite overall research progress that indicates the importance of vapor in inertially controlled bubble dynamics, relatively little attention has been given to vapor in the context of therapeutic ultrasound. As described in more detail in the ensuing section, the goal of this effort was to elucidate the fundamental behavior of violent bubble collapses under ambient conditions that include high levels of dissolved gases and elevated temperatures. Such ambient conditions are directly relevant to SWL and HIFU treatments.

1.3 Scope

In this effort, the underlying hypothesis is that vapor transport plays an important role in the bubble dynamics characteristic of therapeutic ultrasound. In much related work, acoustic cavitation has been studied in terms of gas-bubble dynamics; moreover, this paradigm has often been used to describe the dynamics of bubbles in the context of SWL and HIFU. To test this paradigm, the main focus of this effort is an elucidation of the impact of vapor using a numerical model in conjunction with experiments.

In the exploration of bubble dynamics relevant to SWL and HIFU, it is instructive to categorize the effects of vapor transport as either thermal or mechanical. Thermal effects describe the coupling of temperature at the liquid-gas interface with the vapor pressure inside the bubble. In contrast, mechanical effects involve the total pressure achieved during an inertial collapse and the associated loss of energy to acoustic radiation. Because diffusion among vapor and non-condensable gas molecules can effectively limit condensation and trap vapor during collapse, vapor transport can mechanically alter the evolution of pressure inside a collapsing bubble. With this categorization, the scope of this dissertation is explicitly set forth below.

To investigate gas-vapor bubble dynamics in therapeutic ultrasound, this effort includes three components: (1) development, implementation, and benchmarking of a model for inertial collapses and rebounds of individual, spherical bubbles; (2) collection of experimental data regarding lithotripsy bubble collapses to test model predictions; and (3) analysis of lithotripsy test conditions to aid interpretation of experimental observations in the context

of model predictions. The physical model is described in Chapter 2 and enables interpretation of both thermal and mechanical behaviors associated with vapor transport during a single collapse and rebound. The model explicitly assumes a single, spherical bubbles that undergoes collapse and rebound without consideration of chemical reactions inside the bubble or asymmetries that could lead to bubble fragmentation. Details of the model's numerical implementation are included in Chapter 3, while model predictions and comparisons with the available literature are presented in Chapter 4. Beyond the modeling effort, the ensuing three chapters discuss experiments used to test model predictions with regard to the mechanical impact of vapor transport. Chapters 5 and 6 respectively describe the setup and results from experimentally observing the collapses and rebounds of lithotripsy bubbles. As an outgrowth of these experiments, analyses of the test conditions were performed in order to relate experimental observations to model predictions. These analyses are pertinent to research on lithotripsy and are summarized in Chapter 7. Lastly, Chapter 8 provides a summary and conclusions.

Chapter 2

BUBBLE MODEL

As mentioned in the introduction, the modeling approach considered here involves single, spherical bubbles. In addition, considering the difficulties associated with direct numerical simulation of bubbles excited by large acoustic pressures, we adopt a reduced-order model based on scaling principles, as has been done previously.[34–36,41] In these published models, time and length scales were explicitly identified for heat and mass transport inside the bubble. However, no corresponding scales were implemented for temperature changes in the liquid. While Yasui[41] indirectly used similar ideas to simulate temperature changes in the liquid, his assumed temperature distributions included their own singularities and a fitting parameter that is hard to interpret physically. After initial implementation of a version of Yasui's model that did provide insights for guiding further work, a new scaling approach for thermal behavior in the liquid was derived.

The model developed and implemented in this effort includes the following components: liquid compressibility, heat transport in the gas and liquid phases, and mass transport of both vapor and non-condensable gases. To describe the model in this chapter, we first present fundamental governing equations for completeness and for definition of notation. Then, the explicit bubble model is defined, including a detailed discussion of the scaling principles used to estimate heat and mass transport.

2.1 Fundamental Equations

In this section, we state the fundamental equations—conservation of mass, momentum, and energy; equations of state; and pertinent physical laws for heat and mass transfer. These relations are presented below with a notation and format that are convenient to the ensuing definition of the reduced-order bubble model.

2.1.1 Conservation Equations in the Liquid

Regarding the basic conservation principles, equations can be written for any fluid flow and are thus applicable to both the liquid and gaseous phases involved in cavitation. Accordingly, the basic modeling approach is to apply the conservation equations separately to the liquid and gaseous phases while considering the bubble wall as a moving boundary that separates the flow regimes. Moreover, the fundamental conservation equations can be expressed either in differential form for any arbitrary point in the flow or in integral form for a defined control volume.

In this section, the differential forms for conserving mass, momentum, and energy in the liquid are presented in a form that is typically used in deriving a radial equation of motion for a bubble. For conservation of mass, the following continuity relation holds:

$$\frac{D\rho}{Dt} + \rho\left(\nabla \cdot \mathbf{u}\right) = \frac{\partial \rho}{\partial t} + \nabla \cdot \left(\rho\mathbf{u}\right) = 0 \tag{2.1}$$

In this relation, ρ is the liquid density, t is time, $\mathbf{u}$ is the liquid velocity vector, and the operator $D/Dt \equiv \partial/\partial t + (\mathbf{u} \cdot \nabla)$ represents a material derivative. Similarly, conservation of momentum can be expressed in vector form as

$$\rho\frac{D\mathbf{u}}{Dt} = \left(\nabla \cdot \boldsymbol{\tau}\right) + \mathbf{f} \tag{2.2}$$

where $\boldsymbol{\tau}$ is the complete stress tensor of the liquid and $\mathbf{f}$ is the net body force exerted per unit volume. A convenient alternate form of the momentum equation is obtained by assuming a constitutive relation consistent with a Newtonian fluid and neglecting viscous effects. In this manner, we obtain Euler's equation in the liquid as

$$\rho\frac{D\mathbf{u}}{Dt} + \nabla p = \mathbf{f} \tag{2.3}$$

where p is pressure. Lastly, conservation of energy in the liquid is described by the heat equation

$$\rho\frac{De_i}{Dt} = -p\left(\nabla \cdot \mathbf{u}\right) - \left(\nabla \cdot \mathbf{q}\right) + \phi \tag{2.4}$$

where e_i is the internal energy per unit mass, $\mathbf{q}$ is the heat flux vector per unit area, and ϕ represents viscous dissipation.[58]

For convenient reference in the derivation of a radial equation of motion, we rewrite the conservation equations for mass and momentum after assuming spherical symmetry and neglecting body forces such as gravity:

$$\frac{\partial \rho}{\partial t} + \frac{1}{r^2}\frac{\partial \left(r^2 \rho u_r\right)}{\partial r} = 0 \tag{2.5}$$

$$\frac{\partial u_r}{\partial t} + u_r\frac{\partial u_r}{\partial r} + \frac{1}{\rho}\frac{\partial p}{\partial r} = 0 \tag{2.6}$$

Here, r is the radial coordinate and u_r represents the radial component of the velocity vector. As noted by Prosperetti and Lezzi,[59] the state of the liquid may be expressed in terms of a single thermodynamic variable if thermal effects in the liquid remain small. Hence, an additional equation for thermal energy is not needed to derive the various Rayleigh-Plesset equations for radial bubble motion. As noted by Hao and Prosperetti,[60] such radial equations are well justified even for vapor bubbles under many boiling conditions. Moreover, Storey and Szeri[39] confirmed his justification for sonoluminescence bubbles.

2.1.2 Conservation Equations in the Bubble Interior

As shown by Prosperetti et al.,[61] enforcing an energy balance on the bubble contents is superior to the invocation of a polytropic relation. To this end, we note that the conservation equations from the previous section are also applicable to the gas inside the bubble. However, it is convenient here to recast the equations in integral form to capture the energy of the bubble as a whole.

Along these lines, we first recognize Prosperetti's analysis from which we can treat the pressure inside the bubble as uniform and ignore the momentum equation in the gas.[61] The soundness of this assumption for violent collapses has been considered and confirmed by others.[33] Next, we integrate equations (2.1) and (2.4) over the bubble volume. Using the Leibniz Rule to move the time derivative outside the integral and using the divergence theorem to convert the volume integral to a surface integral, we obtain a new form for the

18

continuity equation:

$$\frac{\partial}{\partial t} \int_V \rho_m \, dV - \rho_m \, \dot{V} = -\int_A \rho_m \, \mathbf{u} \cdot d\mathbf{A} \tag{2.7}$$

Here, the overdot indicates a time derivative, V is the bubble volume, $\mathbf{A}$ is the bubble surface area with outward-pointing normal, and ρ_m is the molar density of gases inside the bubble. If the viscous dissipation term is ignored, integration of the heat equation (2.4) yields

$$\rho_m \frac{\partial}{\partial t} \int_V e_i \, dV - \rho_m \, e_i \, \dot{V} = -\int_A \mathbf{q} \cdot d\mathbf{A} - \int_A p_i \, \mathbf{u} \cdot d\mathbf{A} \tag{2.8}$$

where p_i is the pressure inside the bubble. Note that in writing Equation (2.8) we have used the earlier assumption that pressure is spatially uniform inside the bubble volume V. In addition, we follow an assumption used in reduced-order models by taking other thermodynamic variables to be uniform inside the bubble, except within a boundary layer at the liquid-gas interface.[34,36] Considering spatial uniformity in addition to spherical symmetry, we can directly evaluate the integrals in the previous two equations. Given that the molar density is defined as $\rho_m \equiv n/V$ where n is the total number of moles of gas, the integral form of the continuity equation (2.7) may be solved to determine the radial gas velocity at the bubble wall

$$(u_r)_{r=R} = \dot{R} - \frac{R}{3}\frac{\dot{n}}{n} \tag{2.9}$$

where R denotes the bubble radius. Using this expression for the gas velocity at $r = R$, we evaluate the integrals in Equation (2.8) to obtain

$$\rho_m \, \dot{e}_i = -\frac{3}{R} \, q_r + p_i \left(\frac{\dot{n}}{n} - \frac{3\dot{R}}{R} \right) \tag{2.10}$$

where q_r is the radial heat flux out of the bubble. Below, this equation is used as a starting point for enforcing an energy balance on the contents of the bubble.

2.1.3 Equation of State in the Liquid

In addition to the conservation principles discussed above, description of the pertinent physics also requires equations of state for both liquid and gaseous phases. For liquids, we

utilize a modified form of the Tait equation to relate thermodynamic variables as follows:[62]

$$p = p_0 + \frac{1}{b\,\Gamma} \left[\left(\frac{\rho}{\rho_0} \right)^{\Gamma} - 1 \right] \tag{2.11}$$

In this equation, p is the pressure in the liquid, ρ is the density, Γ and b are empirical constants, and liquid properties at a reference state are denoted by the '0' subscripts. For consistency, we define b in terms of the ambient sound speed c_0 as follows:

$$b = \frac{1}{\rho_0 c_0^2} \tag{2.12}$$

From data presented for water over a range of temperatures,[62] we select $\Gamma = 6.5$ for this work.

2.1.4   Equation of State for Gases Inside the Bubble

Even though vapor and non-condensable gases are treated separately with regard to transport in/out of the bubble, they are treated collectively to express a pressure-volume-temperature relationship. In selecting an equation of state for the bubble interior, we adopt a form of the ideal gas equation

$$p_i = z \rho_m \mathcal{R} \theta \tag{2.13}$$

where p_i is pressure inside the bubble, ρ_m is molar density, θ is temperature, and $\mathcal{R}$ is the universal gas constant. Accordingly, the compressibility factor z represents the deviation from ideal behavior and is unity for an ideal gas. The Redlich-Kwong equation of state as adapted in 1972 by Soave was used to estimate z as the root of a cubic equation under given thermodynamic conditions.[63] However, it was found that inclusion of non-ideal gas behavior led to numerical difficulties in many of the violent collapses investigated in this work. In addition, other researchers have found that even though the equation of state affects quantitative results for modeling sonoluminescence bubbles, the underlying physical trends are insensitive to the equation of state.[38]

Because the model developed here is approximate in nature due to its reliance on scaling principles, the compressibility factor z was dropped. For convenience in defining notation, we now rewrite the ideal gas equation in several forms:

$$p_i = \rho_m \mathcal{R}\theta = \frac{n\mathcal{R}\theta}{V} = \frac{Nk_B\theta}{V} \tag{2.14}$$

In the above expressions, V is the bubble volume, $\rho_m = n/V$ is again the molar density, n is the total number of moles of gas, $N = nN_A$ is the number of gas molecules, and N_A is Avogadro's number. Accordingly, $k_B = \mathcal{R}/N_A$ is the Boltzmann constant.

2.1.5 Heat and Mass Diffusion

The equations that describe both heat and mass diffusion possess an identical form. Accordingly, we describe these equations for a generic scalar property ϕ. The fundamental empirical relation that describes diffusive processes is often called Fick's Law for mass diffusion and Fourier's Law for heat conduction. This relation may be expressed as

$$\mathbf{J} = -K\,\nabla\phi \tag{2.15}$$

where $\mathbf{J}$ is a flux per unit area of the scalar quantity ϕ, K is a constant, and $\nabla\phi$ is the gradient of temperature or mass concentration. For diffusion processes in a moving fluid, the physical behavior described by Equation (2.15) can be generalized to account for convection in the fluid and time dependent changes in ϕ. The resulting equation can be written as[58]

$$\frac{D\phi}{Dt} = \kappa\,\nabla^2\phi \tag{2.16}$$

where D/Dt is again a material derivative, ∇^2 is the Laplace operator, and the diffusivity κ has been assumed constant in time and space.

2.1.6 Solubility of Gases in Water

Another empirical relation is typically used to describe the equilibrium dissolution of a gas in a liquid. As such, Henry's law relates the partial pressure of a given gaseous component

p_j to its molar concentration x_j in the adjacent liquid as

$$p_j = \mathcal{H}_j\, x_j \qquad (2.17)$$

where $\mathcal{H}_j$ is Henry's constant for the given solute and solvent. For oscillating bubbles, the pressure inside the bubble is usually calculated as a part of the numerical solution of the dynamics. Then, it is typically assumed that the concentration of any dissolved gas species in the liquid at the bubble wall will always obey the above relation. Accordingly, Henry's law can be applied to bubbles as a boundary condition for the diffusion of dissolved gases in the surrounding liquid.

2.1.7   Rate of Phase Change from Kinetic Theory

A model for phase change at a gas-liquid interface can be developed from the kinetic theory of gases. Following the derivation of Carey,[64] we begin with Maxwell's velocity distribution for an ideal gas and consider a total of N molecules within an arbitrarily sized box of volume V_B. As such, we consider the ideal gas law (2.14) and can express the rate at which molecules will pass out of the box through one of its planar boundaries as

$$j_N = \frac{1}{4}\frac{N}{V_B}\left(\frac{8k_B\theta}{\pi m}\right)^{1/2} \qquad (2.18)$$

In this relation, j_N is the flux in molecules per unit time per unit area, m is the mass of a single molecule and the other symbols have the same definitions as in Section 2.1.4. This equation can be rewritten in terms of the molar flux as

$$j_n = \left(\frac{1}{2\pi M \mathcal{R}\theta}\right)^{1/2} p_i \qquad (2.19)$$

where j_n in the flux in terms of moles rather than molecules and M is the average molecular weight of the gas species.

Note that if the box contains more than one type of gas, the molecular flux of an individual species can be calculated from Equation (2.19) by using the species' partial pressure and molecular weight in place of the total internal pressure p_i and average molecular

weight M. The utility of this expression lies in its lack of explicit dependence upon the dimensions of the original box. Hence, the flux must be the same for any planar surface in the gas. This understanding along with the assumption that the radius of curvature of the bubble remains large relative to molecular length scales suggests that we can use Equation (2.19) for calculating fluxes across the surface of a spherical bubble. Though this model for vapor transport breaks down under the extreme conditions present during violent bubble collapses, the net effects of these inaccuracies over such short durations is minimal.[39] Hence, the rate of phase-change mass transport across the bubble wall can be estimated as the above molecular flux weighted by a 'sticking' probability that reflects the likelihood that a molecule evaporates or condenses when impinging upon the interface.

2.1.8   Mean Free Path from Kinetic Theory

From the kinetic theory of gases, it is possible to define the mean free path of a gas molecule in terms of the thermodynamic conditions of the gas. Because the mean free path defines an appropriate length scale that is used later, it is convenient to define it here as[65]

$$\lambda = \frac{V}{\sqrt{2}\pi N \Omega^2} \qquad (2.20)$$

Above, V is again the bubble volume, N is the number of gas molecules inside the bubble, and Ω is the hard-sphere molecular diameter as calculated from Lennard-Jones potentials.[63] To account for the presence of both air and vapor inside the bubble, Ω is estimated by averaging the tabulated hard-sphere diameters for air and water. As noted by Poling et al.[63] with regard to diffusion coefficients, it is typical to estimate the effective hard-sphere diameter as an arithmetic mean rather than a weighted average based on mole fraction. This same approach is adopted here to calculate mean free path as a part of the liquid-gas temperature jump described in the next section. Inasmuch as concentration gradients are not explicitly calculated in the model proposed here, the applicable mole fractions of air and water at the bubble wall are not known.

2.1.9 Liquid-Gas Temperature Jump

In the study of rarefied gas flows, it is well known from rarefied gas theory that slip conditions may exist at boundaries of the gas flow. In particular, kinetic gas models have been used to analytically predict the jump in temperature from a solid boundary to adjacent gas molecules.[66] In general, this temperature jump occurs when a non-zero temperature gradient exists normal to the boundary. While the analytic solutions to this problem typically involve an infinite, solid boundary to the gas flow, analogous conditions clearly exist during bubble collapse as strong thermal gradients develop. Indeed, this effect has been included in other bubble models that address temperature changes in the liquid.[41,67]

Although the aforementioned bubble models have estimated the temperature jump with an assumed thermal accommodation coefficient as well as other published parameters from the rarefied gas models, we utilize a somewhat simpler formulation here. Accordingly, we only seek to capture the qualitative behavior of the temperature jump. Following Sharipov and Kalempa,[68] we may write the temperature jump as

$$T_w - \theta_w = \zeta \lambda \left. \frac{\partial \theta}{\partial r} \right|_{r=R} \tag{2.21}$$

where θ_w and T_w are the gas and liquid temperatures at the bubble wall (*i.e.*, at $r = R$). Also, λ is the mean free path in the gas and ζ is the temperature jump coefficient determined from kinetic gas models. In the literature relevant to the temperature-jump condition, it is conventional to estimate λ based on measurable gas properties such as viscosity and the surface temperature T_w. However, for convenience, we employ the estimate of mean free path from the previous section in this work. In specifying the jump coefficient ζ, we note that calculated values depend upon the kinetic model used to describe the gas behavior. Moreover, given that the calculated values typically require an assumption of an infinite solid boundary, we conclude that the appropriate value for a bubble is not well known. However, the values calculated by Sharipov and Kalempa[68] for several noble-gas mixtures suggest that likely values range from about 2–2.5. We select a value $\zeta = 2$ here as a round number—calculations not presented indicate that the model is not sensitive to this parameter.

Despite the inclusion of a temperature jump in prior bubble models, the applicability of the jump condition for bubble motions was not explicitly discussed. From the introductory comments stated by Sharipov and Kalempa,[68] we recognize that this temperature-jump model is only appropriate when the Knudsen number Kn (defined as the ratio of the mean free path to the bubble radius) remains less than about 0.1. Moreover, for Kn less than about 0.01, the temperature jump can be neglected. Upon estimating the Knudsen number for a lithotripsy bubble, we find that $Kn \approx 0.1$ just after the tensile portion of the shock wave arrives; however, during the remainder of the bubble motion, $Kn < 0.01$. For sonoluminescence bubbles, Kn remains less than 0.01 during the end-collapse stages and less than 0.1 otherwise. These cursory estimates of the Knudsen number confirm that the conventional relation for estimating temperature jumps is applicable, though the temperature jump may often be negligible. In addition, considering that bubble motions are approximately isothermal except during collapses, we note that the necessity of including any liquid-gas temperature jumps in a bubble model is questionable. For consistency with other models, the ability to model temperature jumps is included here.

2.2 *Explicit Model Description*

The essence of this model is to separately enforce conservation principles in the liquid and gaseous phases, while transfer of heat and mass in/out of the bubble is estimated from basic physical laws. The radial dynamics of the bubble are determined from the conservation of mass, momentum, and energy in the liquid and are coupled to the gas through the pressure generated inside the bubble. In turn, the pressure inside the bubble is governed by the internal gas dynamics, which include the boundary fluxes of heat and mass. Following this approach, model components for both the radial dynamics and the gas dynamics are described below.

2.2.1 *Radial Dynamics in the Liquid*

As noted in Section 2.1.1, the radial bubble dynamics are modeled by enforcing conservation of mass and momentum in the liquid. While energy must also be conserved in the liquid, derivations of the commonly used radial equations do not strictly enforce energy

conservation. Because we are interested in capturing the physics of both vapor and gas bubbles, temperature changes in the surrounding liquid caused by the bubble motion itself may become important.[60] However, to avoid the difficulties associated with direct numerical simulations of strongly forced vapor bubbles, we follow the traditional approach of specifying a Rayleigh-Plesset style equation for the radial dynamics. As discussed further below, we will address the thermal behavior in the liquid separately.

A Lossless Rayleigh-Plesset Model

To gain insight into the form of ODEs that govern bubble motions, the most simple equation for radial dynamics is derived here. The resulting equation is a lossless Rayleigh-Plesset model and can be derived with various approaches. In one approach, the pressure-volume work of bubble expansion is equated with the resulting kinetic energy in the liquid.[69] In an equivalent approach, the conservation equations for the liquid are integrated spatially over the radial coordinate. The latter approach is considered here. As such, we begin with the conservation equations (2.5) and (2.6) and define boundary conditions on the velocity $u_r(r,t)$ and pressure $p(r,t)$ fields:

$$u_r(R,t) = \dot{R} \qquad u_r(\infty,t) = 0 \tag{2.22}$$

$$p(R,t) = p_w \qquad p(\infty,t) = p_\infty \tag{2.23}$$

As indicated, R is the radial distance to the bubble wall, $\dot{R}$ is the velocity of the bubble wall, p_w is the pressure in the liquid at the bubble wall, and p_∞ is the pressure in the liquid far from the bubble. Assuming that the liquid is incompressible, we can integrate Equation (2.5) by separation of variables. Enforcing boundary conditions on u_r, we have

$$u_r(r,t) = \frac{R^2 \dot{R}}{r^2} \tag{2.24}$$

Substituting this result into Equation (2.6), taking the appropriate time derivatives, and integrating from $r = R$ to ∞, we identify the ambient liquid density as ρ_0 and obtain a

simple Rayleigh-Plesset equation:

$$R\ddot{R} + \frac{3}{2}\dot{R}^2 = \frac{1}{\rho_0}\left(p_w - p_\infty\right) \tag{2.25}$$

With the understanding that p_w can be related to the pressure inside the bubble p_i, Equation (2.25) along with a model of the gas dynamics to compute p_i completes a formulation for bubble motion. Acoustic excitation of the bubble enters through p_∞. Given the original assumption of spherical symmetry, it is implicitly assumed that the acoustic wavelength of the excitation is much greater than the bubble radius.

The Gilmore Model

Although the above lossless model is insightful, a realistic model must account for liquid compressibility. While the details associated with deriving such models are omitted here, complete derivations are readily available in the literature.[59,70,71] To put these various models in perspective, Prosperetti and Lezzi[59] have approached the derivation as an asymptotic expansion in terms of the 'small' parameter $(\dot{R}/c_0)$, which is the acoustic Mach number. Here, $\dot{R}$ is again the velocity of the bubble wall and c_0 is the speed of sound at reference conditions.

With this approach, the effects of liquid compressibility can be taken into account and a family of first-order equations can be derived. For perspective, the simple model derived above is a zeroth order model as reflected by the initial assumption of liquid incompressibility. Given the insights provided by expansions in $\dot{R}/c_0$, higher order models are expected to be more accurate in describing the inertial bubble dynamics of interest here. In particular, the equation originally derived by Gilmore[72] is known to perform remarkably well when compared with full PDE simulations. The success of the Gilmore model can be explicitly traced to its formulation in terms of the enthalpy in the liquid at the bubble wall.[59]

Based on the discussion above, the Gilmore equation is chosen for modeling the radial dynamics in the liquid. This equation can be written as

$$\left(1 - \frac{\dot{R}}{C}\right)R\ddot{R} + \frac{3}{2}\left(1 - \frac{\dot{R}}{3C}\right)\dot{R}^2 = \left(1 + \frac{\dot{R}}{C}\right)H + \left(1 - \frac{\dot{R}}{C}\right)\frac{R}{C}\dot{H} \tag{2.26}$$

where capital letters C and H denote the sound speed and enthalpy evaluated at the bubble wall. The sound speed $c(r,t)$ and enthalpy $h(r,t)$ are defined everywhere in the liquid as

$$c^2 = \frac{dp}{d\rho} \qquad \text{and} \qquad h = \int_{p_\infty}^{p} \frac{dp}{\rho} \qquad (2.27)$$

Using the equation of state (2.11) to evaluate these expressions, we obtain

$$c^2 = \frac{\Gamma(p+B)}{\rho} \qquad \text{and} \qquad h = \frac{c^2 - c_0^2}{\Gamma - 1} \qquad (2.28)$$

where $B \equiv 1/(b\,\Gamma) - p_0$.

To implement this model, c and h must be evaluated at the bubble wall. Accordingly, the pressure in the liquid at the bubble wall p_w must be determined as a boundary condition. Assuming that we have calculated the pressure inside the bubble p_i, we consider the effects of liquid viscosity (μ) and the interfacial surface tension (σ) to define p_w as follows:

$$p_w = p_i - \frac{4\mu\dot{R}}{R} - \frac{2\sigma}{R} \qquad (2.29)$$

In this expression, the last term involving surface tension arises from Laplace's relation,[69] while the second term represents a consideration of the three-dimensional stress state of an incompressible liquid at the gas-liquid interface.[73]

Although we have finished a statement of the Gilmore formulation, it is instructive to evaluate the enthalpy at the bubble wall and its time derivative. Noting that evaluation of the enthalpy at infinity requires consideration of the pressure at infinity to be the sum of the reference pressure and the acoustic forcing (i.e., $p_\infty = p_0 + p_{ac}$), we obtain

$$H = \frac{(b\,\Gamma)^{-1/\Gamma}}{\rho_0} \frac{\Gamma}{\Gamma - 1}\left[(p_w + B)^{(\Gamma-1)/\Gamma} - (p_0 + p_{ac} + B)^{(\Gamma-1)/\Gamma} \right] \qquad (2.30)$$

$$\dot{H} = \frac{(b\,\Gamma)^{-1/\Gamma}}{\rho_0}\left[(p_w + B)^{-1/\Gamma}\dot{p}_w - (p_0 + p_{ac} + B)^{-1/\Gamma}\dot{p}_{ac} \right] \qquad (2.31)$$

The above expressions are suitable for inclusion in a computer program and clearly illustrate

that the acoustic forcing appears through its impact on the enthalpy H.

2.2.2 Gas Dynamics Inside the Bubble

As mentioned above, a formulation of the radial bubble dynamics problem is closed by determining the pressure inside the bubble. Accordingly, the gas dynamics are modeled to determine the thermodynamic state of the bubble contents. As presented in Section 2.1.2, the conservation equations may be enforced to conclude that the thermodynamic conditions inside the bubble are spatially uniform and to yield a single equation for the energy within the bubble (2.10).

Equations for the evolution of bubble temperature and/or pressure as derived from energy conservation considerations have been presented elsewhere.[34,36,61] However, these papers do not provide a complete derivation for the case in which mass transfer is considered. Accordingly, a complete derivation is provided below.

Beginning with Equation (2.10), we utilize the specific heat at constant volume c_v to define the internal energy at temperature θ as $e_i = c_v \theta$. Ignoring the influence of temperature on the vibrational modes of gas molecules,[65] c_v remains constant. Hence, if we express the radial heat flux q_r into the bubble with Fourier's Law (2.15), we obtain

$$\rho_m c_v \dot{\theta} = p_i \left(\frac{\dot{n}}{n} - \frac{3\dot{R}}{R} \right) + \frac{3k_g}{R} \left. \frac{\partial \theta}{\partial r} \right|_{r=R} \tag{2.32}$$

where p_i is the uniform pressure inside the bubble and k_g is the thermal conductivity of the gas. Next, we note that the constant-pressure and constant-volume specific heats can be related by the universal gas constant for an ideal gas: $c_p = c_v + \Re$. In addition, we equate the definition of molar density $\rho_m = n/V$ with its value from the equation of state (2.14), take a time derivative, and solve for $\dot{\theta}$ as

$$\dot{\theta} = \theta \left(\frac{\dot{p}_i}{p_i} + \frac{3\dot{R}}{R} - \frac{\dot{n}}{n} \right) \tag{2.33}$$

Finally, substituting (2.33) into (2.32) yields the following equation for the rate of change

of pressure inside the bubble

$$\dot{p}_i = \gamma p_i \left(\frac{\dot{n}}{n} - \frac{3\dot{R}}{R} \right) + (\gamma - 1) \frac{3k_g}{R} \left. \frac{\partial \theta}{\partial r} \right|_{r=R} \tag{2.34}$$

where $\gamma = c_p/c_v$ has been introduced. Note that this equation is identical to that provided by Matula et al.[36] if chemical reactions are ignored. Also, if we consider c_v as a function of temperature, Equation (2.10) can be simplified to an expression equivalent to that used by Toegel et al.[34] for evolution of the bubble temperature.

For clarity in the notation, we mention here that the amount of gas inside the bubble and its time derivative $(n, \dot{n})$ represent sums of contributions from non-condensable gases $(n_g, \dot{n}_g)$ and from water vapor $(n_v, \dot{n}_v)$. The formulations for calculating $\dot{n}_g$ and $\dot{n}_v$ are discussed in detail below.

2.2.3 Heat and Mass Transport

In order to model heat and mass transport to/from a bubble, spatial gradients of temperature and mass concentration must be calculated. As described above, direct numerical simulation of violent bubble collapses typically leads to numerical instabilities as the gradients become very steep. Alternative approaches include approximation of the gradients from scaling principles and a Lagrangian formulation of the problem that requires evaluation of a convolution integral.[74,75] Both of these approaches have been implemented to calculate aspects of heat and mass transfer in the present model. In the sections below, relevant time and length scales are discussed first; subsequently, model formulations for specific aspects of heat and mass transport are described.

Time and Length Scales

The goal of this section is to define time and length scales associated with the diffusion of both heat and mass. In context, 'scales' does not refer to scales used to derive uniform asymptotic expansions. Rather, 'scales' refers to order-of-magnitude estimates of characteristic times and lengths associated with transport phenomena. As such, several time scales are derived from the dynamics of bubble motion, while lengths are calculated from the

partial differential equation for diffusion. Several time scales are derived below, reflecting aspects of the bubble dynamics associated with compression of the gaseous phase as well as phase change. While the scales are derived in this section, their synthesis into the model is left to subsequent sections that explicitly treat heat or mass transport.

To estimate spatial gradients from scaling principles, we assume that the gradient is constant across a boundary layer. This assumption is illustrated in Figure 2.1 for both heat and mass transport. As such, δ_m, δ_θ, and δ_T represent boundary layer thicknesses, T and θ respectively denote the temperature in the liquid and gaseous phases, and C indicates mass concentration. In addition, the subscripts v and g respectively denote vapor and non-condensable gases, while the subscripts w and ∞ indicate locations at the bubble wall and at a distance far from the bubble. As depicted in Figure 2.1, the temperature θ and vapor concentration C_v inside the bubble are assumed to be constant everywhere except within the boundary layers. Similarly, the liquid temperature is defined to be constant at T_∞ everywhere except within the boundary layer. Based on these assumed conditions, fluxes of heat and mass can be estimated from Equation (2.15), provided that convection is ignored and the boundary layer thicknesses are known.

To estimate boundary layer thicknesses, we follow the approach adopted by Matula et al.[52] and Toegel et al.[34] Assuming a time scale for bubble motion can be estimated, we use the partial differential equation for diffusion to estimate a characteristic penetration distance. As such, considering the general diffusion equation (2.16) in Cartesian coordinates, we neglect convection and discretize derivatives to obtain

$$\frac{\Delta \phi}{\Delta t} = \kappa \frac{\Delta \phi}{\Delta x^2} \qquad (2.35)$$

Recognizing that a diffusive penetration distance can be defined as a relative change in the spatial dimension Δx, we define an approximate boundary layer thickness as

$$\delta = \Delta x = \sqrt{\kappa \tau} \qquad (2.36)$$

In the above equation, $\tau = \Delta t$ is an independent time scale that characterizes radial bubble

motions.

To identify time scales for bubble motion, two basic approaches are considered. In the first approach, a time scale is defined as the ratio of a characteristic length or volume to a corresponding velocity.[34,36,67] Using a volumetric ratio $V/\dot{V}$, we can express the time scale in terms of the bubble radius R as follows:

$$\tau_1 = \frac{R}{3\,|\dot{R}|} \tag{2.37}$$

Note that this definition utilizes only the magnitude of the radial velocity in order to maintain positive values for the time scale. In the second approach, we consider the simple Rayleigh-Plesset equation (2.25) and neglect the pressure far from the bubble to obtain the following discretized expression:

$$R\frac{\Delta R}{\Delta t^2} + \frac{3}{2}\frac{\Delta R^2}{\Delta t^2} = \frac{p_w}{\rho_0} \tag{2.38}$$

From this expression, we can define a characteristic time for bubble motion by solving for Δt when $\Delta R \approx R$. Neglecting viscosity and surface tension from relation (2.29) and ignoring the constant multiplier, we obtain a second time scale

$$\tau_2 = \frac{R}{(p_i/\rho_0)^{1/2}} \tag{2.39}$$

In this expression, p_i is the total pressure inside the bubble and ρ_0 is the ambient liquid density.

In comparing the above time scales τ_1 and τ_2, notable differences are observed. Although τ_1 has been used in prior reduced-order models in the literature,[34,36] the presence of a singularity as $|\dot{R}|$ goes to zero leads to awkward numerical behavior. While such singularities can be removed by imposing a minimum amplitude for $|\dot{R}|$ in Equation (2.37), use of τ_2 inherently addresses the problem without reliance on an arbitrary minimum velocity. As discussed in further detail in the ensuing sections, both of these time scales are used in the present model.

While the basic time scales discussed above can be interpreted geometrically in terms

of characteristic lengths and velocities, a separate thermal time scale can be identified for temperature changes in the liquid phase. In addition to heat conduction effects that are well described by the aforementioned scales for bubble motion and boundary-layer thicknesses, the liquid temperature at the bubble wall is affected by the thermodynamics of evaporation and condensation. In the previous literature, only van Iersel et al.[67] addressed temperature changes in the liquid using a model based on length and time scales. In this work, they used an approach based on equations (2.36) and (2.37) to model bubble dynamics in liquid carbon dioxide with relatively small acoustic excitation amplitudes.

To introduce a new time scale derived from the thermal effects of phase change on the liquid, we consider a thin shell of liquid whose thickness is δ_T [see Figure 2.1(b)]. First, we approximate the mass of liquid in this shell as $\rho_0 \, 4\pi R^2 \, \delta_T$ and assume that the liquid temperature T_w is uniform within the shell. Next, we consider heat transfer to/from the liquid shell only from phase-change processes. This approach is tantamount to assuming that thermal conduction on the inner and outer surfaces of the shell roughly offset one another while convection is negligible. Notably, these assumptions are most consistent with isothermal bubble behavior at large radii, when convection is minimized by slow radial velocities and conduction is minimized by the lack of significant thermal gradients. Now, enforcing an energy balance on the liquid shell leads to an expression for an incremental change in temperature ΔT_w as a function of an incremental time change Δt:

$$\Delta T_w = -\frac{\mathcal{L}\dot{n}_v}{\rho_0 \, 4\pi R^2 \, \delta_T \, c_{pL}} \Delta t \qquad (2.40)$$

Above, $\dot{n}_v$ is the molar evaporation rate at the liquid-gas interface, $\mathcal{L}$ is the latent heat of vaporization, and c_{pL} is the heat capacity of the liquid. Setting the magnitude of ΔT_w to unity, we can then solve for a phase-change time scale as

$$\tau_3 = \frac{\rho_0 \, 4\pi R^2 \, \delta_T \, c_{pL}}{\mathcal{L}|\dot{n}_v|} \, (1^\circ\text{K}) \qquad (2.41)$$

Further, given that $\dot{n}_v$ represents a combination of evaporative and condensative fluxes, we note that a singularity occurs when these fluxes cancel one another and $\dot{n}_v = 0$. To address

(a) mass transport   (b) heat transport
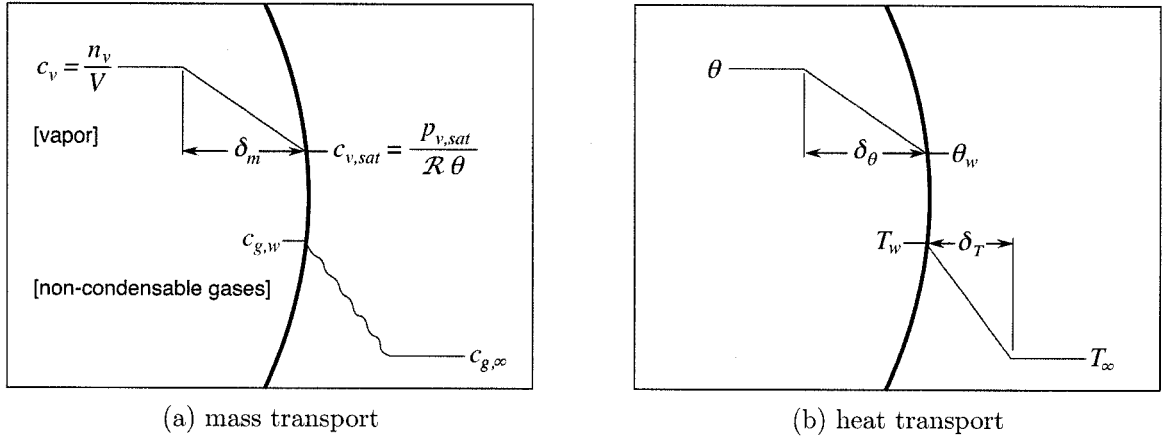
Figure 2.1. Schematic depiction of assumed boundary layers used in the model. In each diagram, the blue line refers to a bubble wall whose curvature implies gas on the left and liquid on the right. The red lines indicate gradients in mass concentration or temperature.

the singularity, only the condensative flux is used to calculate τ_3; this flux is explicitly written below as the p_v term from Equation (2.45).

As discussed in more detail in the following sections, τ_2 and τ_3 are used in conjunction with Equation (2.36) to define the thermal boundary layer thickness in the liquid δ_T. Using the time and length scales defined in this section, the explicit equations used to calculate heat and mass transfer are presented below.

Mass Transport of Non-Condensable Gases

As suggested in Section 2.1.6, Henry's law can be used to couple the thermodynamic state of non-condensable gases inside the bubble to the diffusion of these same gases in the surrounding liquid. Accordingly, if we formulate a mass diffusion problem in the liquid [see Equation (2.16)] and use Henry's law to provide a dynamic boundary condition, the problem may be solved for the flux of non-condensable gases across the bubble wall.

An approximate solution to the mass diffusion problem for a single, spherical bubble was first presented by Eller and Flynn.[74] This is the classic solution used to describe rectified diffusion in gas bubbles. Eller and Flynn transformed the problem into an asymptotic series of equations and analytically solved the zeroth- and first-order equations. Noting that the

Eller-Flynn solution is uniformly valid in time only under equilibrium conditions at which there is no net mass flux to or from the bubble (*i.e., the 'high-frequency' solution*), Fyrillas and Szeri[76] developed a new solution that accounts for non-equilibrium conditions in which a diffusive boundary layer develops. Here, we adopt the zeroth-order Eller-Flynn solution for its simplicity and its ability to capture the basic features of diffusion. The explicit approach was originally developed and implemented to study mass diffusion behavior for lithotripsy bubbles by Church[51] and by Sapozhnikov et al.[10] Note that this approach does not require the scaling assumptions described in the previous section; accordingly, the concentration gradient in Figure 2.1(a) is illustrated by a wavy line and no boundary layer thickness is explicitly depicted.

To state the zeroth-order Eller-Flynn solution, we first define a time scale for diffusion in terms of the actual time t and the bubble radius R as

$$\tau_{ef} = \int_0^t R^4 \, dt' \tag{2.42}$$

Next, we define the function $\mathcal{F}$ to represent the concentration difference that drives diffusion:

$$\mathcal{F} = c_{g,w} - c_{g,\infty} = \frac{p_g - p_0}{\mathcal{H}} \tag{2.43}$$

Here, $c_{g,w}$ is the saturation concentration of non-condensable gases in the liquid at the bubble wall and $c_{g,\infty}$ is the initial concentration everywhere in the liquid. Also, p_g is the partial pressure of non-condensable gases inside the bubble, p_0 is the ambient pressure in the liquid, and $\mathcal{H}$ is Henry's constant for air from Equation (2.17). This arrangement of concentrations is illustrated in Figure 2.1(a), where the wavy red line indicates that no explicit shape of the concentration gradient in the liquid is assumed.

Now, if n_g represents the number of moles of non-condensable gas inside the bubble and n_{g0} represents n_g at time $t = 0$, then we can estimate diffusive transport effects through the

following convolution calculation:

$$n_g = n_{g0} - 4\sqrt{\pi \mathcal{D}} \int_0^\tau \frac{\mathcal{F}(\tau')}{\sqrt{\tau_{ef} - \tau'}} \, d\tau' \tag{2.44}$$

Note that $\mathcal{D}$ in this equation is the diffusion constant of the non-condensable gas in the liquid and is analogous to κ in Equation (2.16). From this solution, the current amount of non-condensable gas inside the bubble n_g may be calculated at a given time. However, for a given bubble size, the current value for n_g implies an updated current value for p_g, which was already used in Equation (2.44) to estimate n_g. To address this circular dependence, Church[51] suggested that sequentially updating n_g and p_g three times provided a reasonably accurate convergence for lithotripsy bubbles. For computational convenience, an adaptation of this approach was used here. This adaptation is discussed further in the next chapter on model implementation.

Mass Transport of Vapor

The model for evaporation and condensation at the bubble wall is based on the kinetic theory of ideal gases as discussed above in Section 2.1.7. The net flux of vapor into the bubble may be estimated by applying Equation (2.19) for both the evaporative and condensative fluxes and subtracting condensation from evaporation. Performing this superposition of fluxes and neglecting any differences between T_w and θ_w, we obtain

$$\dot{n}_v = 4\pi R^2 \frac{\hat{\sigma}}{\sqrt{2\pi M \mathcal{R} T_w}} \left(p_{sat} - p_v \right) \tag{2.45}$$

where $\dot{n}_v$ is again the time rate of change of the number of moles of vapor inside the bubble, T_w is the liquid temperature at the bubble wall, p_{sat} is the saturated vapor pressure evaluated at the bubble wall temperature, p_v is the partial pressure of vapor pressure inside the bubble, and M is the vapor's molecular weight. Based on molecular dynamics simulations,[39] we select a value $\hat{\sigma} = 0.4$ for the accommodation coefficient. While Equation (2.45) is generally applicable as an estimate of phase change, the very meaning of phase change is not sensible at supercritical temperatures. Following Akhatov et al.,[42] $\dot{n}_v$ is identically set to zero when

either θ or T_w exceeds the critical temperature of water.

Strictly speaking, the above kinetic equation for vapor transport only applies for a pure vapor bubble below the critical temperature of the liquid. Above the critical temperature, no transport occurs since the phases are ill-defined. In addition, if non-condensable gases are present, diffusion among vapor and non-condensable gas molecules must also be considered. In particular, such diffusion is important when the time scale for diffusion is much slower than the time scale for bubble motion. Following other reduced-order models,[34,36] we associate evaporation with bubble growth and 'expanded' diffusive boundary layers such that diffusion does not limit the kinetic evaporation rate. Conversely, we note 'compressed' boundary layers during collapse, thereby requiring consideration of diffusion-limited condensation. This phenomenon can be described as 'vapor trapping,' whereby non-condensable gas molecules at the liquid-gas interface inhibit condensation and trap vapor molecules inside the bubble.[39] Again following the aforementioned reduced-order models, we use the scaling principles from Section 2.2.3 to estimate the maximum condensation rate that is permitted by mass diffusion.

Under the assumption of a diffusive boundary layer with a constant concentration gradient [see Figure 2.1(a)], we consider the basic equation for diffusive flux (2.15), discretize the spatial gradient, and express the maximum condensation rate as follows:

$$(\dot{n}_v)_{max,cond} = 4\pi R^2 \, \mathcal{D}_{12} \frac{C_v - C_{v,sat}}{\delta_m} \tag{2.46}$$

Here, $\mathcal{D}_{12}$ is the diffusion coefficient between vapor and non-condensable gas molecules, $C_v = n_v/V$ is the concentration of vapor inside the bubble, $C_{v,sat}$ is the equilibrium concentration at the surface temperature T_w, and δ_m is the boundary layer thickness for mass diffusion. To estimate, δ_m, we consider time scale τ_1 from Equation (2.37), introduce an arbitrary scale factor a_m for fine-tuning, and find the penetration distance from Equation (2.36):

$$\delta_m = a_m \sqrt{\mathcal{D}_{12} \left(\frac{R}{3|\dot{R}|} \right)} \tag{2.47}$$

In addition, δ_m is constrained to remain less than or equal to the bubble radius. As noted

above, τ_1 possesses undesirable singularities when $\left|\dot{R}\right| = 0$. However, model calculations using both τ_1 and τ_2 indicate that τ_1 yields better scaling estimates in that experimental data can be matched with values of a_m near unity. Moreover, the singularity is readily addressed by assigning a minimum value for $\left|\dot{R}\right|$. Model results were found to converge when minimum values on the order of 1 or smaller were used. A minimum value of 10^{-3} was adopted in this effort as a relatively small velocity that does not introduce numerical artifacts.

Discussion of Reduced-Order Heat Transport Models

The classic approach for estimating thermal damping for a gas bubble involves calculation of a temperature gradient in the gas without regard to thermal effects in the liquid. This makes sense for a gas bubble; however, for a bubble with significant vapor content, phase change and the enthalpy of vaporization can significantly affect the energy balance at the bubble wall. Consequently, modeling the heat transport processes of gas-vapor bubbles should comprehensively address both liquid and gas phases.

Of the available reduced-order models in the literature, here we specifically discuss two that address heat transport in both liquid and gas phases. As mentioned at the beginning of this chapter, Yasui[41] incorporated heat transfer in the liquid by assuming exponential temperature profiles in the liquid. Accordingly, the heat transported out of the bubble (*i.e.*, heat conduction from the gas phase and heat of vaporization from vapor condensation) is used to calculate the rate at which a boundary layer of liquid changes temperature. Hence, this approach includes some thermal mass in the liquid near the bubble. In a different approach, van Iersel et al.[67] begin with the same equations and algebraically solve for the temperatures inside the bubble and in the liquid at the bubble wall. The algebraic solution is based on the use of aforementioned scaling principles to estimate boundary layer thicknesses in the gas and in the liquid. Given the nature of this algebraic solution, the liquid temperature at the bubble wall is determined uniquely by the current state of the bubble. Consequently, this approach discounts the thermal mass of the liquid; the prior history of bubble motion does not affect the thermal behavior.

Weighing the merits of these basic approaches, note that Yasui's model has the potential to capture the relevant dynamics over many cycles of oscillation by 'remembering' the bubble history. Such a capability is essential for modeling a HIFU bubble over thousands or even millions of acoustic cycles. However, we also recognize that any model based upon scaling principles must be tuned by pertinent experimental data. Because it is not clear how to experimentally quantify such thermal behavior in the immediate vicinity of an oscillating bubble over thousands of cycles, the simpler task of understanding a single collapse and rebound is attempted here. Accordingly, the present model approximates the heat transport of gas-vapor bubbles with a variation of the aforementioned algebraic solution.

Before proceeding to state this algebraic model, it is constructive to describe other efforts to model heat transfer that were undertaken in this work. In particular, a version of Yasui's model was implemented and found to be only marginally stable when simulating violent collapses in SWL and HIFU. In a separate effort to capture the effects of thermal mass in the liquid, the zeroth-order convolution solution from Plesset and Zwick[75] was implemented. This solution is completely analogous to the Eller-Flynn mass diffusion solution presented in Section 2.2.3 and utilizes the 'boundary-layer' formulation also employed in sophisticated sonoluminescence models.[38,39] Although numerical instabilities were also encountered with the Plesset-Zwick solution, simple test cases were utilized for comparison with the algebraic solution. Accordingly, details of the Plesset-Zwick model are explicitly stated below.

Plesset-Zwick Solution for Thermal Diffusion in the Liquid

The problem for thermal diffusion in the liquid is described by Equation (2.16), where κ refers to the thermal diffusivity of the liquid. This problem is completely analogous to that for mass diffusion in the liquid presented in Section 2.2.3. Again using the time scale τ_{ef}, the solution is obtained by updating Equations (2.43) and (2.44) as follows:

$$\mathcal{F}_{th} = \frac{1}{R^2} \left. \frac{\partial T}{\partial r} \right|_{r=R} \tag{2.48}$$

$$T_w = T_\infty - \sqrt{\frac{k_L}{\rho_0 c_{pL}}} \int_0^\tau \frac{\mathcal{F}_{th}(\tau')}{\sqrt{\tau_{ef} - \tau'}} \, d\tau' \tag{2.49}$$

Again, Figure 2.1(b) illustrates the relevant liquid temperatures, though no assumptions about the structure of the boundary layer are made. To implement the Plesset-Zwick solution, the temperature gradient in Equation (2.48) is found algebraically from the heat transport equations (2.50) and (2.51).

Algebraic Balancing of Heat Transport

To determine an algebraic solution for heat transfer, we formulate the problem by assuming imposed conditions on the uniform gas temperature θ and the constant temperature T_∞ far from the bubble. While T_∞ is a generally applicable boundary condition, θ is imposed by the radial bubble dynamics. As such, at any given time, the bubble radius R and the pressure inside the bubble p_i are calculated from Equations (2.26) and (2.34). In turn, the uniform temperature θ can be calculated from the ideal gas equation of state (2.14). Now, for any time at which θ and T_∞ are known, the heat transport may be determined by solving for the gas and liquid temperatures at the bubble wall (θ_w and T_w).

In the formulation described above, radial dynamics are imposed and heat transport is then estimated. However, Equation (2.34) clearly couples the radius to the heat transport through a thermal conduction term. Although the numerical implementation of this modeling approach recognizes this coupling and seeks convergence between the radial and the thermal dynamics, the algebraic solution presented in this section can be treated as if θ were imposed by the radial dynamics. This solution is described below, while the explicit numerical treatment is deferred to the next chapter.

To determine heat transfer effects, we first assume linear concentration gradients across thermal boundary layers in both the liquid and the gas [see Figure 2.1(b)]. Then, using Fourier's Law from Equation (2.15) with discretized gradients, we enforce an energy balance at the liquid-gas interface as[67]

$$4\pi R^2 \, k_g \frac{\theta_w - \theta}{\delta_\theta} + 4\pi R^2 \, k_L \frac{T_w - T_\infty}{\delta_T} + \dot{n}_v \mathcal{L} + c_v \left(\dot{n}_g + \dot{n}_v \right) \left(\theta_w - T_w \right) = 0 \qquad (2.50)$$

Here, k_g and k_L are the thermal conductivities in the gas and liquid, $\mathcal{L}$ is the heat of vaporization, and c_v is the heat capacity of the mixture of vapor and non-condensable gas

molecules that changes phase and temperature from T_w to θ_w. Next, we note that T_w and θ_w can be related by a temperature-jump relation based on Equation (2.21):

$$T_w - \theta_w = \zeta\lambda\frac{\theta_w - \theta}{\delta_\theta} \qquad (2.51)$$

The previous two equations can now be solved for T_w and θ_w as long as the boundary layer thicknesses can be estimated.

Following the approach outlined in Section 2.2.3, we define the thermal boundary layer in the gas using the time scale τ_2 in conjunction with Equation (2.36). We obtain

$$\delta_\theta = a_\theta \left(\frac{k_g}{\rho_m c_p} \frac{R}{\sqrt{p_i/\rho_0}}\right)^{1/2} \qquad (2.52)$$

where a_θ is an arbitrary multiplicative factor, ρ_m is the molar density of gases inside the bubble, and $c_p = c_v + \mathcal{R}$ is the constant-pressure heat capacity. Moreover, δ_θ is required to remain less than or equal to the bubble radius.

To define an equivalent boundary layer in the liquid, we note the contributions of both conduction and phase change to temperature changes. Accordingly, two relevant time scales (τ_2 and τ_3) were defined in Section 2.2.3. Used with Equation (2.36), these time scales lead to the following estimates of boundary layer thickness:

$$\delta_{T1} = \left(\frac{k_L}{\rho_0 c_{pL}} \frac{R}{\sqrt{p_i/\rho_0}}\right)^{1/2} \qquad (2.53)$$

$$\delta_{T2} = \left(\frac{k_L}{\rho_0 c_{pL}} \frac{4\pi R^2 \rho_0 c_{pL}}{\mathcal{L}|\dot{n}_v|}\delta_{T2}\right)^{1/2} \qquad \Rightarrow \qquad \delta_{T2} = \frac{k_L\sqrt{2\pi M\mathcal{R}T_w}}{\mathcal{L}p_v\hat{\sigma}} \qquad (2.54)$$

Above, c_{pL} is the heat capacity of the liquid while δ_{T1} and δ_{T2} correspond to time scales τ_2 and τ_3, respectively. Moreover, as mentioned above, δ_{T2} avoids singularities by including only the condensative term from Equation (2.45) for $\dot{n}_v$.

For simplicity, using one or the other of these thicknesses would be desirable. Upon closer examination, it is apparent that δ_{T2} remains smaller than δ_{T1} for an inertially collapsing bubble. From the perspective that the actual boundary layer thickness will be as thin

as necessary to accommodate the relevant energy fluxes, using only δ_{T2} is appealing. However, using a scaling with δ_{T2} alone does not produce liquid temperatures (T_w) that closely match those calculated by the Plesset-Zwick approach from the previous section, wherein no boundary layer scaling is assumed. On the other hand, using δ_{T1} alone introduces a numerical instability. To match the Plesset-Zwick results, the following strategy for scaling the thermal boundary layer in the liquid was adopted:

$$
\delta_T = \begin{cases}
a_T \left(0.3\, \delta_{T1} + 0.7\, \delta_{T2}\right) & \text{when } T_w \text{ or } \theta < T_c \\
a_T \delta_{T1} & \text{when } T_w \text{ or } \theta \geq T_c
\end{cases}
\tag{2.55}
$$

Here, a_T is an arbitrary factor for fine-tuning and T_c is the critical temperature of the liquid, above which only thermal conduction occurs. Although the chosen linear combination of δ_{T1} and δ_{T2} is somewhat arbitrary, the above formulation was found to be numerically stable and to provide estimates of T_w that agree with the Plesset-Zwick approach. Further discussion of this choice of scaling is deferred to Chapter 4.

Chapter 3

MODEL IMPLEMENTATION

While the previous chapter describes the assumptions and equations used to formulate a model, it does not describe how this model was implemented to generate numerical results. The numerical implementation is presented here. Considering that the essence of the model is a set of ordinary differential equations (ODEs), a typical approach is to define a state vector $\mathbf{y}$ and to formulate the ODEs in state-space form $\mathbf{y}' = f(\mathbf{y}, t)$, where t is time and the prime denotes a time derivative.

In this form, various numerical integration algorithms can be used. An adaptation of this approach was adopted here, wherein a fifth-order Runge-Kutta routine with variable step sizing was implemented with double precision in Fortran95 and compiled in *gfortran*.[77] Moreover, the Fortran code was written with switches that allow the various mechanisms of heat and mass transport from Section 2.2.3 to be turned on or off, thereby enabling exploration of the impact of each mechanism on the dynamics. Details of the numerical integration strategy and its convergence are provided below.

3.1 Numerical Model

3.1.1 Integration Algorithm

The numerical integration is performed using an adaptive fifth-order Runge-Kutta method with explicit time-marching that includes error estimates by also evaluating an embedded fourth-order solution.[78] In simplest terms, if the governing equations can be expressed in state-space form, then the numerical integration by Runge-Kutta can proceed by just evaluating the time derivative $\mathbf{y}'$. The manner in which the time derivative is calculated is discussed in the ensuing section.

The error estimates mentioned above are used to enforce an error tolerance on each time step and to adaptively determine the size of each time step. Such variability in the step size

is necessary here because of the numerically stiff nature of bubble collapses, which involve both fast and slow time scales. Error estimates are normalized to the current value of each state variable and then compared to a dimensionless integration tolerance ϵ. If the error exceeds the tolerance for any state variable, the integration step is rejected and a smaller time step is chosen. If the error tolerance is met for all variables, the step is accepted and a larger step size is selected for the next attempted integration step. Consider an attempted time step of size dt and a maximum error estimate among state variables of $\mathcal{E}$. Then, the variation of step size proceeds according to the following rules:

if $\mathcal{E} > \epsilon$, step rejected:

$$dt_{guess} = \left[0.8 \ (\epsilon/\mathcal{E})^{1/4} \right] \, dt$$

$$dt_{next} = \max\{dt_{guess}, \ 0.1 \, dt, \ 10^{-50} \ \text{sec}\}$$

if $\mathcal{E} \leq \epsilon$, step accepted:

$$dt_{guess} = \left[(1/0.8) \ (\epsilon/\mathcal{E})^{1/5} \right] \, dt$$

$$dt_{next} = \min\{dt_{guess}, \ 5 \, dt, \ 10^{-7} \ \text{sec}\}$$

where dt_{guess} is an estimate for the next time step and dt_{next} is the actual size chosen. Note the 'max' and 'min' operators select the respective maximum and minimum values and that the explicit values used in the above rules were chosen for successful integration of bubble collapses and rebounds.

3.1.2 Treatment of State Variables and Thermal Variables

As shown in the upper left corner of Figure 3.1, the state variables used for the Runge-Kutta algorithm described above include the bubble radius (R), velocity $(\dot{R})$, pressure (p_i), moles of non-condensable gas (n_g), and moles of water vapor (n_v). While these variables technically define the state of the bubble, they do not address any changes in the gas and liquid temperatures at the bubble wall $(\theta_w, \ T_w)$. Because these liquid temperatures affect the heat transfer from the bubble as well as the saturated vapor pressure at the interface, these thermal variables must be 'settled' during each time step to address heat transport. In the schematic of Figure 3.1 for each Runge-Kutta time step, the substep used to update

the thermal variables is outlined in red. Due to the coupling of heat transport to the time derivative of the state variable n_v, up to 10 iterations are used to solve the heat transport problem in an attempt to achieve convergence. As noted in the figure, the thermal substep is executed using either the scaling approach from Section 2.2.3 or the convolution solution from Section 2.2.3. This approach of using a substep to 'settle' variables that impact the bubble's state is comparable to that implemented by Church[51] for mass diffusion.

Having defined the thermal substep, we now describe the overall algorithm used to execute each Runge-Kutta time step. First, the current value of the state vector $\mathbf{y}^{(k)}$ at the start of the kth step is used to update the fluid properties (see Section 3.1.4 and Appendix A). Next, evaluation of the state derivative $\mathbf{y}'$ involves two substeps: settling the thermal variables as described above and calculating time derivatives for the remaining variables. Note that the convolution solution for the transport of non-condensable gases cannot be easily implemented to obtain $\dot{n}_g$. Numerical evaluation of a time derivative of Equation (2.44) is possible; however, the derivative worsens the singularity encountered at $\tau_{ef} = \tau'$ and causes numerical instabilities for small time steps. Church[51] used a substep to settle n_g and its associated partial pressure. Here, we choose to decouple the diffusion problem from the radial dynamics and approximate the time derivative as the average rate of change of n_g across the previous time step. This decoupling is based on the assumption that aqueous diffusion is typically slow relative to bubble motion. As implemented, this assumption is justified in that it produces results very similar to those obtained with Church's approach. The remaining state variables are calculated in a straightforward manner from the equations in Chapter 2. After completing evaluations of $\mathbf{y}'$ and execution of the Runge-Kutta integration, the thermal substep and the convolution for n_g are performed. As such, the full step is completed to obtain the next state $\mathbf{y}^{k+1}$ along with updated values of the ancillary thermal variables.

3.1.3   Model Initialization

The previous sections describe how the numerical integration progresses; however, definition of the model implementation must also include its initialization. First, we note that three

boundary-layer scaling constants are defined for mass diffusion inside the bubble (a_m), heat conduction inside the bubble(a_θ), and heat conduction in the liquid (a_T). Next, we note that the following logical switches exist to control how heat and mass transport are estimated:

- Diffusion of non-condensable gases can be turned *on* or *off*.

- Vapor transport (*i.e.*, phase change at the liquid-gas interface) can be turned *on* or *off*.

- If vapor transport is *on*, vapor trapping (*i.e.*, limiting of condensation by mass diffusion) can be turned *on* or *off*.

- Heat transport in both the gas and liquid phases can be turned *on* or *off*.

- If heat transport is *on*, heat conduction in the liquid and corresponding temperature changes in the liquid can be turned *on* or *off*.

The final aspect of model initialization is the bubble's initial conditions. The initial radius (R) and velocity ($\dot{R}$) are specified directly. From there, either an equilibrium or a non-equilibrium bubble is specified, as follows:

Equilibrium bubble
[1] Pressure inside the bubble is calculated from the static pressure far from the bubble and surface tension as $p_i = p_\infty + 2\sigma/R$.
[2] The partial pressure of vapor is assumed to be the saturated vapor pressure (p_{sat}), while the partial pressure of air is taken to be $p_{air} = p_i - p_{sat}$.
[3] The ideal gas equation is then used to calculate n_v and n_g from the associated partial pressures.

Non-equilibrium bubble
[1] The molar fraction of vapor (f_v) is explicitly specified as an input.
[2] The partial pressure of vapor inside the bubble is assumed to be the saturated vapor pressure; hence, $p_i = p_{sat}/f_v$. Accordingly, the partial pressure of air is again $p_{air} = p_i - p_{sat}$.
[3] The ideal gas equation is then used to calculate n_v and n_g from the associated partial pressures.

Note that as defined, an 'equilibrium' bubble will dissolve away unless no diffusion of non-condensable gases occurs.

3.1.4 Fluid Properties

A single bubble is modeled as an air bubble in water. Given the high temperatures and pressures generated during inertial collapses, it is useful to consider the effects of any changes in the thermodynamic properties of both the liquid and gaseous phases. As noted in Figure 3.1, the fluid properties are updated after completion of each integration time step. The explicit equations used to calculate fluid properties as a function of the current state variables are described in detail in Appendix A.

3.2 Numerical Performance

3.2.1 Convergence

Successful implementation of the above numerical model requires that convergence is achieved as the error tolerance ϵ becomes smaller. To investigate this type of convergence, the Rayleigh collapse of a lithotripsy-like bubble was simulated using error tolerances from 10^{-6} to 10^{-16}. The basic radius-time curve for this bubble is shown in Figure 3.2(a). Notably, the curves generally lie on top of one another across a range of error tolerances from 10^{-8} to 10^{-16}. The smaller time steps required by smaller tolerances should produce more accurate results for a straightforward numerical integration. However, as discussed above, the present model includes substep operations for both thermal variables as well as for mass diffusion of dissolved gases in the liquid. Moreover, as described in Section 3.1.2, the convolution integral that determines n_g can be numerically troublesome for very small time steps. This effect is clearly seen in Figure 3.2(b), where the extra noise is evident on the calculated values of n_g at the smallest error tolerance. Though this noise is noteworthy, the overall model produces consistent results.

To explore the convergence in more detail, close-up views at the minimum volume during collapse and at the maximum volume during the ensuing rebound are shown in Figure 3.3. At minimum volume in parts (a) and (b), the results appear to approach convergence as ϵ is reduced from 10^{-6} through 10^{-11}. However, as ϵ is further reduced, the timing of the minimum volume shifts slightly. Considering the noisy behavior associated with diffusion from Figure 3.2(b), it appears that such noise may contribute to the observed time shift of

the minimum volume at the smallest tolerances. Moving to the maximum rebound volume in parts (c) and (d), we note that the smaller tolerances in (d) produce less scatter even though there does not appear to be a monotonic convergence to a specific value. Hence, the model does provide an overall convergence even though a small amount of uncertainty is persistent. This variability may be explained by a combination of three contributing factors: (1) numerical uncertainty in the integration algorithm with its substeps, (2) sensitive dynamics of a strongly nonlinear physical system as represented by the mathematical model, and (3) limitations of machine precision. For context, the uncertainties are about 0.5 ppm in the timing of the minimum volume and 500 ppm in the maximum rebound volume. Considering the nature of the scaling model developed here, this convergence behavior is deemed to be suitable. Unless otherwise noted, a tolerance of 10^{-9} was used in model calculations presented in this effort.

3.2.2 Other Characteristics

Aside from numerical convergence characteristics, other observations of model stability and performance have been noted. First, with the scaling model for heat transport, it was found that numerical performance is much better when heat conduction and temperature changes in the liquid are enabled. More specifically, in the absence of liquid heating, the model requires extremely small step sizes and cannot effectively integrate through a violent collapse. This behavior can be explained by recognizing that a fixed liquid temperature can lead to an overprediction of the temperature gradient in the gas during collapse. Through Equation (2.34), the overestimated temperature gradient leads to an enhanced coupling of the radial dynamics with the heat transport, which is treated as a substep to the Runge-Kutta integration. Because the thermal variables are not directly integrated as state variables, very small steps are required to enable reasonable convergence during the thermal substep. Although the iteration limit of 10 is often exceeded during violent collapses, the presence of liquid heating renders the estimation of temperature gradients much more consistent, thereby minimizing relative errors in the state variables and enabling integration to proceed with larger steps.

A second observation involves use of the Plesset-Zwick model for the thermal substep. Because the formulation for this heat transport model is analogous to that for diffusion of non-condensable gases, the same numerical challenges apply. In particular, a singularity in the convolution integral when $\tau_{ef} = \tau'$ leads to instabilities when the step size is small. Unfortunately, the violent collapses associated with SWL and HIFU require small time steps through which the Plesset-Zwick solution cannot be successfully integrated with the scheme adopted here. While the Plesset-Zwick approach is only used for more mild collapses, results from such a mild collapse can be used as a comparative standard for the scaling model. Such comparisons are considered further in the next chapter.

$$y^{(k)} = \left\{ \begin{array}{c} R \\ \dot{R} \\ p_i \\ n_g \\ n_v \end{array} \right\}$$

update fluid properties
using current state

$y^{(k)}$

Evaluate State Derivative

$$y' = f(y, t)$$

[settle thermal variables]

$$\dot{n}_g = \frac{n_g^{(k)} - n_g^{(k-1)}}{\Delta t^{(k-1)}}$$

$\dot{p}_i$ (2.34)

$\dot{R}, \ddot{R}$ (2.26) (2.29) (2.30) (2.31)

Settle Thermal Variables

calculate θ (2.14)

calculate δ_θ (2.50)

estimate $\dot{n}_v$ (2.45) (2.46)

calculate δ_T (2.53)

solve for T_w, θ_w
(2.48) (2.49)
(2.42) (2.49) (2.54) (2.55)

NO

Is relative change in $T_w < 0.01$?
OR
Is number of iterations > 10 ?

YES

return $\dot{n}_v, T_w, \theta_w, \theta$

End-Step Update

[settle thermal variables]

calculate $n_g^{(k+1)}$

(2.42) (2.43) (2.44)

$y^{(k+1)}$

Figure 3.1. Schematic of the numerical algorithm implemented for each Runge-Kutta time step. The annotated numbers indicate equations from Chapter 2. Note that the blue numbers refer to an implementation of the Plesset-Zwick model for determining the liquid temperature at the bubble wall T_w.

(a) bubble radius

(b) moles of air inside bubble (n_g)
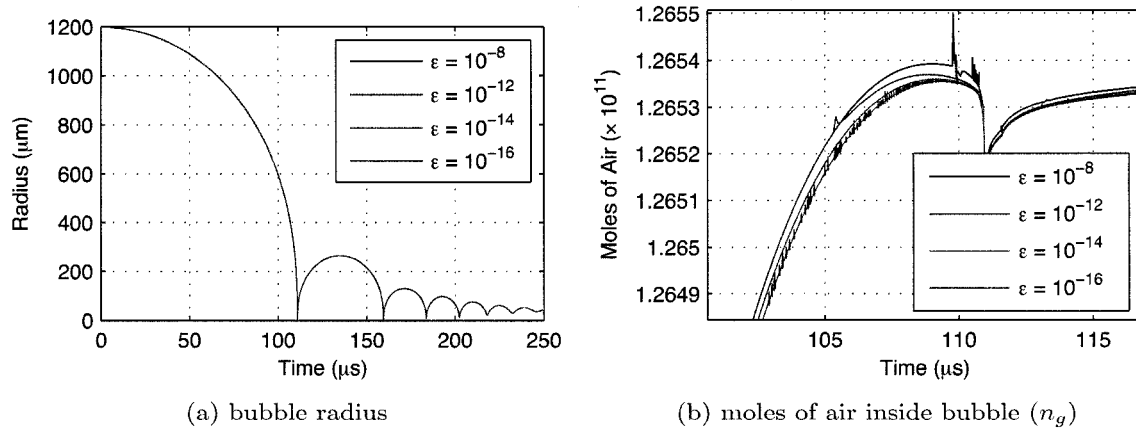
Figure 3.2. Sample model results for a Rayleigh collapse that simulates a lithotripsy bubble. The following model parameters were used for a non-equilibrium bubble: $T_\infty = 20°C$, initial radius $R_0 = 1.2$ mm, initial velocity $\dot{R} = 0$, initial vapor fraction $f_v = 0.999$, $a_m = 0.2$, $a - \theta = 0.5$, $a_T = 1.3$. The scaling model (rather than the Plesset-Zwick model) was used for heat transport.
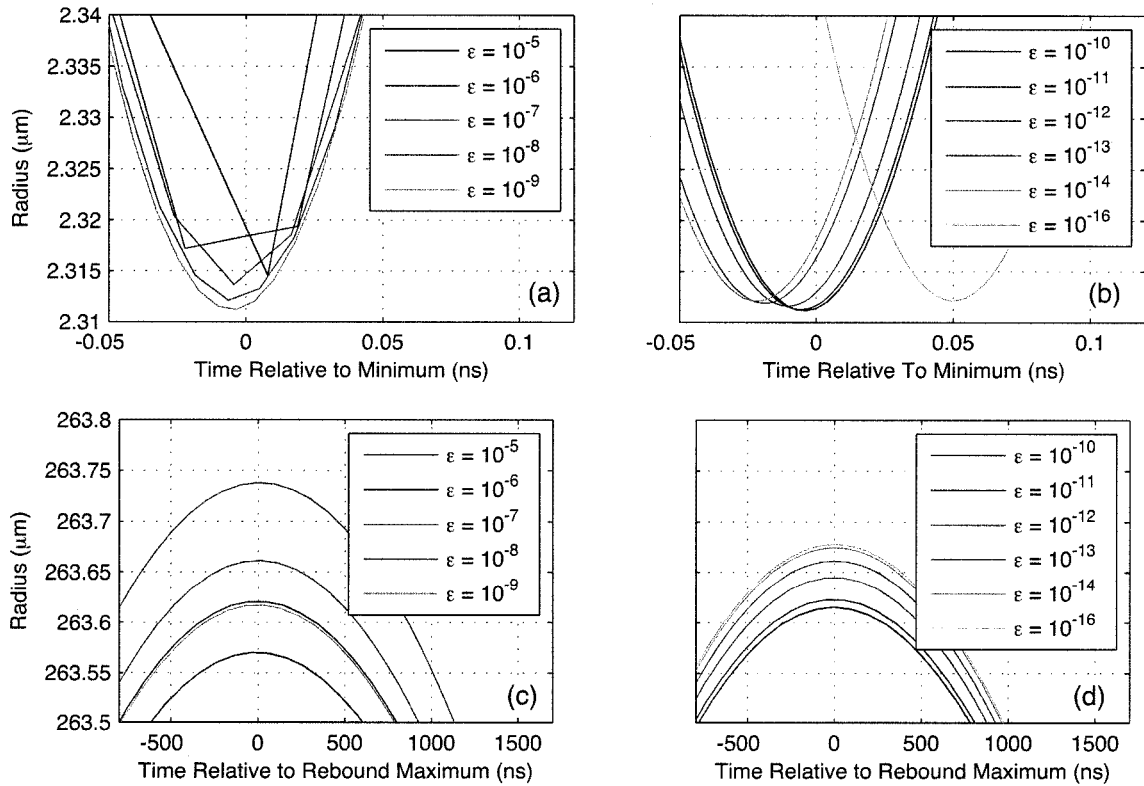
Figure 3.3. Model results demonstrating numerical convergence as a function of the error tolerance parameter ϵ. The bubble minimum radius at the end of collapse is shown in (a) and (b), while the maximum radius during the subsequent rebound is shown in (c) and (d). The model parameters were the same as those for Figure 3.2.

Chapter 4

MODEL PREDICTIONS

As noted in the introduction, the bubble model is intended to elucidate both the mechanical and thermal roles played by vapor in the context of a single collapse and rebound. Given the formulation presented in Chapter 2, the relevant model parameters define the boundary layer thicknesses: a_m scales the diffusive gradient inside the bubble to control the mechanical effects of vapor trapping; a_θ and a_T scale the temperature gradients in the gas and liquid phases, thereby affecting the thermal behavior. Based on this formulation, all three parameters are not explicitly defined even though they should remain on the order of 1. To define these parameters, the strategy here involves the use of other model results to identify a_θ and a_T, while experimental data from the ensuing chapters assist in the ultimate determination of a_m. Accordingly, this chapter includes an initial section to tune the thermal scaling parameters, a subsequent section to test model predictions against other published models, and a final section in which model predictions elucidate the roles of various damping mechanisms in order to guide experiments.

4.1 Determining the Thermal Model Parameters

4.1.1 Thermal Boundary Layer in the Gas

To tune the thermal boundary layer scaling in the gas, a specific test case was considered for which detailed numerical results are readily available. More specifically, Preston[32] implemented a 'gold standard' model of a gas-vapor bubble and explicitly solved for the spatial profiles of the thermal and diffusive variables. Moreover, he presented results for a test case in which a bubble was excited by the following tensile Gaussian pressure pulse:

$$p_{ac} = -p_0\, A\, \exp\left[-\left(\frac{t - t_0}{t_w} \right)^2 \right]$$ (4.1)

Here, p_0 is atmospheric pressure, $A = 0.985$, $t_w = 1.01 \times 10^{-4}$ s, and t_0 is an arbitrary time offset. In addition, the test case assumed a gas-vapor bubble that was initially at rest with radius $R_0 = 40.3$ μm and surrounding temperature $T_\infty = 298°$K. Figure 4.1 shows radius-time curves from Preston's model (top) and from the present model (bottom). In the present model, the parameters used were $a_m = 0.2$ and $a_\theta = 0.5$; moreover, the Plesset-Zwick formulation was used for heat transport in the liquid along with a slightly smaller error tolerance of 10^{-8}. In comparing these curves, it is immediately apparent that the bubble rebounds possess less damping in the Preston model. This behavior can be attributed to Preston's use of a Rayleigh-Plesset model that does not account for liquid compressibility.

To evaluate the scaling $a_\theta = 0.5$, we compare the calculated boundary layer thickness with the profiles presented by Preston. Preston's results at the time points indicated in Figure 4.1 are reproduced in parts (a)–(e) of Figure 4.2. In part (f) of this figure, the results from the present model are plotted for all times. Note that the boundary layer thicknesses were normalized relative to bubble radius. As indicated for each of Preston's plots, an approximate boundary layer thickness based on a constant gradient can be interpreted graphically. Comparing these estimated thicknesses with the marked red circles in part (f), the scaling $a_\theta = 0.5$ provides a reasonable estimate of the temperature gradient throughout the collapse/rebound cycle. This scaling for heat conduction in the gas phase will be used in subsequent calculations unless stated otherwise.

4.1.2   Thermal Boundary Layer in the Liquid

To tune model behavior with regard to heat transport in the liquid, calculations using the Plesset-Zwick substep were compared to results from the scaling approach. In the scaling model, the impact of the boundary layer thickness as controlled by a_T can be interpreted relative to the implicit boundary-layer assumptions of the Plesset-Zwick convolution. In this context, the Plesset-Zwick formulation was treated as a standard solution from which a particular choice of a_T could be justified. As a first step in this comparison, the results produced by the Plesset-Zwick substep were independently tested against published results. Then, the aforementioned test case used by Preston was simulated with both modeling

54
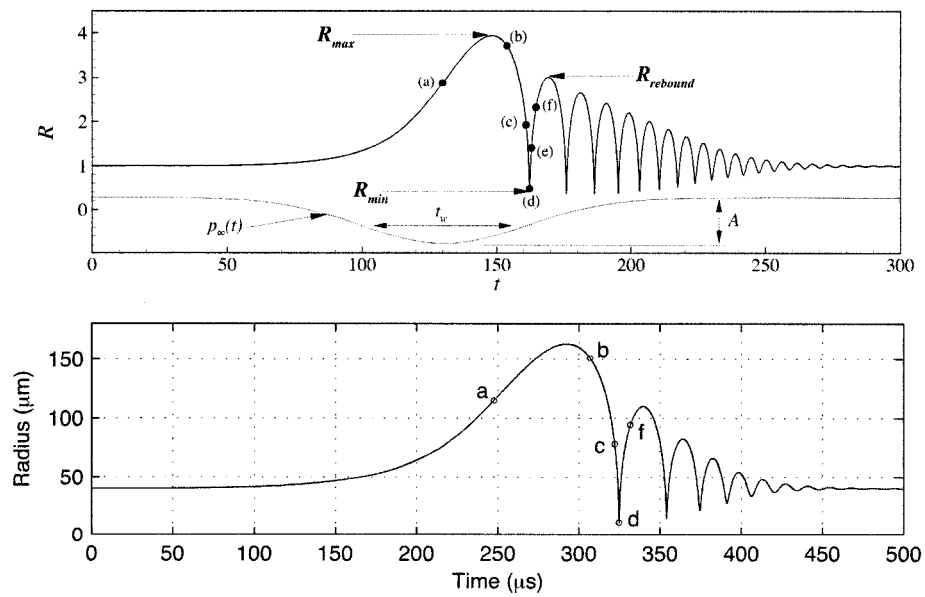
Figure 4.1. Radius-time curve for the 'Preston' bubble,[32] as reproduced from Figure 2.3(a) of the referenced dissertation [top] and as simulated by the present model [bottom]. The labeled points denote times at which spatial profiles of temperature are provided. Note that the time and radius are shown in nondimensional coordinates in the top plot. For the present model, the Plesset-Zwick formulation for heat transport in the liquid was used with an error tolerance of $\epsilon = 10^{-8}$.

(a) Point a, $\delta_\theta / R \approx 0.48$

(b) Point b, $\delta_\theta / R \approx 0.33$

(c) Point c, $\delta_\theta / R \approx 0.25$

(d) Point d, $\delta_\theta / R \approx 0.03$

(e) Point f, $\delta_\theta / R \approx 0.33$

(f) δ_θ / R [present model]
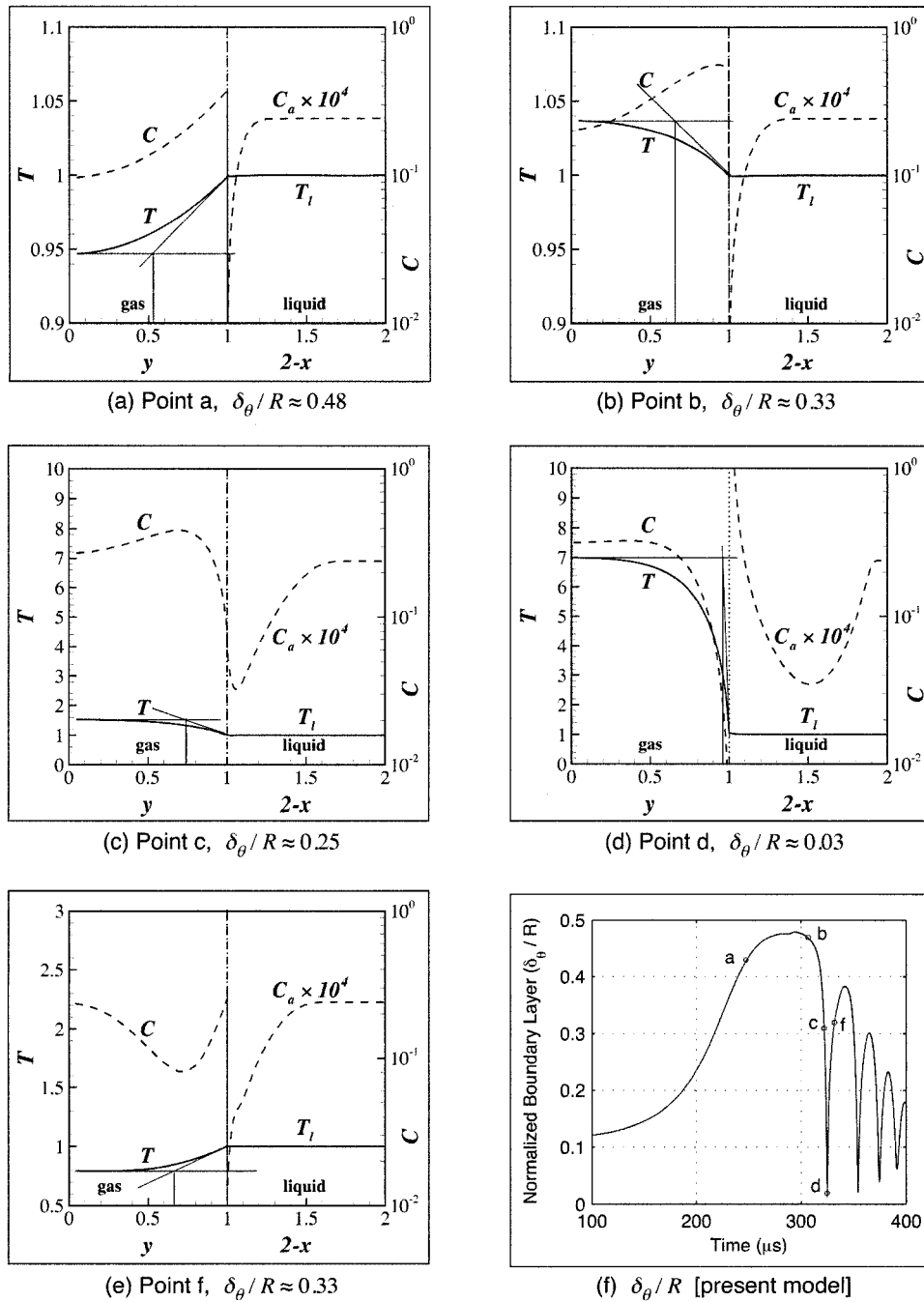
Figure 4.2. Spatial profiles of temperature inside the 'Preston' bubble[32] for various time points labeled in Figure 4.1. Parts (a) through (e) are reproduced from Figure 2.4 of the referenced dissertation. On these plots, red and blue construction lines are overlaid on the original plots to approximate boundary layer thicknesses with constant temperature gradients. Moreover, the plotted radial scale from 0 to 1 in the gas corresponds to the center of the bubble to the bubble wall at $r = R$. Part (f) depicts the boundary layer thickness predicted by the present model.

approaches to assist in the determination of a_T.

To test the Plesset-Zwick approach used in this effort, we considered calculations performed by Plesset and Zwick[79] for the growth rates of vapor bubbles in superheated water. Although they adopted the same formulation of the problem as used both in their prior paper[75] and in the 'Plesset-Zwick' substep here, their relevant calculations invoked two additional approximations. More specifically, Plesset and Zwick derived asymptotic expressions both for the initial, rapid bubble growth that is limited by the inertia of the liquid and for the subsequent growth that is limited by the rate of heat transfer to the bubble. Results of these calculations are shown in Figure 4.3(a). In part (b) of the same figure, calculations from the present model are plotted. These calculations were executed for a pure vapor bubble with an initial radius of 20 μm and an error tolerance $\epsilon = 10^{-6}$ to minimize singularities in the convolution integral. Note that in both plots, the curves are artificially separated in time for viewability.

In comparing these plots, it is evident that the present model predicts faster bubble growth. This discrepancy can be interpreted to mean that the thickness of the thermal boundary layer in the liquid is underpredicted by the Plesset-Zwick substep used here. Indeed, this behavior is expected given the well understood 'high-frequency' limit[74] that implicitly governs the zeroth-order convolution. That is, the convolution solution is asymptotically valid only at high frequencies for which the boundary layer remains thin. However, for the type of bubble responses plotted in Figure 4.3, the extended duration of growth leads to evolution of a significant thermal boundary layer whose thickness limits both the heat flux into the bubble and its corresponding growth rate. Although the present model with the Plesset-Zwick substep does not fully capture the long-term evolution of the thermal boundary layer in the liquid, this behavior is understood. Moreover, for a single collapse a rebound over which the 'high-frequency' approximation remains valid, the Plesset-Zwick model should provide physically meaningful results with regard to the thermal boundary layer.

Having gained confidence in the performance of the Plesset-Zwick substep, we then used its results to determine a suitable scaling factor a_T. Using the same Preston bubble from the previous section, the liquid temperature at the bubble wall calculated with the Plesset-

Zwick substep was compared to the temperature calculated with various scaling values a_T. Calculated temperatures are plotted in Figure 4.4(a). Noting the numerical noise introduced by the convolution, it is apparent that a scaling of $a_T = 1.3$ produces a peak liquid temperature that matches the convolution solution quite closely, even though the peak temperature occurs a fraction of a microsecond later in all of the scaling calculations. Further comparison of these curves raises two salient points. First, the Plesset-Zwick substep predicts a noticeably higher liquid temperature during the bubble rebound (*i.e.*, after the peak temperature was achieved). This result can be explained by the nature of the convolution solution—such a solution has a 'memory' of the bubble history such that the nearby liquid possesses a thermal mass. In contrast, the scaling solution algebraically solves for the liquid temperature based on the gas temperature and the concomitant heat and mass transfer at the boundary. Because the scaling approach does not explicitly account for thermal mass in the liquid, the temperature drops relatively quickly based on the very fast radial dynamics during the rebound. The second observation from Figure 4.4(a) involves the evident discontinuities in the liquid temperature. These discontinuities are an artifact of the time scale used to define the boundary layer thickness δ_T [see Equation (2.55)]. As the temperature inside the bubble exceeds the critical temperature, phase change no longer occurs and the condensation time scale becomes irrelevant. Although the presence of such a discontinuity is clearly not physically realistic, this type of detail is beyond the intended scope of the scaling model. Consequently, the discontinuity is deemed acceptable and a_T was calibrated accordingly.

Although it is also possible to compare the temperature predictions for the present model to those from Preston's work, such a comparison is difficult for several reasons. In particular, Preston's model differs in three significant regards: (1) liquid compressibility was not taken into account, (2) fluid properties were not changed as a function of the local thermodynamic state, and (3) phase change at supercritical temperatures was not suspended. Ultimately, a peak liquid temperature of about 335°K was obtained by Preston as opposed to the 416°K predicted here. It is likely that reasons (1) and (2) listed above account for much of this discrepancy. Given these considerations, tuning the scaling factor a_T by comparison of the scaling and Plesset-Zwick substeps in the present model is more appropriate than

58
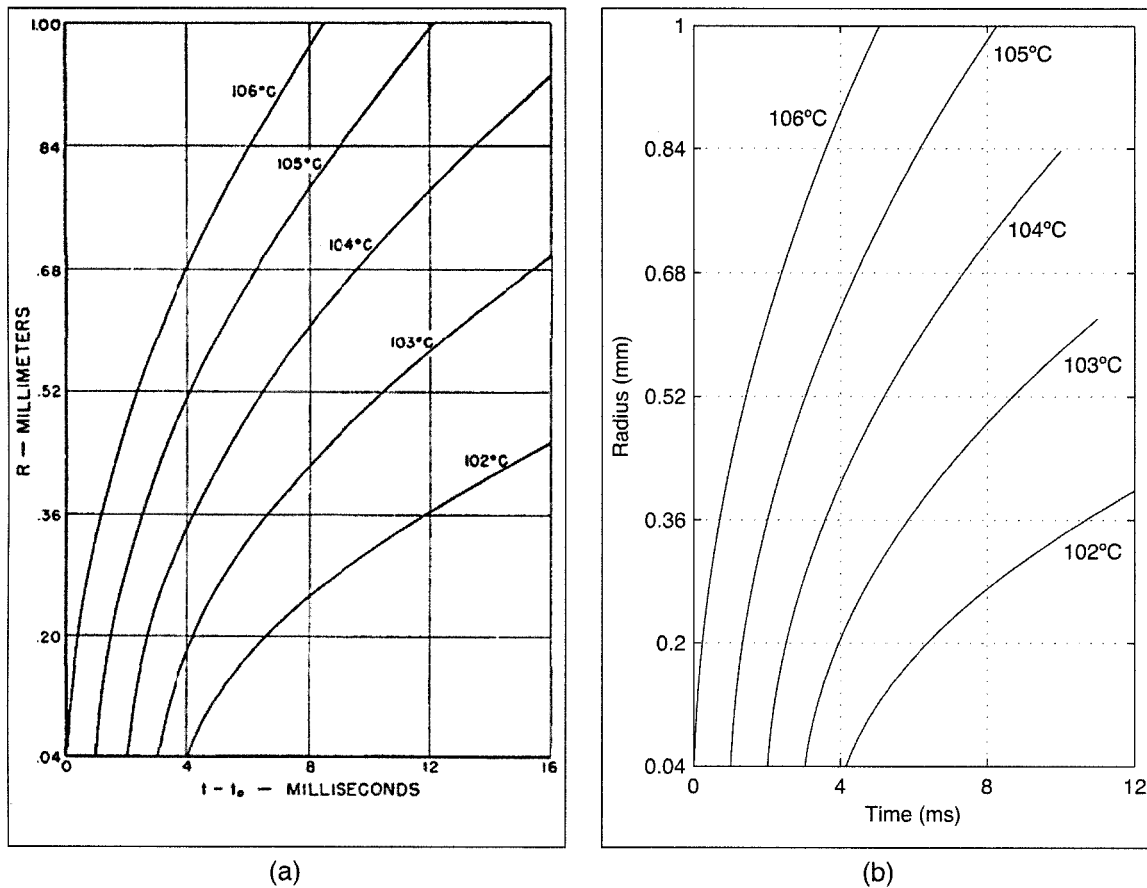
Figure 4.3. The growth rates of vapor bubbles are plotted at several superheated temperatures. Part (a) is reproduced from a paper by Plesset and Zwick[79]. In (b), analogous results from the present model are plotted, where the Plesset-Zwick convolution was used to model heat transport in the liquid. Note that in both plots, each curve is offset by 1 ms for clarity.

attempting a direct comparison of the scaling model with Preston's model.

4.2 Benchmark Tests

In order to test the present model, direct comparisons with other published models is useful. To this end, models of sonoluminescence bubbles and lithotripsy bubbles both provide results regarding the thermodynamics of a single, violent collapse. In the next sections, such comparisons are made to gain an understanding of the performance of the scaling model implemented here.
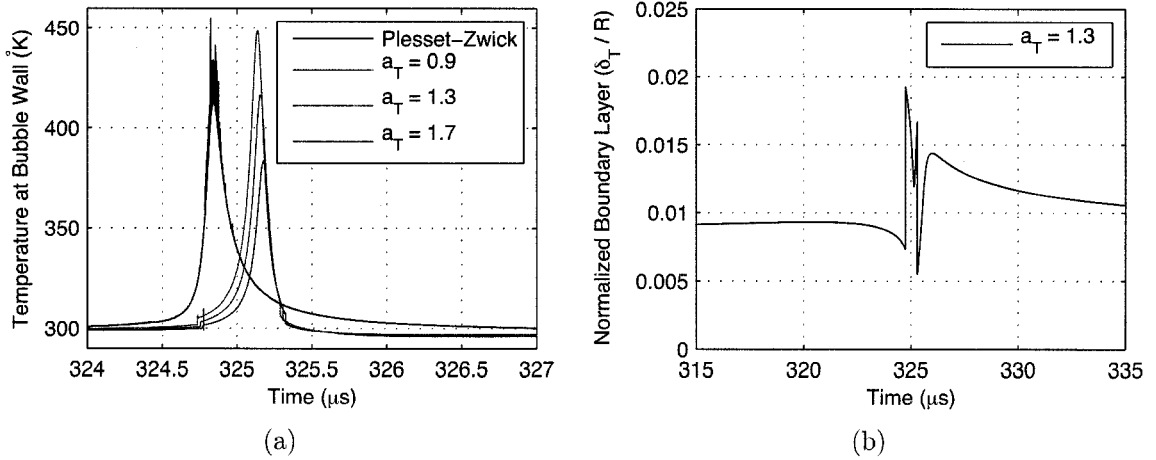
Figure 4.4. Heat transport in the liquid was explored with the present model, comparing the Plesset-Zwick formulation with the scaling approach. In (a) the temperatures at the bubble wall are compared, while a corresponding boundary layer thickness is plotted in (b).

4.2.1 Sonoluminescence Bubbles

Although numerous models of sonoluminescence bubbles have been published, a detailed comparison against all of these models is not the objective here. Rather, we select a particular model that addresses the essential features of heat and mass transfer.[39] In this work, Storey and Szeri implemented one of the most complete models in the literature for violent spherical collapses. Here, we consider 'Case II' analyzed by Storey and Szeri, for which chemical reactions were neglected. Simulations involved a 4.5 μm bubble in 298°K water, while the acoustic excitation was a sine wave with a frequency of 26.5 kHz and an amplitude of 1.2 bar.

Simulation results for bubble radius and vapor content inside the bubble are presented in Figures 4.5 and 4.6. In both figures, Storey and Szeri's plots are provided in part (a), while part (b) comprises results from the present model. In the present model, $a_\theta = 0.5$ and $a_T = 1.3$ were used, while $a_m = 1.3$ was found to provide the best fit for vapor content. From the radius-time plots, both models predict essentially similar behavior with two subtle differences: the maximum radius predicted by Storey and Szeri is slightly larger, while the present model exhibits higher damping of the rebounds. Overall, the radius-time curve
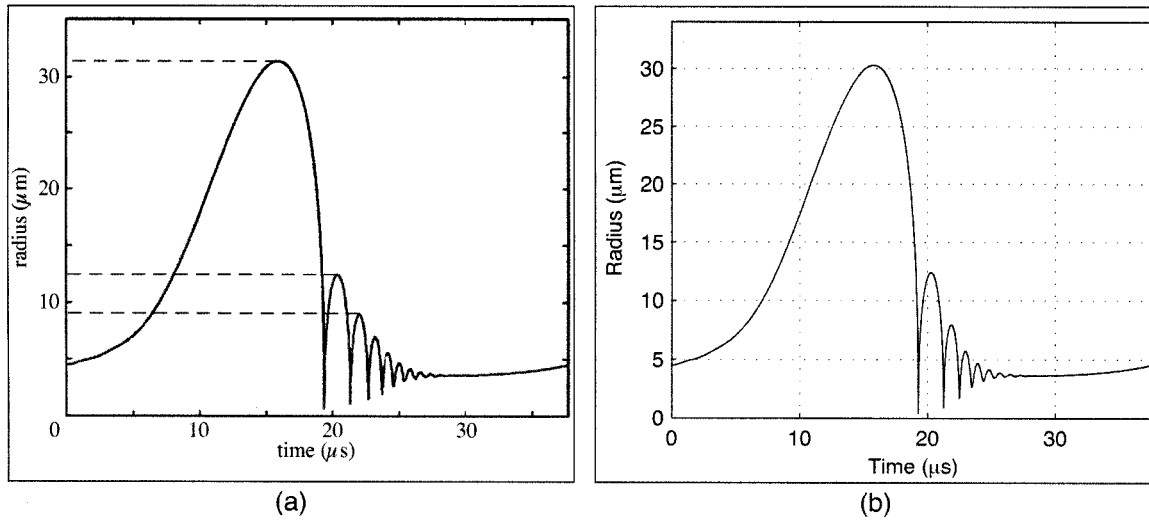
Figure 4.5. Comparison of radius-time curves for a sonoluminescence bubble. Part (a) is reproduced from the work of Storey and Szeri,[39] while (b) is from the present model with $a_\theta = 0.5$, $a_T = 1.3$, and $a_m = 1.3$. The dashed lines in (a) are overlaid on the reproduced plot in order to assist in reading specific values.

was found to be insensitive to a_θ, a_T, and a_m. The discrepancy in maximum radius is likely explained by the use of different static pressures (in the present model, 1.013 bar was used). The damping of rebounds can be considered to be a combination of thermal and acoustic damping. Considering Figure 4.6 for the vapor content, it appears that both models treat vapor trapping similarly. Hence, additional damping in the present model may come from differences either in heat transport (note the consideration of argon versus air), or in the gas equation of state (internal pressure affects acoustic damping), or both. Although Storey and Szeri simulated an argon bubble as opposed to an air bubble, a loose comparison can be drawn with regard to the maximum temperature obtained during the primary collapse. Storey and Szeri calculated a peak temperature of about 9,000°K at the bubble center, while the present model calculates a peak average temperature of about 3,600°K. The higher temperature from Storey and Szeri should be expected on the basis of the lower thermal conductivity of argon as well as the reporting of a center temperature rather than an average temperature.
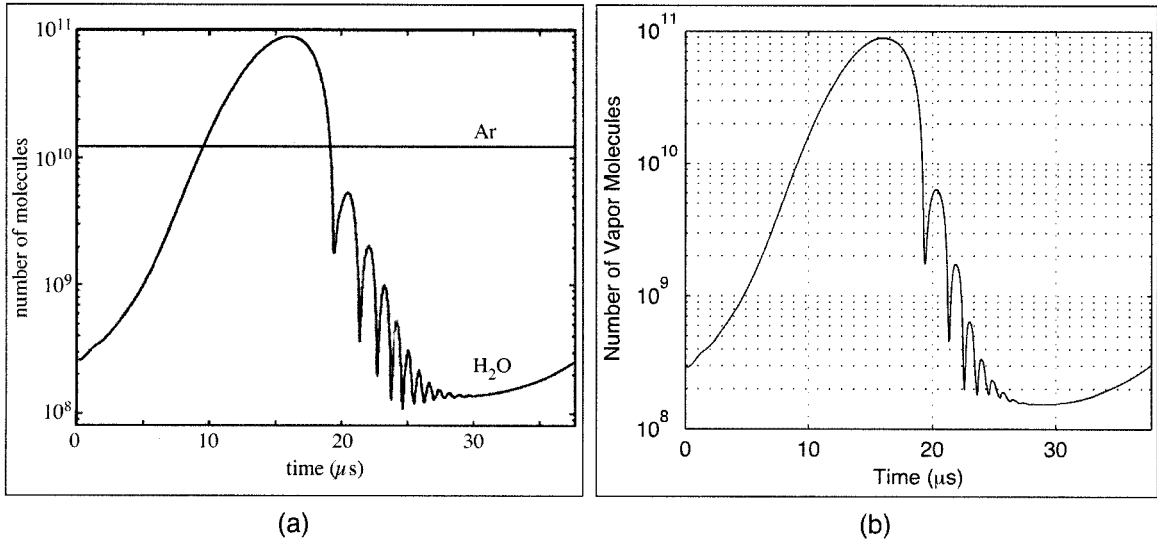
Figure 4.6. Comparison of the calculated number of vapor molecules inside a sonoluminescence bubble. Part (a) is reproduced from the work of Storey and Szeri,[39] while (b) is from the present model.

4.2.2 Lithotripsy Bubbles

Two relevant models from the literature simulated lithotripsy bubbles. Sapozhnikov et al.[10] did not consider heat or vapor transport, but extensively analyzed the diffusion of non-condensable gases. Separately, Matula et al.[36] considered heat and vapor transport, though they did not address heating in the liquid. Calculations from both of these models are discussed below.

Sapozhnikov et al. explored how static pressure and initial bubble radius affect the rectified diffusion of non-condensable gases for bubbles excited by an analytic shock wave. The analytic shock wave was calculated as

$$p = A\, 2e^{-\alpha t} \cos\left(2\pi f t + \pi/3\right) \tag{4.2}$$

where $A = 50$ MPa is the peak positive pressure, $\alpha = 9.1 \times 10^5$ rad/s, and $f = 83.3$ kHz. The published results from Sapozhnikov et al. are reproduced here in Figure 4.7(a). For comparison, analogous calculations from the present model are provided in part (b) of the

figure. To generate these results, the present model considered gas-vapor bubbles with $a_m = 0.1$ for minimal vapor trapping. In addition, the ambient temperature T_∞ was taken as 296.2°K to match Henry's constant as used by Sapozhnikov et al. It is clear from these plots that both models produce essentially the same results with regard to the change in equilibrium radius induced by diffusion. Accordingly, we conclude that the algorithmic simplification for diffusion as described in Section 3.1.2 is warranted.

Moving to the other model,[36] vapor trapping and heat transport in the gas were included for lithotripsy bubbles. They used the above equation for an analytic shock wave (4.2) [$A = 33$ MPa, $\alpha = 3.5 \times 10^5$ rad/s, $f = 50$ kHz] and predicted bubble responses using scaling parameters similar to those used in the present effort. Exemplary results from their model are shown in Figure 4.8(a) and 4.9(a), while parts (b) of these figures provide analogous results from the present model. All model predictions assumed an initial bubble radius of 4.5 μm and an ambient temperature of 298°K; in the present model, vapor trapping was controlled by setting $a_m = 0.3$. From the aforementioned figures, we note that while the radius-time curves agree well, the vapor and non-condensable gas content do not. Regarding non-condensable gases, the present model predicted less diffusion into the bubble (by about an order of magnitude in gas molecules). Similar to the approach used here, Matula et al. employed a convolution solution for diffusion;[76] hence, there is no clear explanation for this discrepancy between models unless a much different Henry's constant was used. As for the vapor curve in Figure 4.9, a qualitative difference between models is apparent. The vapor content 'bounces' during bubble rebounds in the present model, while it appears to level off in steps in the referenced model. This step-like shape can be attributed to additional damping that is not associated with acoustic radiation. Because Matula et al. considered chemistry effects, we infer that the shape of the vapor curve is likely influenced by damping from chemical reactions. Moreover, it is instructive to note that chemical reactions and heat transfer appear in the pressure modulation equation (2.34) as similar energy-sink terms. Overall, this comparison of models implies that similar radius-time curves can be achieved with both, although the balance of damping mechanisms appears to be different in each model.
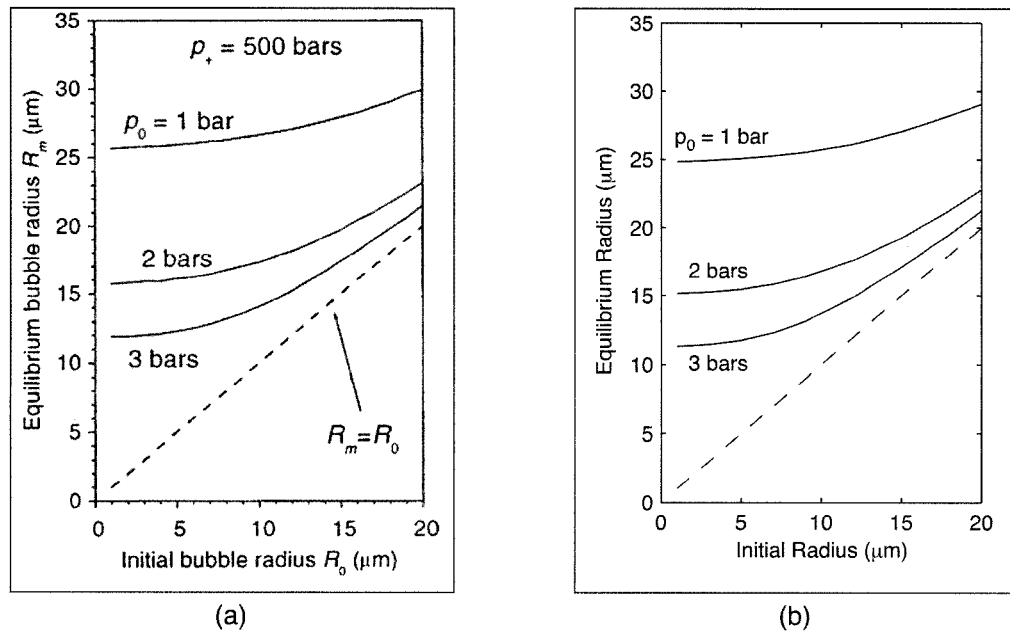
Figure 4.7. Comparison of the rectified diffusion of non-condensable gases for bubbles excited by a lithotripter shock wave. Part (a) is reproduced from Figure 3 in a paper by Sapozhnikov et al.,[10] while part (b) is from the present model. In these calculations, the liquid was initially assumed to be saturated with dissolved air at 1 bar; hence, the initial conditions were 50% and 33% saturated at 2 and 3 bars, respectively.
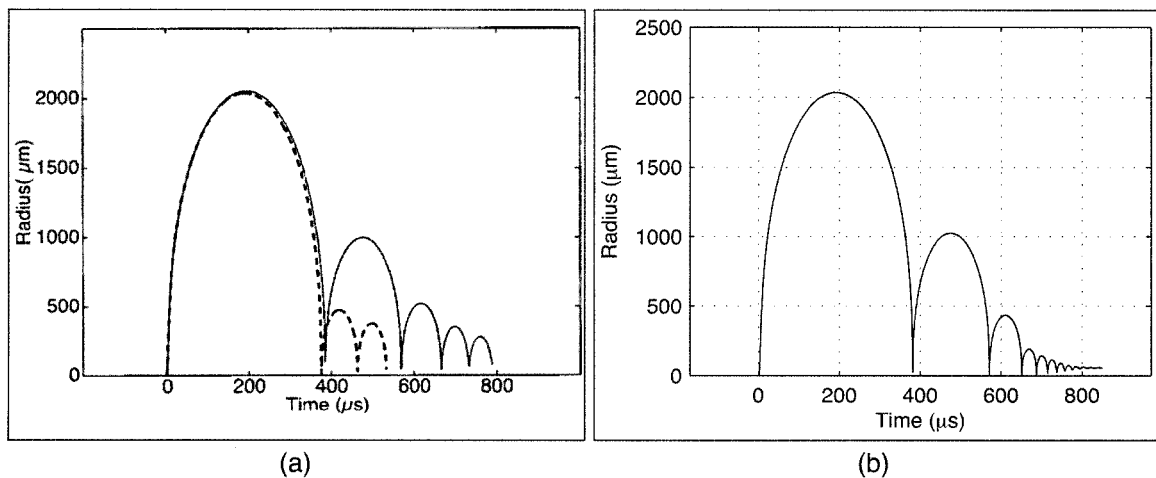
Figure 4.8. Vapor-trapping behavior in bubbles exposed to a lithotripter shock wave. Radius-time curves are compared for (a) calculations performed by Andrew Szeri (plot reproduced from reference[36]), and (b) calculations from the present model with $a_m = 0.3$.

64
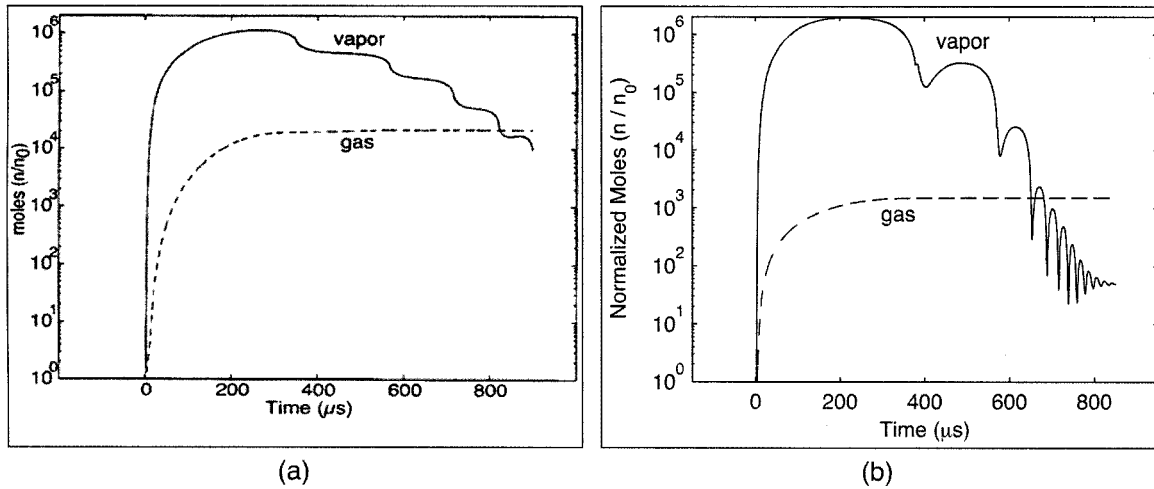
Figure 4.9. Comparison of the vapor and gas content of lithotripsy bubbles. The plot in part (a) is reproduced from the aforementioned paper,[36] while part (b) shows calculations from the present model.

4.3   Energy Loss Mechanisms for a Collapsing Bubble

In previous sections of this chapter, the model formulated and implemented in this effort has been exercised and compared against other published models. First, the scaling parameters governing heat transport (a_θ, a_T) were determined by consideration of Preston's calculated temperature profiles in the gas[32] along with consideration of the Plesset-Zwick convolution. Having discerned scaling factors of $a_\theta = 0.5$ and $a_T = 1.3$, we compared predictions with results from other models in the literature for sonoluminescence and lithotripsy bubbles. These comparisons demonstrate that the present model captures the basic features of heat and mass transport for a single bubble collapse. However, these test cases also suggest a complex interaction of thermal, mechanical, and perhaps even chemical damping mechanisms that affect the radial dynamics.

To help sort out these mechanisms, we now consider two distinct types of collapse: a Rayleigh collapse of a millimeter-sized bubble and a driven collapse of a micron-sized bubble. These collapses can essentially be classified as lithotripsy bubbles and sonoluminescence bubbles, respectively. For the Rayleigh collapse, the relative effects of mass diffusion of vapor (a_m) and thermal coupling of vapor with the liquid (a_T) were explored using the

scaling model [see Figure 4.10(a)]. As is evident from the plotted curves, the rebound is controlled primarily by diffusive trapping of vapor inside the bubble. Such vapor trapping cushions the collapse, thereby affecting the evolution of pressure inside the bubble as well as the radiated pressure. In this manner, most of the energy loss is mechanical during a Rayleigh collapse that resembles a lithotripsy bubble. In addition, the diffusion of vapor is influenced by the ambient liquid temperature, as implied by part (b) of this figure [though not shown in (b), radial dynamics remain insensitive to a_T at higher temperatures]. As an interesting aside, the prominence of mechanical over thermal vapor effects does not apply to sonoluminescence bubbles, as demonstrated by Figure 4.11.

Given the above discussion, the rebounds of lithotripsy bubbles are essentially controlled by acoustic radiation losses. Accordingly, these rebounds can be studied to elucidate diffusion behavior among vapor and non-condensable gas molecules. Indeed, the experimental work discussed in the next chapters was aimed at understanding this diffusion behavior. In terms of the modeling discussed to this point, diffusive vapor trapping can be understood through the scaling parameter a_m. As suggested by Figure 4.10(b), one tool that may be used to experimentally affect vapor trapping is the bulk temperature of the liquid. Similarly, the concentration of dissolved gases in the liquid may affect the diffusive gradients of gas and vapor inside the bubble. Overall, these model predictions suggest an experimental approach whereby vapor trapping is studied by observing the collapse and rebound of lithotripsy bubbles under different test conditions in the liquid.

The aforementioned experimental strategy relies on the distinction of mechanical (a_m) and thermal (a_T) aspects of vapor transport. However, in addition to these vapor transport processes, other damping mechanisms also exist. Although chemical reactions are not expected contribute significantly to the energetics of collapse,[80] heat conduction driven by compressional heating of the gas phase (a_θ) may be significant. Hence, an implicit assumption in the experimental strategy described above is that changes in the bulk liquid temperature and dissolved gas concentration will primarily affect vapor transport processes as opposed to damping processes associated with compressional heating and/or chemical reactions.
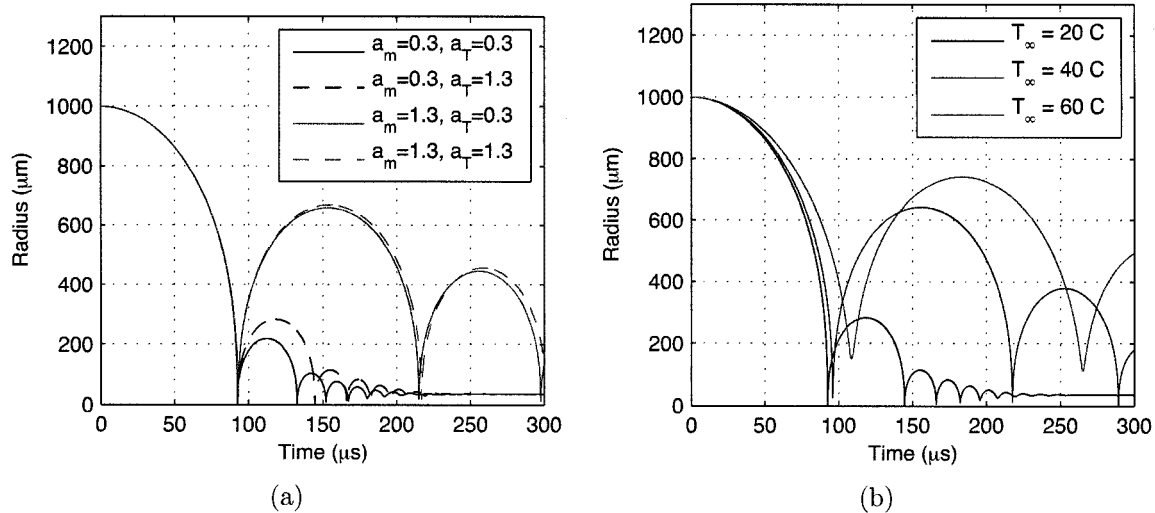
Figure 4.10. Comparison of damping mechanisms for the Rayleigh collapse and rebound of a millimeter-sized lithotripsy bubble. Radius-time curves are plotted in (a) to show the effects of scaling parameters for mass diffusion inside the bubble and temperature changes in the liquid. Additional curves are shown in (b) to elucidate the impact of ambient liquid temperature.
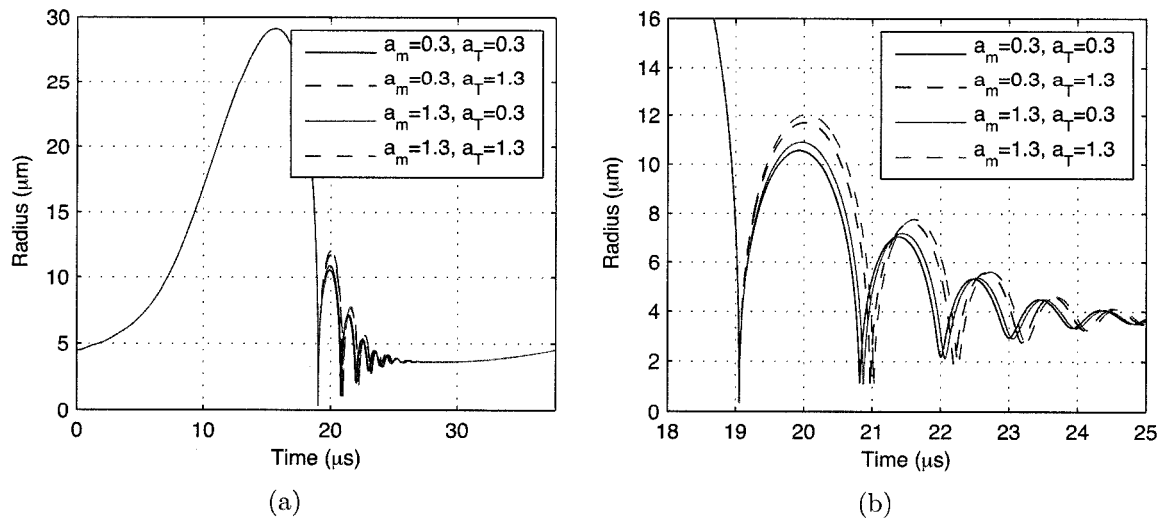
Figure 4.11. Comparison of damping mechanisms for the collapse and rebound of a sonoluminescence bubble. The same radius-time curves are plotted for (a) an entire acoustic cycle, and (b) a zoomed perspective of the rebound. The curves compare the effects of scaling parameters for mass diffusion inside the bubble and temperature changes in the liquid. Except as explicitly noted in the legend, simulation conditions were the same as those from Section 4.2.1.

Chapter 5

EXPERIMENTAL SETUP

In the preceding chapters, a model has been developed for simulating the collapse and rebound of a spherical bubble. The model uses a scaling approach to address heat and mass transport effects, as embodied by the parameters for scaling boundary layer thicknesses: a_m, a_θ, and a_T. In this chapter, an experimental approach and setup are described for testing the role of diffusive vapor trapping, as represented by a_m. As yet, this parameter remains unspecified, while the thermal scaling parameters were determined in Chapter 4. Broadly, the intent of these experiments was to collect data that characterize the collapse and rebound behaviors of bubbles. More specifically, such data were meant to provide insight regarding values of a_m under various test conditions that are relevant to SWL and HIFU.

5.1   Overview of Experimental Design and Setup

The basic strategy was to use a lithotripter shock wave to excite bubble collapses that could be experimentally observed and characterized. Given a shock wave such as that modeled by Equation (4.2), the tensile tail of the shock will excite an extended bubble growth followed by an inertial collapse. Such a response is illustrated by a sample model calculation in Figure 5.1. Because the shock wave ideally lasts for less than about 15 μs, the collapse from maximum radius $R_{max,1}$ should be undisturbed, thereby representing a Rayleigh collapse such as those depicted in Figure 4.10. In many ways, the collapses of lithotripsy bubbles are similar to collapses of laser-induced cavitation bubbles that were discussed in the introduction. However, laser-induced bubbles are created by rather complicated physics associated with the optical breakdown of water, subsequent plasma recombination, and presumably thermal effects that drive bubble growth to its maximum radius. Consequently, the prevailing thermodynamic conditions of the bubble at the start of collapse are not clear.

In contrast, the growth of lithotripsy bubbles is driven only by a tensile acoustic pressure and can be simulated using common modeling approaches such as that used in this effort. Moreover, if the initial bubble size is much smaller than $R_{max,1}$, the dynamics of collapse from $R_{max,1}$ will be insensitive to the initial radius prior to shock-wave arrival.

Given that initial size need not be explicitly controlled, lithotripsy bubbles provide an excellent platform for studying the dynamics of inertial collapses. Characterization of these dynamics can be achieved by measuring the four parameters labeled in Figure 5.1: $R_{max,1}$, $R_{max,2}$, t_1, and t_2. The measurement of maximum radius before collapse provides information regarding the potential energy of the bubble. Together, the maximum radius after collapse and the collapse times provide overlapping information that describes the amount of energy retained through collapse. The overarching goal was to acquire these measurements for lithotripsy bubbles under various conditions. In particular, by conditioning the water at various temperatures and levels of dissolved gases, the dynamics of collapse were investigated as a function of different vapor-gas conditions inside the bubble. As discussed in Section 4.3, these conditions and the corresponding mass diffusion represented by a_m were expected to alter the collapse and the observed rebound.

To collect the aforementioned measurements, a high-speed camera was used in conjunction with passive cavitation detectors (PCDs). The concept of using confocal PCDs to identify the timing of bubble collapse events is based upon the setup employed by Cleveland et al.[81] A functional schematic of the experimental setup is depicted in Figure 5.2. Details of the various setup components are described in detail in the following sections.

5.2 APL-UW Lithotripter

The APL-UW lithotripter used in this effort was designed to simulate the Dornier model HM3. Although this lithotripter exhibits significant shot-to-shot variability as an electrohydraulic device, it was carefully characterized when designed and built.[82] In this device, a spherical shock wave is generated by a high-voltage discharge across electrodes. Because the discharge occurs at one of the geometric foci (F1) of an ellipsoidal reflector, the spherical shock becomes focused at the other geometric focus (F2). The focal region of the APL-UW device is approximately ellipsoidal, where the -6 dB level curves for peak positive pressure
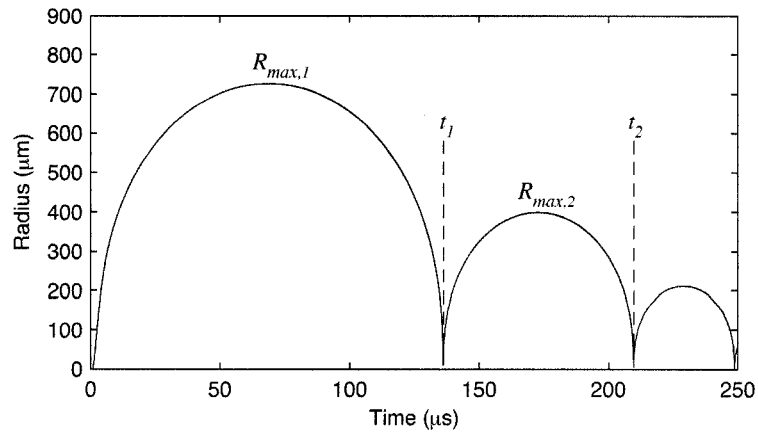
Figure 5.1. Sample radius-time curve for a bubble excited by a lithotripter shock wave.

(a) plan view
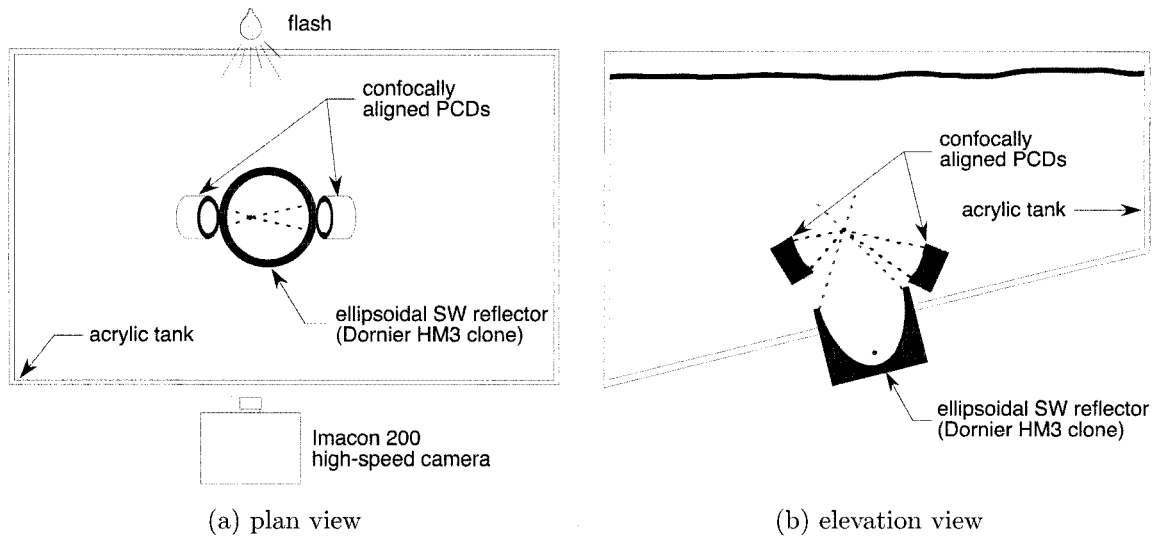
(b) elevation view

Figure 5.2. Schematic of the experimental setup with (a) a plan view lithotripsy tank and (b) an elevation view.

have approximate dimensions of 6 cm in length and 1 cm in width. Input voltages from 12-24 kV produce focal shock waves with peak positive pressures between 25 and 40 MPa and peak negative pressures between -7 and -12 MPa.

5.3 Passive Cavitation Detectors

To detect the collapse times of individual bubbles, two broadband passive cavitation detectors (PCDs) were used. These detectors were fabricated as prototypes at the Center for Industrial and Medical Ultrasound (Applied Physics Laboratory, University of Washington). In particular, the PCDs comprised a sheet of polyvinylidene fluoride (PVDF) film that was 25 μm thick and conformed to a spherical geometry. During construction, the PVDF film was stretched in place by an optical lens, while epoxy was poured on the back side to maintain the spherical shape after curing. The epoxy and a polycarbonate block served as acoustic absorbers to minimize reverberations in the device itself.

The PCDs functioned as spherically focused broadband receivers; both have an aperture of 50 mm, while different radii of curvature provide focal distances of approximately 10 cm and 15.4 cm. The -6 dB focal boundaries were characterized at 3.6 MHz as ellipses with the following length × width characteristics: 17 mm × 1.2 mm for the PCD with 10 cm focal length, and 47 mm × 2 mm for the PCD with 15.4 cm focal length. Geometric characterization of the PCD foci was accomplished by wiring the PCDs as acoustic sources and measuring the output along and transverse to the acoustic axis. These measurements utilized a 'lipstick' hydrophone (Model GL-0150-1A, SEA/Onda, Sunnyvale, CA). For observing bubbles, PCDs were wired as receivers with a built-in preamplifier and were aligned confocally with the lithotripter and with one another. As receivers, the PCDs possess an effective bandwidth up to about 10 MHz. Photographs of a PCD on a table and of PCD alignment in the test tank are shown in Figure 5.3. With the pointers in place as shown in part (b) of the figure, photographs were captured with the high-speed camera to document the PCD locations.

Data from the PCDs were collected on a Tektronix TDS744A digital oscilloscope with a sampling frequency of 50 MHz, DC coupling, 20 mV/division sensitivity, and 50Ω input impedance. One PCD was routed through an analog high-pass filter set at 200 kHz

(Krohn-Hite Model 3202) before being digitally captured on the oscilloscope. This immediate filtering enabled easier interpretation of the PCD signal for immediate evaluation of individual data points. All saved PCD data were downloaded from the oscilloscope over a GPIB connection using a personal computer and a custom LabVIEW program (National Instruments, Austin, TX).

PCDs with both of the aforementioned geometries were used during testing. Although the PCDs were found to be quite robust overall, several failures did occur. Consequently, some data were collected using two long-focus PCDs, other data using both a short- and a long-focus PCD, and yet a few other data points with a single long-focus PCD. Ultimately, the small focal regions and broadband characteristics of these PCDs enabled the identification of individual collapse events from a single PCD trace. By analyzing two PCD traces, even relatively crowded cavitation fields could be evaluated to assign individual collapse events to specific bubbles in high-speed photographs. To assist the correlation of PCD data to photographs, high-speed images of the alignment pointers *in situ* were acquired.

The preceding description of PCDs in this section represents the final evolution of the measurement technique. Initial attempts at these measurements used confocal piezoelectric PCDs.[81] Initial work with this setup demonstrated the limitations of the piezoelectric transducers.[83] The lack of spatial and temporal specificity proved to limit their utility for the current experiment, leading to the adoption of the PVDF devices.

5.4   High-Speed Photography

An Imacon 200 high-speed camera (DRS Technologies, Parsippany, NJ) was used to capture images of bubbles both before and after the primary collapse at time t_1 from Figure 5.1. The camera is capable of capturing a sequence of 14 images at rates up to 200 million frames per second using seven separate charge-coupled devices (CCDs). Each image frame comprises 980 pixels in height × 1200 pixels in width, where each pixel is an 8-bit grayscale value. The captured images served two purposes: spatial characterization of the cavitation field and measurement of the radii $R_{max,1}$ and $R_{max,2}$. First, the photographs enabled selection of data for which single, isolated bubbles were identified and correlated with PCD traces. This selection was very important in that many shock waves produced either no significant
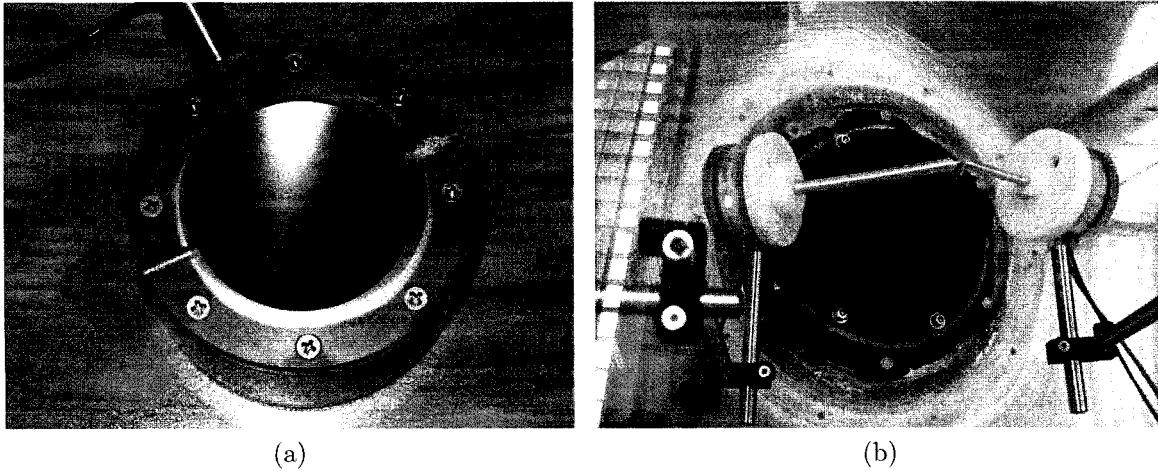
Figure 5.3. Photographs of (a) a passive cavitation detector and (b) passive cavitation detectors as fixtured and aligned in the lithotripter tank using pointers.

bubbles (in the absence of nuclei) or dense clusters of bubbles. Moreover, when sparse groups of bubbles were present, the photographs allowed correlation of pressure spikes in the PCD data to specific bubbles. Second, images of target bubbles were analyzed to estimate bubble radii. Details of both the optical setup used to capture the images as well as the steps taken to calibrate radius measurements are described in the next two sections.

5.4.1   Optical Configuration

The physical setup of the camera and lighting are illustrated in Figure 5.2(a). Bubbles were backlit using light from a non-collimated flash source (Photogenic PowerLight 2500DR, Bartlett, IL). Also, a single sheet of white office paper was taped to the lithotripter tank to diffuse light from the flash. On the camera side, a 105 mm Nikon lens with a PK-13 extender ring was used. The f/stop was set at $f/2.5$ to allow passage of maximum light. This combination resulted in a standoff of about 17.7 in. between the front edge of the 105 mm lens and the acoustic axis of the lithotripter. Moreover, the acoustic axes of the PCDs were also kept in the optical plane of focus. The remainder of the optical settings were adjusted through the software used to control the camera. As such, the internal iris was set at $f/2$, the exposure duration was set at 1 μs, and the gain for each CCD was set
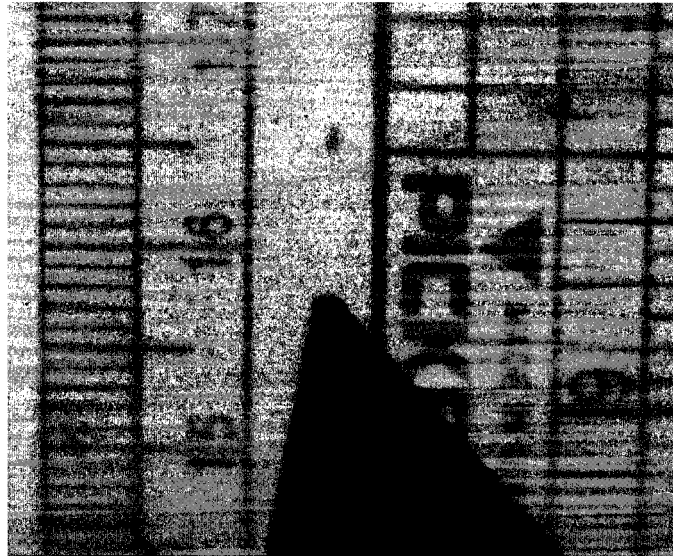
Figure 5.4. Photograph of a ruler at a 45° angle to depict depth of field. The dark pointer in the photograph indicated the acoustic focus of the lithotripter; the ruler mark at 16 cm was approximately above the tip of the pointer.

at zero (the lowest available level).

To quantify the depth of field of this setup, an image of a ruler angled at 45 degrees is provided in Figure 5.4. In this photograph, the mark for 16 cm was approximately at the center of the focal plane. The marks at 15 and 17 cm are noticeably more blurry, though still visible. Accordingly, we conclude that the depth of focus was greater than $2 \text{ cm}/\sqrt{2} = 1.41$ cm. Given that the -6 dB focal region of the lithotripter was stated above to be about 1 cm transverse to the acoustic axis, it is reasonable to expect that any bubbles in the field of view that were excited by the lithotripter would be visible.

5.4.2 Calibration of Bubble Radius

To calibrate measurements of bubble radius from high-speed photographs, an image processing algorithm was developed and calibrated. The algorithm consisted of the following steps:

(1) Interactive selection of a target bubble for analysis. A target square of 150×150

pixels centered at a user-specified 'click' was taken for further processing.

(2) Target pixels were segmented by applying a threshold to identify the edges of the bubble as dark pixels. Due to variability in lighting within frames as well as between frames, the segmentation could not be reliably executed by applying a constant threshold. Rather, pixels in the target square were analyzed using the 'graythresh' function in MATLAB (The MathWorks, Natick, MA) to statistically identify a threshold level. This level was then multiplied by an empirically determined factor of 0.9.

(3) Because the segmented image did not always represent a singly connected region, a morphological closing operation was applied to the segmented binary image. The closing utilized a structuring element in the shape of a 'plus' sign (3 pixels × 3 pixels). After this operation, only the largest pixel region below the threshold value was retained.

(4) A Sobel operator was applied to the binary image for edge detection. The resulting image was a binary outline of the dark pixels that correspond to the bubble edges. Such an outline was a convenient output to be ultimately saved.

(5) The diameter of the bubble was measured in pixels from the outline image by taking the maximum minus the minimum pixel coordinates along the horizontal and vertical axes. The image was then successively rotated by 10 degrees before repeating the diameter measurements. In this fashion, 18 diameter measurements were acquired in 10-degree increments. The actual diameter was taken as the median of collected measurements. Note that the median was used to limit the impact of spurious variations.

Accordingly, the image processing provided a measurement of bubble diameter in pixels. To calibrate this value to physical units, photographs of spheres of known size were captured. More specifically, both glass and nylon spheres were photographed in water, with the same optical configuration described above (see Figure 5.5). The motivation for considering both materials was to use the nylon spheres as a control while investigating the impact of refraction at the glass-water interface.

Both types of spheres had nominal diameters of 3/32 in. Because the photographs were captured by dropping a series of spheres into the camera's field of view in the focal plane, specific images were not matched with explicit measurements of the corresponding sphere. However, a micrometer with a precision of 0.0001 in. was used to measure the diameters of a sample of 20 spheres of each material. These measurements are summarized in Table 5.1. Given that a scaling of 53.2 pixels per millimeter was read directly from a photograph of a ruler, this value was applied to diameter measurements of spheres based on image processing. The results are listed in Table 5.1 and plotted in Figure 5.6.

(a)   (b)
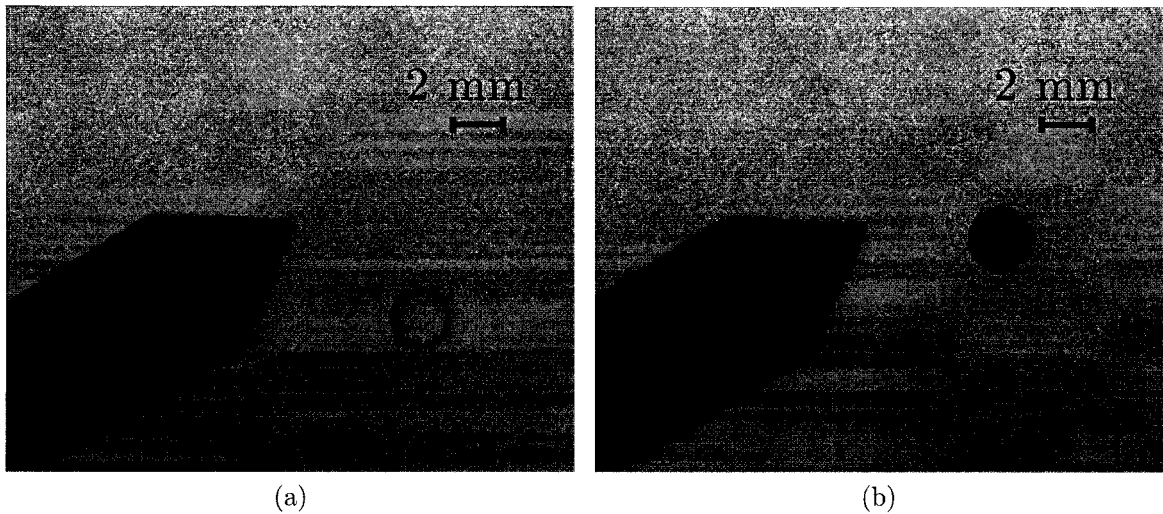
Figure 5.5. Photographic frames captured with the high-speed camera that show (a) a glass sphere and (b) a nylon sphere. The dark bar in each photo is the lithotripter pointer and was used to aid alignment of the spheres in the camera's focal plane. In conjunction with a grayscale thresholding algorithm, these photographs enabled calibration of spherical size since both types of spheres had a known radius near 1.2 mm.

In the table, standard deviations are calculated as percentages of mean radius, while the estimated error of the image processing algorithm is referenced to the micrometer measurements. Also, noting the presence of 14 frames per sequence, the listed number of sequences/frames indicates that several frames were omitted from the statistical analysis as outliers with poor image segmentation characteristics. The failures of the processing algorithm in these few frames were caused either by impingement of the bubble on the boundary of the 150×150 pixel target region or by a lack of a singly connected segmentation image. Such artifacts were obvious in the data and did not propagate through analyses of actual bubbles. Ultimately, these data demonstrate that the image processing algorithm effectively adapted to variable lighting conditions. Moreover, because the physical scaling read from an image of ruler was consistent with the actual sphere diameters to within about 2% for both materials, it is reasonable to conclude that light refraction and diffraction effects were negligible for images of spheres with about a 1 mm radius. Consequently, a scaling of 53.2 pixels/mm was used for all image processing, while an accuracy of about 2% was expected for measurements of bubble radii.

Table 5.1. Measurements of sphere diameters.

Micrometer Measurements

	Mean Radius (mm)	Standard Deviation
Glass Spheres (20 measurements)	1.1923	0.04%
Nylon Spheres (20 measurements)	1.1740	0.6%

Image Processing Measurements (53.2 pixels/mm)

	Mean Radius (mm)	Standard Deviation	Error
Glass Spheres (27 frames, 2 image sequences)	1.217	0.5%	+2.1%
Nylon Spheres (54 frames, 4 image sequences)	1.176	0.8%	+0.2%

5.5 Maintaining and Measuring Water Conditions

A final component of the test setup was a water system capable of heating and degassing about 90 gallons of water. To meet the needs of this experiment, a water system was designed and constructed, as depicted in Figure 5.7. This system included the following components:

- Liqui-Cel 4×13 membrane contactor (Membrana, Charlotte, NC) to provide a high contact surface area for a flowing liquid, thereby facilitating gas exchange to/from the liquid.

- Vacuubrand MZ 2C pump with ultimate vacuum rating of 6.8 torr (BrandTech Scientific, Inc., Essex, CT). In conjunction with the membrane contactor, dissolved oxygen levels below 3% of saturation were obtained in water.

- Mechanical filtration using two filters in series: a Claris series cartridge (1 μm nominal pore size) preceding a Nexis C-series cartridge with an 2 μm absolute rating (Pall Corporation, East Hills, NY).
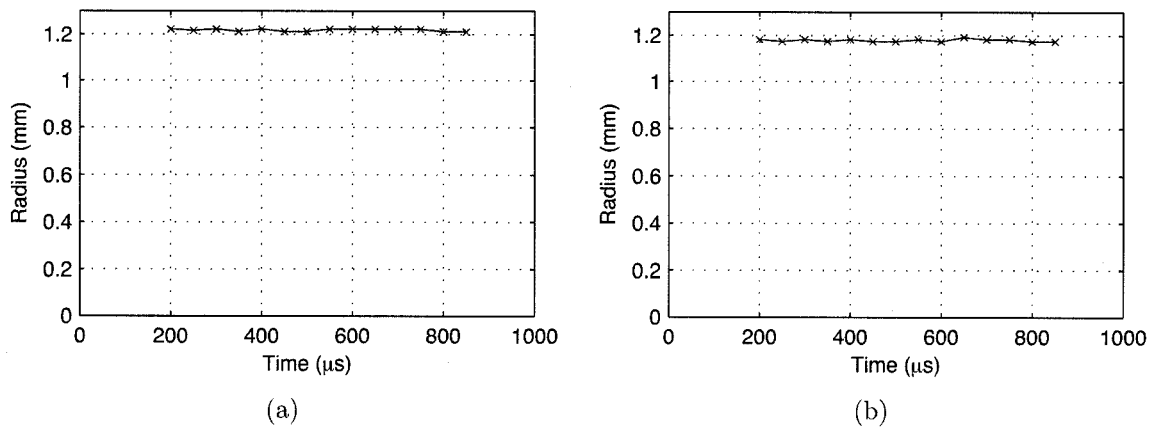
Figure 5.6. Calibrated measurements of sphere radius from a series of high-speed photographs of (a) a glass sphere and (b) a nylon sphere. Each red 'x' indicates a measurement from a single frame while the blue lines connect measurements.

- Stainless steel circulation heater with 4.5 kW capacity (Gaumer Company, Inc., Houston, TX).

These elements were connected using 3/4 in. stainless steel tubing and Swagelok tube fittings (The Swagelok Company, Solon, OH). A 1 hp centrifugal pump was used to drive the flow and was capable of achieving flow rates up to 10 gpm.

While this system enabled control of the water used in the lithotripter tank, water conditions were measured and recorded in a notebook roughly every hour during testing. First, water conductivity was measured with a Model EP conductivity meter (Myron L Company, Carlsbad, CA). Table salt was added to tap water to reach the desired conductivity of 600 μS/cm for initiating the spark. In addition, water temperature and dissolved oxygen content were measured using an Oxi 330i meter with a CellOx 325 probe (WTW Wissenschaftlich-Technische Werkstätten GmbH, Wellhelm, Germany). Lastly, because temperatures above 50°C exceeded the range of the dissolved oxygen meter, such temperatures were measured with a type K thermocouple and a Fluke 179 multimeter. To acquire dissolved oxygen measurements at these temperatures, two approaches were used. In the first approach, the dissolved oxygen concentration (not the saturation percentage) was controlled to reach a level that would be consistent with the target saturation percentage at 60°C. During heating and cooling from 50°C to 60°C and back again, diffusion was

minimized by covering the surface with floating polypropylene balls. The major drawback of this approach was the substantial amount of time involved in the heating and cooling; hence, measurements of dissolved oxygen were not temporally specific, requiring estimation of the applicable values during the test. A second and improved approach was developed whereby a 400 mL sample of water was collected in a plastic beaker from the surface of the tank. This sample was immediately covered in aluminum foil to minimize the liquid surface area and was cooled in a water bath for about 10 minutes. Then, a dissolved oxygen measurement was acquired in terms of absolute concentration, which was later converted to a saturation level at 60°C. Note that such a measurement required active stirring of the sample and that measurable diffusion into such a small volume occurred within tens of seconds. Consequently, the recorded measurement was the lowest reading achieved rather than an equilibrium reading. Ultimately, consistent readings were obtained with the latter approach.

A summary of the nominal conditions tested and the range of acquired measurements for each test case is provided in Table 5.2. This matrix includes 9 test cases, including all permutations of temperature at 20°, 40°, or 60° coupled with dissolved oxygen content at 10%, 50%, or 85% of saturation. In general, temperature was controlled to the nominal target ±1°C. The measurements of dissolved oxygen exhibited somewhat more scatter, especially at 60°C. However, because these measurements were acquired within several inches of the water's surface, the actual changes at the lithotripter's focus were likely much less (the focus was about 18 in. beneath the surface). With the exception of Case I, the dissolved oxygen content was controlled to the target level ±5%, where these bounding tolerances are conservative.

During the testing of Case I, an interesting phenomenon was observed. Despite dissolved oxygen levels measured to be below saturation, quasi-static bubble growth was observed on surfaces inside the tank. Explaining this observation requires a discussion of the path by which the water was brought to its measured state at 60°C. First, at a temperature near 40°C, the water was degassed to achieve a saturation level of about 71%. Assuming that this concentration was achieved by enforcing equilibrium conditions at the membrane contactor, other gases including nitrogen, argon, and carbon dioxide were also at 71% saturation at

40°C. To check if any of the aforementioned gases could become supersaturated at 60°C, a relevant parameter is the ratio of solubility at 60°C to that at 40°C. Using correlations from the CRC Handbook,[84] we note that this ratio is 0.68 for carbon dioxide, 0.82 for argon, 0.84 for oxygen and 0.88 for nitrogen. Because the ratio for carbon dioxide drops below the original saturation percentage at 40°C, it is evident that supersaturation of carbon dioxide likely explains the observed bubble growth. Although this phenomenon can be understood through a few quick calculations, the behavior was nonetheless surprising. As a consequence of carbon dioxide supersaturation, it was very difficult to limit the presence of bubble nuclei for Case I. Accordingly, most of the data collected under these approximate conditions involved the presence of many bubbles, thereby making the study of single-bubble dynamics very troublesome. Hence, these data should be interpreted with caution.

Based on the above discussion of carbon dioxide, it is instructive to consider the extent to which dissolved oxygen measurements consistently reflect the state of dissolved gases in water. A cursory examination of the solubilities of argon, oxygen, and nitrogen suggests that dissolved oxygen levels should remain representative of the solute levels of each of these gases. Although the solubility of carbon dioxide exhibits a markedly different behavior with changes in temperature, the scarcity of carbon dioxide in fresh air implies that these effects are relatively minor with regard to the overall levels of gas dissolved in water. Consequently, dissolved oxygen measurements are retained as a representative indicator of dissolved gas content for the purposes of this effort.
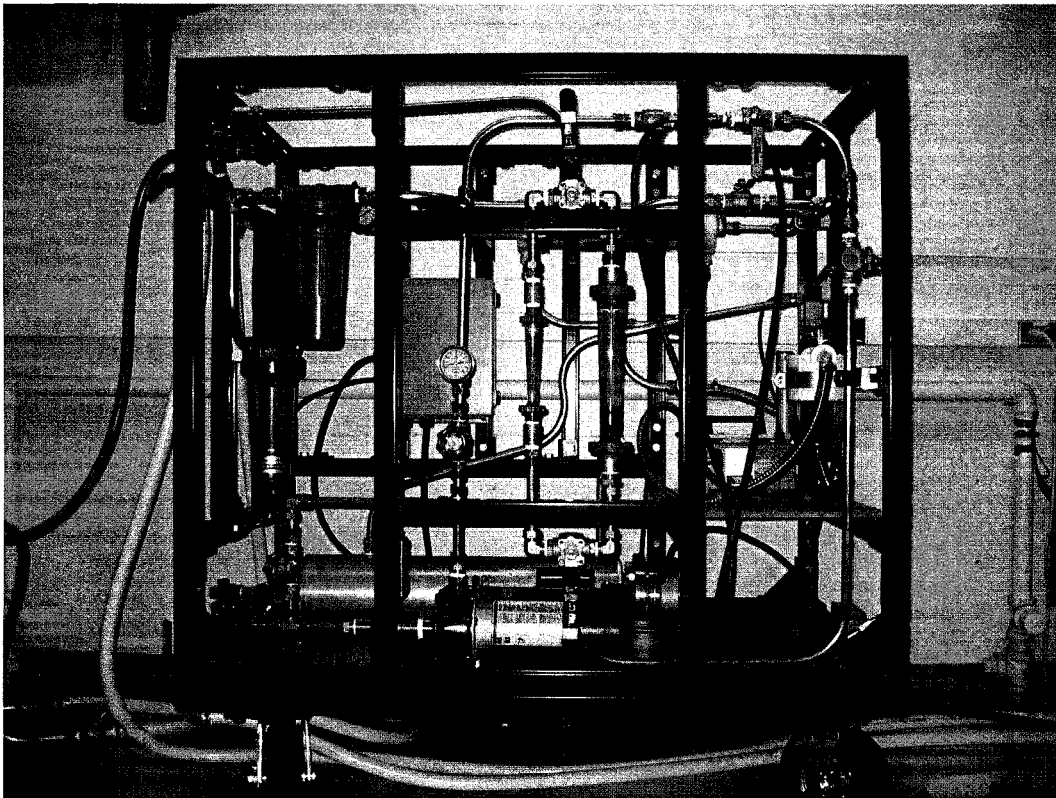
Figure 5.7. Photograph of the water system.

Table 5.2. Experimental test conditions.

| Temperature | Dissolved O_2 Content | | |
	10%	50%	85%
20°C	**Case A** [min: 18.5°C, 7.4%] [max: 19.6°C, 9.6%]	**Case B** [min: 19.5°C, 47.3%] [max: 21.5°C, 50.4%]	**Case C** [min: 19.7°C, 79.0%] [max: 21.4°C, 84.3%]
40°C	**Case D** [min: 39.5°C, 7.8%] [max: 40.6°C, 10.6%]	**Case E** [min: 39.3°C, 47.1%] [max: 40.4°C, 49.1%]	**Case F** [min: 38.5°C, 81.0%] [max: 40.4°C, 83.7%]
60°C	**Case G** [min: 59.6°C, 8.5%] [max: 61.6°C, 14.4%]	**Case H** [min: 59.0°C, 48.8%] [max: 61.1°C, 56.2%]	**Case I** [min: 58.1°C, 69.1%] [max: 61.2°C, 79.3%]

Chapter 6

EXPERIMENTAL RESULTS

The previous chapter describes the instrumentation and physical setup used to study the collapses and rebounds of lithotripsy bubbles. These experiments were designed to elucidate the impact of diffusion among vapor and gas molecules on the dynamics of collapse. More specifically, test conditions were designed to manipulate the bubble's gas-vapor state during collapse by varying the temperature and dissolved gas content of the ambient water. The matrix of conditions tested is listed in Table 5.2. In this chapter, the experimental results are presented and analyzed. First, the methodology for analyzing PCD data in conjunction with high-speed photographs is described; also, sample data are shown for illustrative purposes. Next, the compiled results from all collected data are presented. Finally, the results are discussed and interpreted in the context of the model described in earlier chapters.

6.1 Data Processing and Sample Data

Observations of the collapses and rebounds of lithotripsy bubbles were made with both high-speed photography and with passive cavitation detection (PCD). Data from both sources were analyzed in tandem to reconstruct the behavior of a target bubble in the cavitation field for each 'shot.' Here, 'shot' refers to each collected data point, which in turn corresponds to the passage of a single lithotripter shock wave. In the subsections below, details of the data processing are described and sample data are presented.

6.1.1 Analysis of Image Sequences

A first step in the data processing was segmentation of high-speed image sequences using the image processing algorithm described in the last chapter. For two separate shots, the results of image segmentation and estimation of bubble radius are shown in Figure 6.1. Each outlined box corresponds to the analyzed target region from the original photograph.
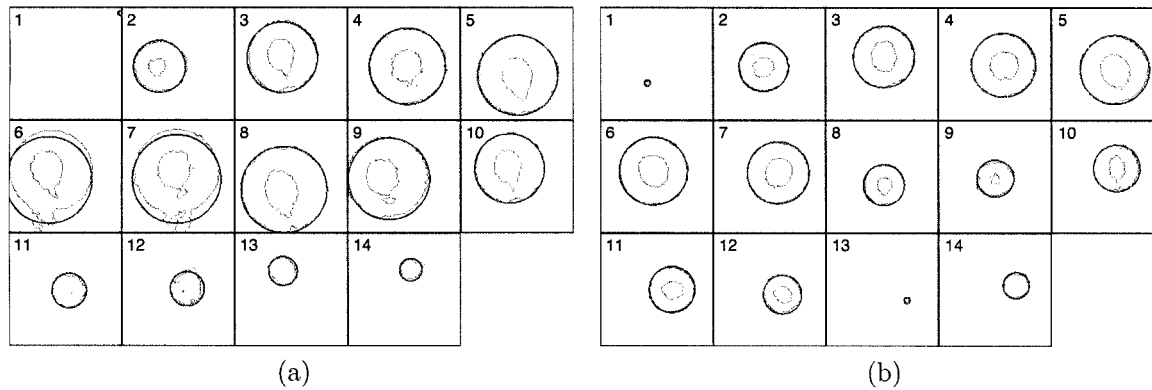
Figure 6.1. Sample images of segmentation results and estimated bubble radius for image sequences of a bubble from (a) Case A conditions [reference shot #46] and (b) Case H conditions [reference shot #57]. For each bubble, the outlined boxes represent the target region analyzed in each frame of the sequence—frame progression goes left-to-right, top-to-bottom. For each frame, the red tracing denotes the segmented region corresponding to the bubble boundary, while the overlaid blue circle represents the estimated bubble radius based on the segmentation.

Moreover, the sequence of image frames progresses from left-to-right, top-to-bottom. The red tracing in each frame outlines the segmented region that defines the bubble boundary; the blue circle represents the estimated bubble radius. For reference, the photographic sequences that correspond to data in Figure 6.1 are provided below in Figures 6.2 and 6.3. In these figures, the raw photographs were modified to include time stamps as well as highlighted ellipses that mark the -6 dB focal regions of the PCDs. These highlights assisted in the interpretation of PCD data.

From frames 6 and 7 of the sequence in Figure 6.1(a), it is clear that a small nearby bubble was included in the segmentation, thereby distorting the radius estimate. In such instances, corrections to the affected frames were made manually; the segmented image was imported into a vector graphics program to determine an approximate length scaling between the estimated blue circle and the red tracing. From the bubble radius estimates, radius-time curves were plotted (see Figure 6.4). Note data points of zero radius were included at the times when bubble collapses were detected in PCD data. For reference, the corresponding PCD traces are provided in the next section in Figure 6.5.
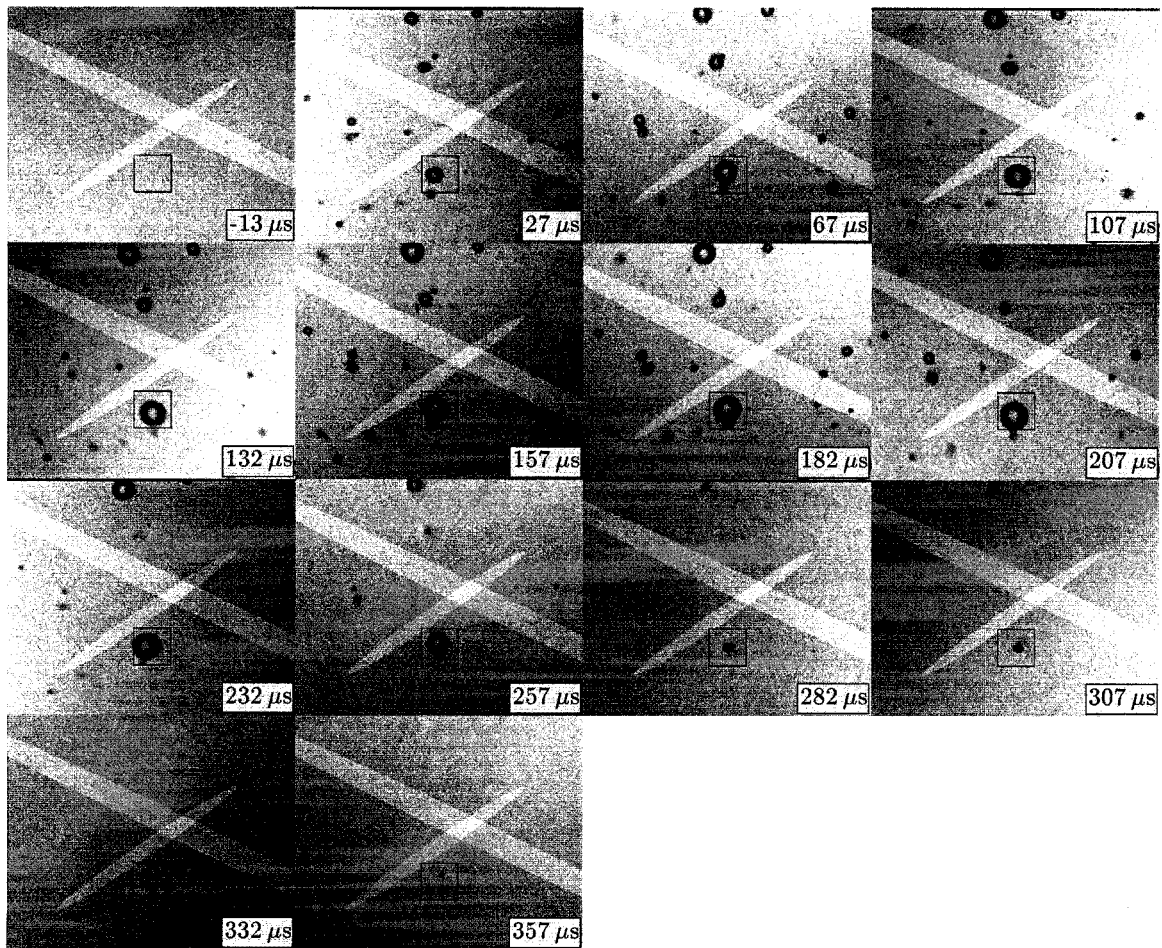
Figure 6.2. Sequential images of bubbles [reference: Case A, shot #46]. Each frame includes a time stamp, two highlighted regions, and a square box outlining a target bubble for analysis. In the referenced time scale, the shock wave arrived at the center of the field of view at time zero. The highlighted regions each correspond to the -6 dB sensitive region of a PCD. The box is 2.8 mm on all sides.

6.1.2 PCD Traces

As mentioned in the last chapter, PCD data were captured on a digital oscilloscope at a sample rate of 50 MHz. When two PCD traces were simultaneously acquired, one of them was passed through an analog high-pass filter at 200 kHz. Because bubble collapses inherently induced high-frequency spikes in the PCD signal, the high-pass filter 'cleaned up' the trace for real-time viewing on the oscilloscope. This approach aided data acquisition
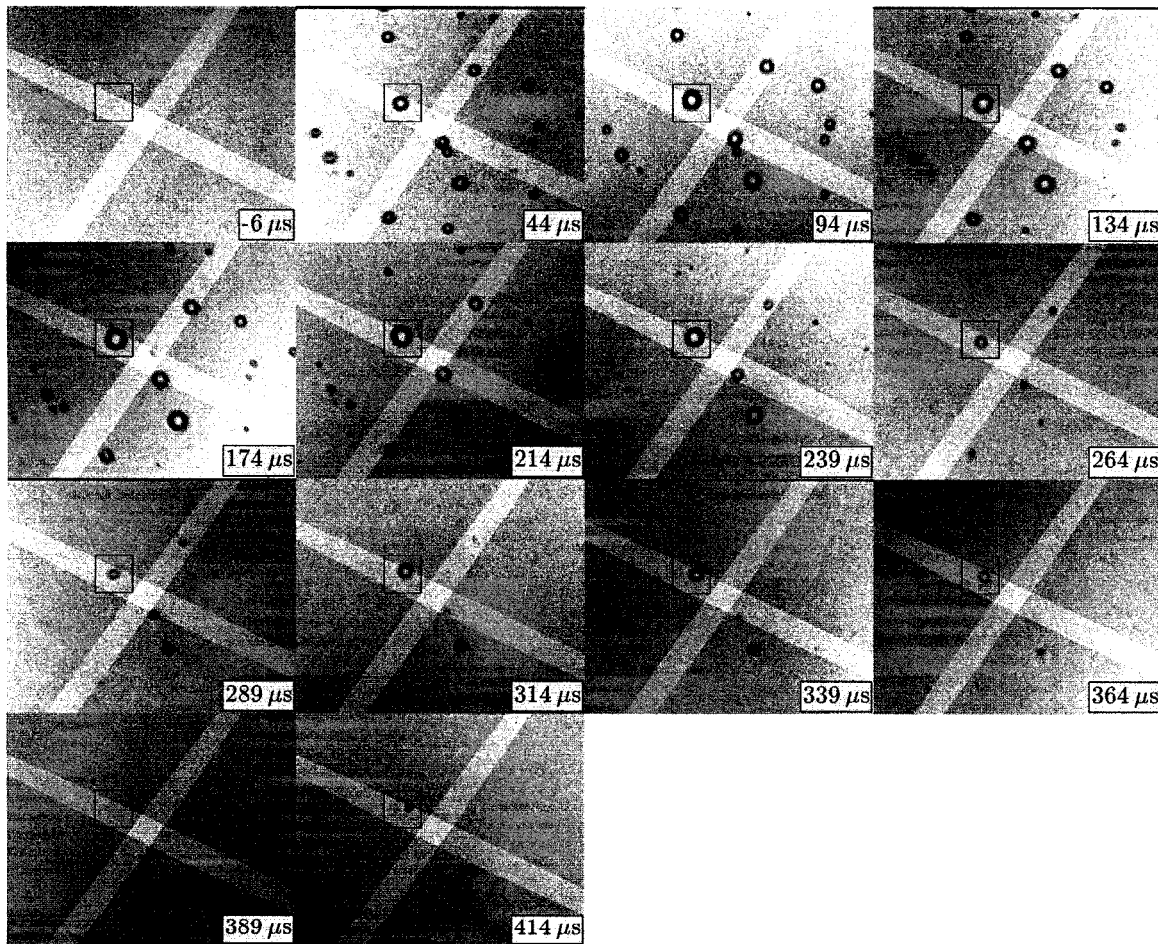
Figure 6.3. Sequential images of bubbles [reference: Case H, shot #57]. Each frame includes a time stamp, two highlighted regions, and a square box outlining a target bubble for analysis. In the referenced time scale, the shock wave arrived at the center of the field of view at time zero. The highlighted regions each correspond to the -6 dB sensitive region of a PCD. The box is 2.8 mm on all sides.

by providing immediate feedback regarding the quality of the PCD data; accordingly, data were not saved when the PCD data could not be interpreted relative to the behavior of a single bubble in the photographs. The saved PCD data were processed further offline, using the following steps for each trace:

(1) The time scale was shifted to account for acoustic propagation delays, such that time zero indicated the arrival of the shock wave at the center of the field of view of the high-speed camera. To estimate the appropriate time shift, the following focal lengths
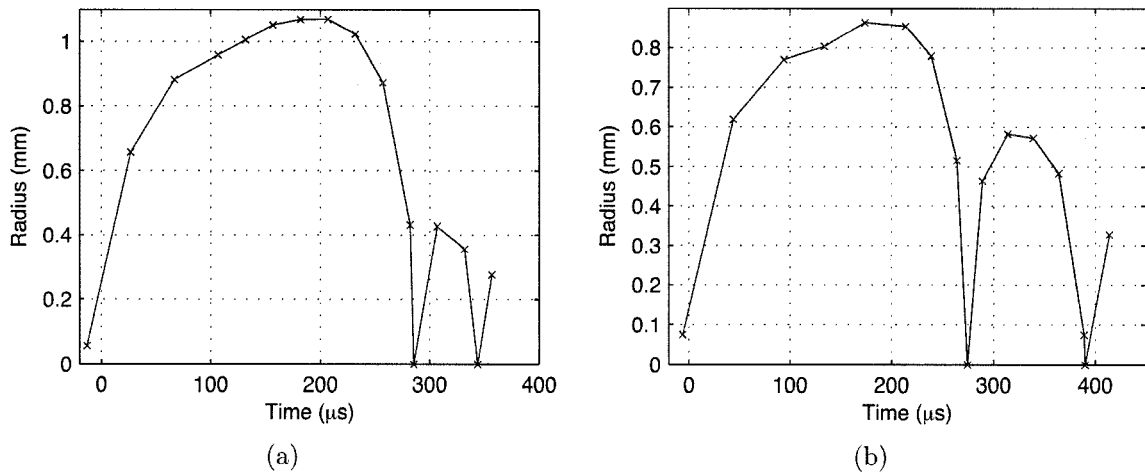
Figure 6.4. Radius-time curves derived from image sequences of a bubble from (a) Case A conditions [reference shot #46] and (b) Case H conditions [reference shot #57]. Each red 'x' indicates a measurement from a single frame while the blue lines connect measurements. Note that measurements from image frames were supplemented by the PCD data in these plots—at measured collapse times (see Figure 6.5), a radius of zero was assumed and plotted.

were used in conjunction with the sound speed of water as a function of temperature: 276 mm for the propagation of the focused shock wave, 94.5 mm for the focal length of the 10 cm PCD, and 156 mm for the 15.4 cm PCD. The focal lengths of the PCDs were adjusted from nominal values to most consistently match the bubble-collapse timings observed in photographs.

(2) Data captured through the analog Krohn-Hite filter were deconvolved in the frequency domain using an experimentally determined impulse response of the filter.

(3) The signals were bandpass filtered between 800 kHz and 3 MHz with a 200th-order finite impulse response (FIR) filter. These bandpass frequencies were chosen to maintain good temporal resolution for discerning the timing of individual collapse events while removing much of the high-frequency noise.

For the shots documented above, the processed PCD traces are provided in Figure 6.5. In these plots, the blue curve corresponds to the highlighted region going from lower-left to upper-right in Figures 6.2 and 6.3, while the red curve is from the other PCD. The vertical green lines denote the timing of frame acquisition for the high-speed photographs. Note that the traces were normalized to the maximum signal level to 'zoom in'; consequently, the background noise appears larger when the measured collapse signal was weak. From the figure, a persistent source of periodic noise is apparent on both blue and red curves. Upon
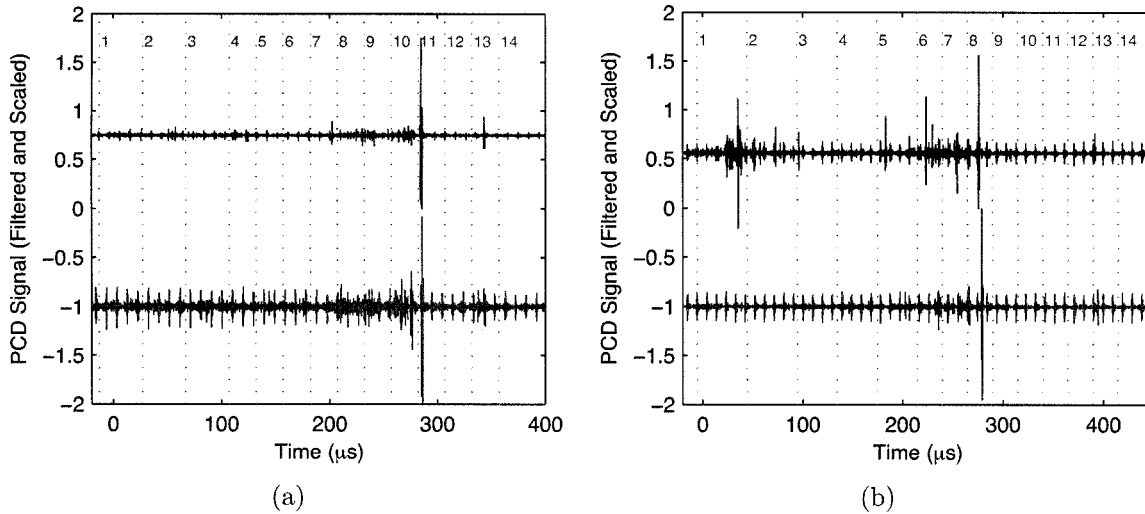
Figure 6.5. Sample PCD traces corresponding to a shock wave under (a) Case A conditions [reference shot #46] and (b) Case H conditions [reference shot #57]. In each plot, the blue and red traces represent simultaneously acquired data from two PCDs. The plotted traces were bandpass filtered and individually scaled such that the maximum amplitude of each signal remained less than 1. The traces were offset vertically for clarity. The time scale was adjusted such that the shock-wave arrived at the lithotripter's focus at time zero.

closer examination, the noise can be characterized as a 5 MHz ringing that recurred with a frequency of about 113 kHz. This noise seems to have been caused by electromagnetic interference from the lithotripter itself. In particular, recharging of the high-voltage power supply after ignition of a shock wave was a likely source of the interference.

Given that the aforementioned noise is understood to be independent of cavitation activity, the trace in Figure 6.5(a) can be easily interpreted. The dominant bubble collapse occurred just after frame 11 from the image sequence of Figure 6.2. Moreover, the subsequent bubble rebound ended with another collapse about midway between frames 13 and 14.

6.1.3   Normalization of Bubble Rebounds

Using the captured image sequences in addition to the PCD data, bubble rebounds were quantified by normalizing the rebound amplitude to the maximum radius obtained before collapse. This normalization approach was identified and adopted independently in this ef-

fort, though the same approach had been used previously to study asymmetric collapses.[43,44] Considering the maximum radii before and after collapse as depicted in Figure 5.1, we can express a normalized rebound radius as $R_{max,2}/R_{max,1}$. Considering that the bubble's energy at these maxima is a potential energy due to volumetric expansion against the ambient liquid pressure, the corresponding volumetric ratio $(R_{max,2}/R_{max,1})^3$ represents the fraction of energy retained through collapse.

In order to normalize the data for comparison of rebounds, $R_{max,1}$ and $R_{max,2}$ must be estimated. The initial maximum $R_{max,1}$ can only be estimated based on the image data and the calibrated processing algorithm described above. However, two possibilities exist for the rebound maximum: direct estimation based on the same image processing or indirect estimation based upon the timing of the bubble collapses t_1 and t_2 from Figure 5.1. From these collapse times, the maximum rebound radius can be approximated by assuming that the dynamics are controlled by the inertia of the liquid and that time and maximum radius are related by the Rayleigh collapse time of a vapor cavity.[85] As such, $R_{max,2}$ is calculated as

$$R_{max,2} = \frac{t_2 - t_1}{2} \left(\frac{1}{0.915}\right) \left(\frac{p_0 - p_v}{\rho_0}\right)^{1/2} \tag{6.1}$$

where ρ_0 is the liquid density, p_0 is the hydrostatic liquid pressure, and p_v is the vapor pressure of the liquid at the ambient temperature.

Although both methods of experimentally determining $R_{max,2}$ ideally lead to the same result, the presence of geometric asymmetry in the bubble collapse complicates the issue. Vogel and Lauterborn studied the collapses of bubbles near a solid boundary to elucidate the impact of asymmetry.[43,44] Of pertinence to the present discussion, they found that the introduction of asymmetry lengthens the effective Rayleigh collapse time. Consequently, use of Equation (6.1) would overestimate $R_{max,2}$ when asymmetries are present. To account for these effects, Vogel and Lauterborn introduced a correction factor k as the ratio of the estimated rebound maximum based upon collapse times to the actual rebound maximum. As a function of the bubble standoff from a solid boundary, they experimentally determined this ratio for both the initial collapse from $R_{max,1}$ as well as for the ensuing rebound. For convenience, their results are reproduced here in Figure 6.6, where k_1 is the ratio for the

initial collapse and k_2 applies to the subsequent rebound. These results suggest that as the bubble collapse becomes more symmetric (as measured by increased standoff from the solid boundary), both k_1 and k_2 approach unity. However, k_2 does increase significantly as the bubble approaches the boundary and the collapse is less symmetric.

In deciding how to estimate $R_{max,2}$ from the acquired data, the merits of both methods need to be evaluated. To this end, it is instructive to first note the types of bubble collapses that were observed. In addition to the essentially symmetric collapses and re-bounds exemplified by the images in Figures 6.2 and 6.3, many of the collapses exhibited clear asymmetries in the form of a visible re-entrant jet. Examples of such collapses and rebounds are provided below in Figures 6.7 and 6.8. Although no nearby solid boundaries were present in these experiments, the presence of other bubbles represents an analogous asymmetry. As discussed above, such asymmetries likely affected the estimation of $R_{max,2}$. However, estimates of $R_{max,2}$ based on image analysis have other inaccuracies. The presence of a re-entrant jet implies that an estimate based on the image segmentation algorithm would overestimate the radius because the assumed bubble volume included a liquid jet. A countereffect is that the radius may be underestimated due to low sampling of image frames during the rebound. Lastly, when bubble rebounds were small enough, it is unclear how well the calibrated image processing algorithm performed; however, because such rebounds appeared as 'smudges' rather than bubbles with well defined boundaries, radii may have been overestimated in these instances.

Given the various uncertainties associated with determining $R_{max,2}$ from either PCD or image data, a coherent strategy was necessary to consistently normalize bubble rebound data. The strategy adopted in this effort was to use the lowest available estimate for $R_{max,2}$. The logic behind this approach is that PCD data should not underpredict the maximum radius, as demonstrated by the data from Vogel and Lauterborn. On the other hand, it is reasonable to expect that the PCD data can overpredict the maximum radius; hence, a lower estimate based on the image data should be accepted. Ultimately, this approach addressed the primary issue raised in Figure 6.6, wherein k_2 can deviate significantly from unity for relatively asymmetric collapses. For most of the data analyzed, the estimates of $R_{max,2}$ from image data were smaller and were therefore used for normalization. The
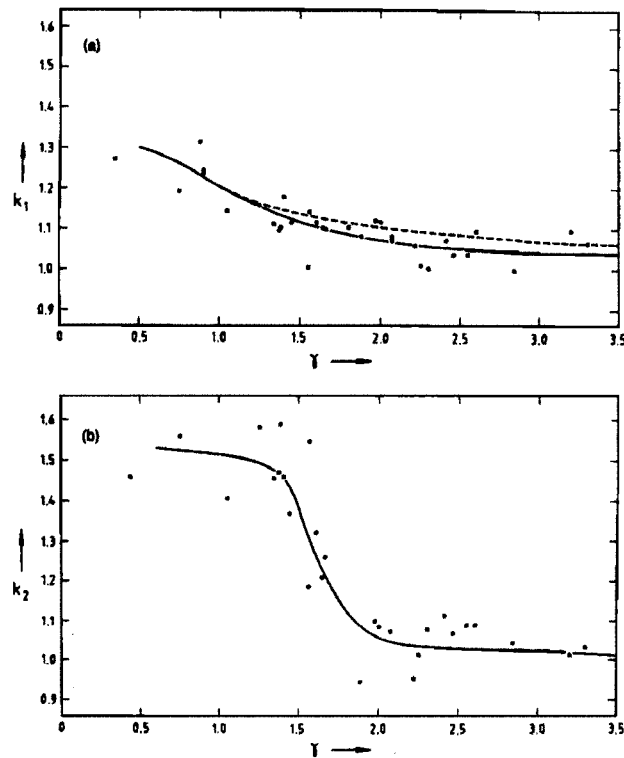
Figure 6.6. Reproduction of Figure 16 from Vogel and Lauterborn.[43] Above, γ is the bubble standoff from a solid boundary and is nondimensionalized relative to the initial bubble radius; $\gamma = 1$ indicates that the bubble was just touching the wall prior to its initial collapse. k_1 and k_2 are ratios of asymmetric bubble collapse times relative to the ideal Rayleigh times from Equation (6.1)–the subscripts '1' and '2' respectively denote the initial collapse and the rebound.

only conditions under which PCD data consistently produced lower estimates involved very small bubble rebounds. As noted above, it is likely that the image processing algorithm performed poorly and overestimated the radii of small, 'smudge-like' bubbles.

6.2 Compiled Results

In conducting experiments to acquire the desired test data, several important characteristics of the actual test conditions were identified and studied. These studies involved the acoustics associated with shock-wave propagation and reflection inside the test tank as well as interactions among multiple bubbles. Eventually, details of test execution were refined to enable the acquisition of consistent and repeatable data regarding the collapses and re-
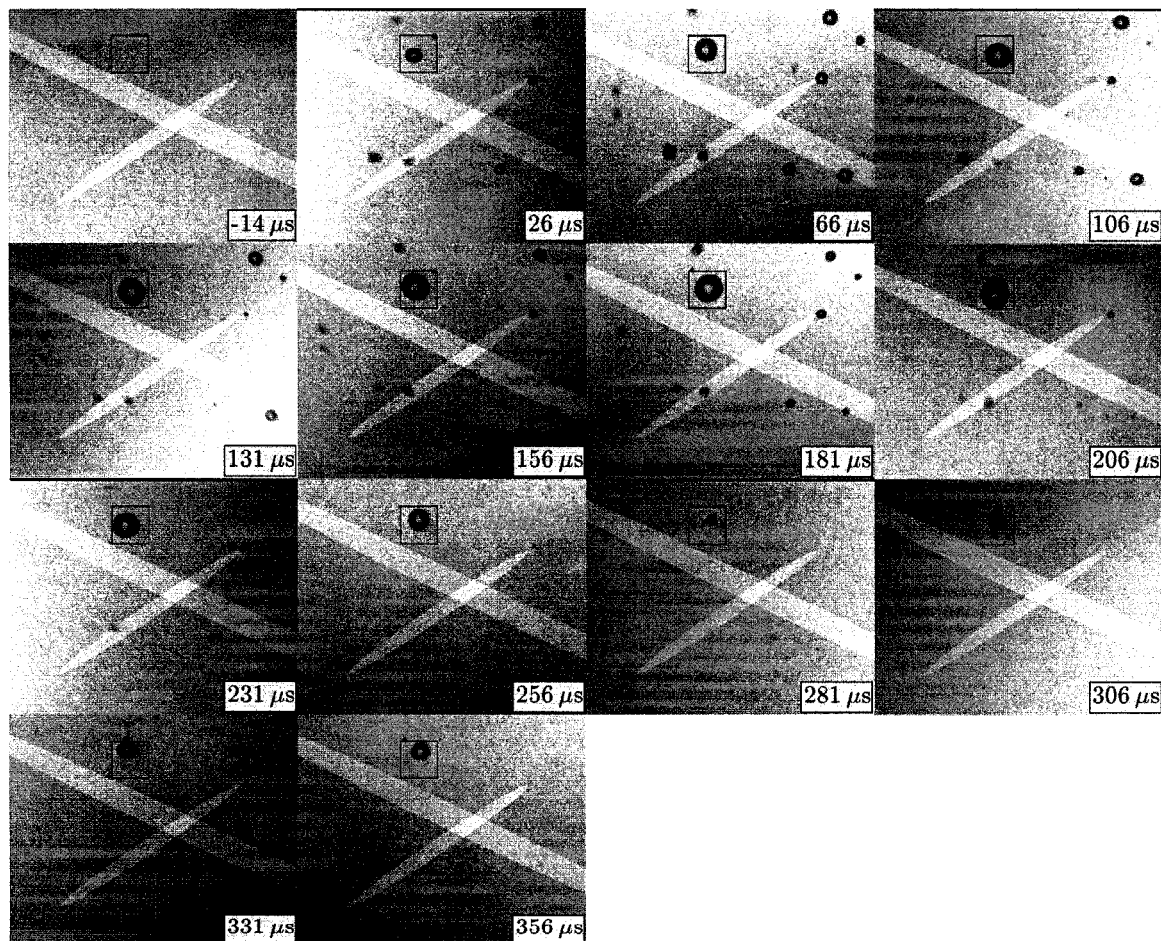
Figure 6.7. Sequential images of bubbles [reference: Case A, shot #26]. Each frame includes a time stamp, two highlighted regions, and a square box outlining a target bubble for analysis. In the referenced time scale, the shock wave arrived at the center of the field of view at time zero. The highlighted regions each correspond to the -6 dB sensitive region of a PCD. The box is 2.8 mm on all sides.

bounds of isolated lithotripsy bubbles. While a more careful discussion of the detailed test conditions is deferred to the next chapter, the compilation and analysis of acquired data are discussed in this section.

Before presenting a statistical analysis of the data, it is instructive to consider the selection of data used in the analysis. First, during data acquisition, not every shock wave (or 'shot') produced a cavitation field that was deemed worthy of study. Generally, these
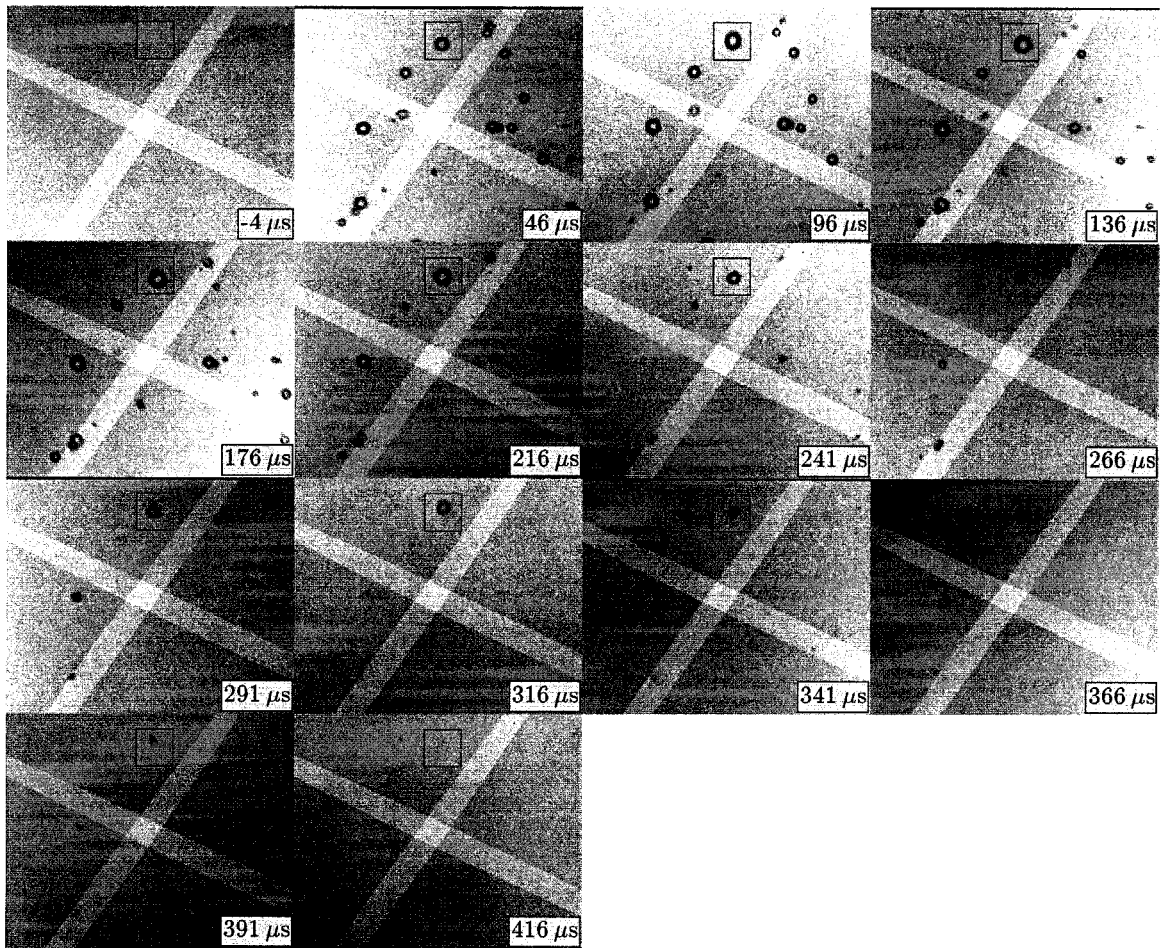
Figure 6.8. Sequential images of bubbles [reference: Case H, shot #44]. Each frame includes a time stamp, two highlighted regions, and a square box outlining a target bubble for analysis. In the referenced time scale, the shock wave arrived at the center of the field of view at time zero. The highlighted regions each correspond to the −6 dB sensitive region of a PCD. The box is 2.8 mm on all sides.

data involved either no observable bubbles or a cluster of interacting bubbles and were accordingly not saved. During refinement of the data collection procedures, on the order of 1,000 shots were saved and analyzed in at least a preliminary fashion. From data collected with the final test procedures across all nine test conditions from Table 5.2, 605 shots were saved for analysis. The image sequence from each saved shot was then graded as 'acceptable' or 'unacceptable' with regard to the presence of a bubble that could be studied as an isolated,

single bubble. Criteria for this grading included the overall density of bubbles in the field of view, the proximity of nearby bubbles, and the 'dominance' of the target bubble. Here, 'dominance' refers to not only the bubble size, but also to the collapse timing. Bubbles that collapsed later were judged to be more dominant because their rebounds would be less affected by motion of nearby bubbles. Of the 605 saved shots, 326 were graded to be acceptable for studying single bubbles.

In addition, during the data analysis, one further restriction was applied. Namely, each target bubble was required to begin its Rayleigh collapse at least 160 μs after shock-wave arrival at time zero. The utility of this restriction can be understood from the radius-time curves shown in Figure 6.4. In both of these curves, a point of inflection is apparent at a time in the 130–150 μs range. Although the shock wave ideally persisted for only about 15 μs, some tensile wave must have been present much later to explain the consistent point of inflection in the radius-time curves. While this behavior is discussed further in the next chapter, the implication for studying Rayleigh collapses is clear: for a bubble that began its collapse too early, the passage of a tensile wave likely interfered with the collapse. Indeed, this interpretation is borne out in that much higher variability was observed in the rebounds of early-collapsing bubbles. The time when a bubble began its collapse was recursively estimated from the radius-time curve in conjunction with the collapse time from PCD data. Of the 326 bubbles analyzed, 294 met this additional restriction and were included in the ensuing statistical analysis.

To present the data, we show in Figure 6.9 a scatter plot of the observed bubble rebounds for each of the nine test conditions. Note that in these plots, the rebounds are categorized by the observed symmetry of collapse. For asymmetric collapses, a bubble jet was observed in the photographs; conversely, a symmetric collapse was assumed when no jet was apparent. Although helpful, this categorization is imprecise given the spatial and temporal limitations of the high-speed photographs. Especially for the low-temperature conditions from Cases A–C, symmetry was repeatedly found to affect rebounds in an unexpected manner. Despite the conversion of energy into the asymmetry embodied by the jet, asymmetric rebounds were consistently larger than symmetric rebounds. It was initially postulated that the higher pressures inside a spherically collapsing bubble led to higher pressures radiated from

the bubble and therefore more acoustic damping of the rebounds. Such an assumption that acoustic radiation was the dominant damping mechanism is justified by measurements previously obtained by Vogel and Lauterborn[43,44] as well as by calculations performed by Johnsen et al.[47] The measurements acquired in this effort were used to motivate and guide Johnsen's calculations on Rayleigh collapses. Because symmetry could not be actively controlled or precisely observed, all data were kept to statistically represent the given test conditions. Table 6.1 summarizes the data from the scatter plots, including statistics for the symmetric collapses as well as for all collapses.

To go beyond the basic summary of the data described above, analysis of variance (ANOVA) was performed. To compare the rebounds flatly across all test conditions, the analysis was performed with both a one-way ANOVA as well as with a two-way analysis across groupings of both temperature and dissolved oxygen content. These analyses were performed using the 'anova1', 'anovan', and 'multcompare' functions within MATLAB (The MathWorks, Natick, MA). Results of these analyses are shown in Figures 6.10 and 6.11. For each test case in these plots, the mean of the rebound energy is denoted by a circle, while the vertical bars represent a 95% confidence interval. As such, the population means of any two cases are different at a 95% level of confidence if the corresponding vertical bars do not overlap. In Figure 6.10, it is clear from consideration of all data in part (a) that statistically significant differences occurred among many of the cases. Of particular note, Case A was different from all other cases; moreover, the degassed, room-temperature conditions represented by Case A are those most often used to experimentally study bubble dynamics. In part (b), the one-way ANOVA was applied only to data for which no jets were observed. These apparently symmetric rebounds are compared to model predictions with $a_m = 0.3$ in this plot. The relatively low number of 'symmetric' rebounds for some cases leads to the correspondingly large confidence intervals.

To more clearly discern the effects of temperature and dissolved gas content, two-way ANOVA results were explicitly compared against variations in either dissolved gas content or temperature. Given that Case I was troublesome as described in Section 5.5, the two-way ANOVA ignored this case. To avoid consideration of Case I, comparisons were made while omitting either the 60°C cases or the 85% dissolved oxygen cases. Results are provided in

94

Figure 6.11, where the plots can be interpreted as before. It is clear from these plots that both temperature and dissolved gas content contributed to the variance in the observed bubble rebounds. These comparisons were made at a 95% confidence level, while the p-values related to the significance of both temperature and dissolved gases are less than 10^{-3} for all combinations of cases analyzed.

6.3 Discussion of Results

In these experiments, careful control of test conditions in addition to normalization of the observed rebound data yielded conclusive results with regard to the influence of dissolved gases and temperature on vapor trapping behavior in lithotripsy bubbles. To the author's knowledge, these data represent the only experimental evidence to date that systematically characterizes vapor trapping across a range of test conditions. Although water conditions were tightly controlled in the experiments, other pertinent variables were not directly controlled. In particular, bubble asymmetries were frequently observed, while bubble collapse times (as measured by t_1) varied with a standard deviation of about 25 μs. Because longer collapse times enabled additional diffusion of non-condensable gases into the bubble, such variability tended to blur differences among the test conditions at 10%, 50%, and 85% dissolved oxygen. Model calculations suggest that these variations in t_1 roughly corresponded to changes in dissolved oxygen of up to 15% at high levels of dissolved gases and up to 5% at low levels. The higher sensitivity at higher levels of dissolved gases may contribute to the lack of any statistically significant difference between 50% and 85% levels, as indicated in Figure 6.11(a).

Overall, despite the presence of some uncontrollable variables, enough data were collected to statistically identify sensitivities to both temperature and dissolved gas content. This result is important because both temperature and gas saturation conditions are directly relevant to therapeutic ultrasound. In addition, these data provide several new insights. For example, the demonstrated sensitivity to dissolved gas content contradicts assertions made by Akhatov et al.[42] on the basis of their model for gas-vapor bubbles. In this work, Akhatov et al. explicitly argued that dissolved gas content should not affect the collapse dynamics of millimeter-sized bubbles. Consequently, they did not address the diffusion of
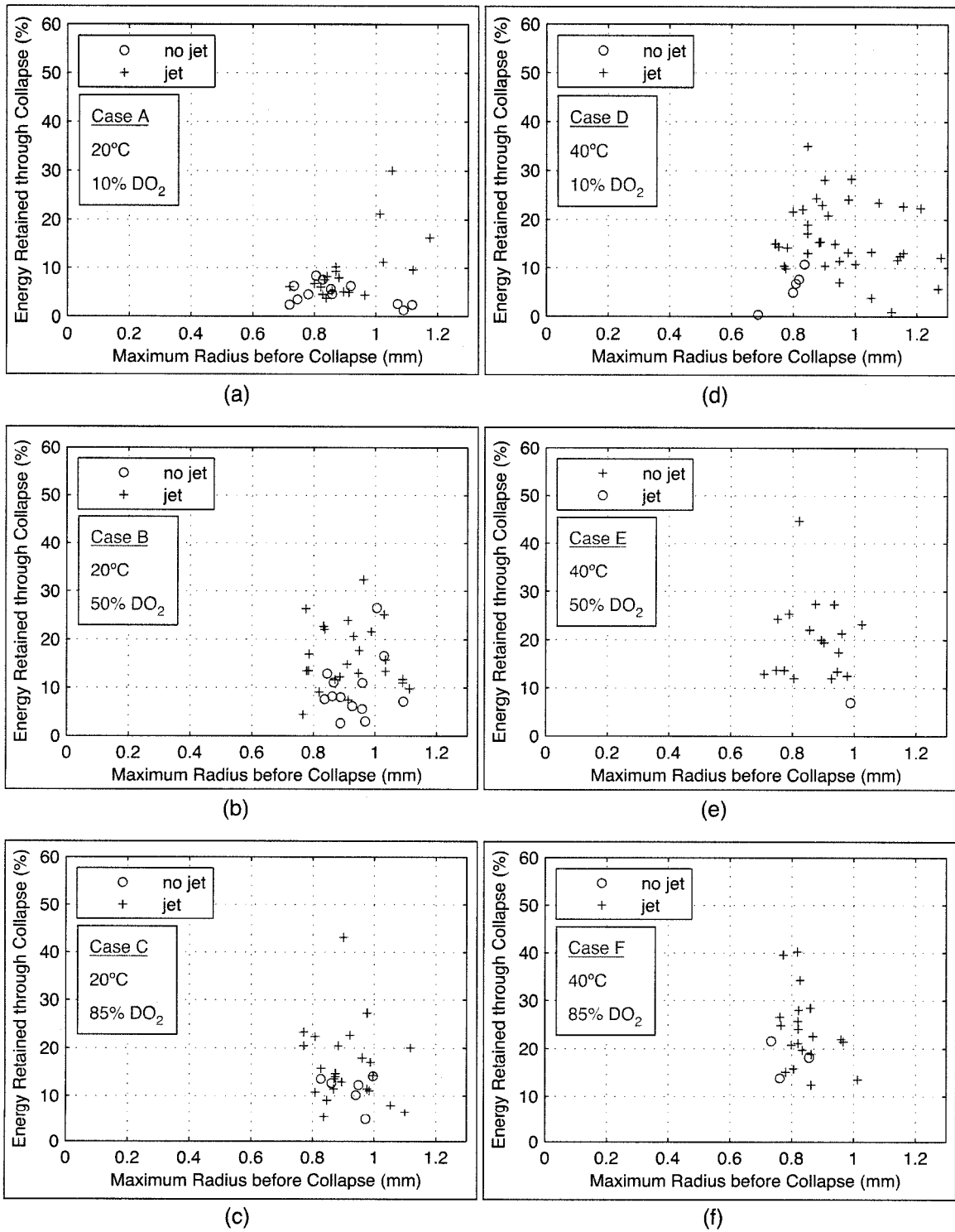
Figure 6.9. Scatter plots of bubble rebound data.

96
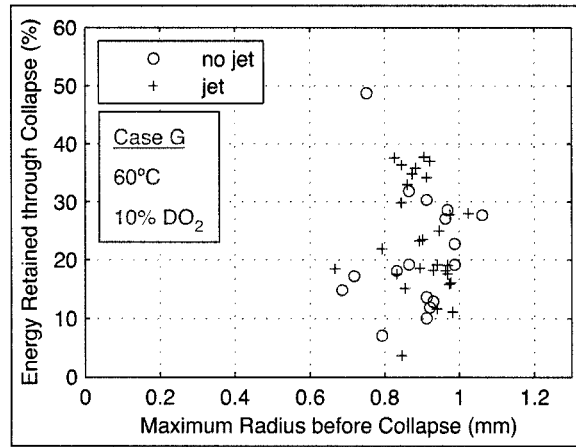
(g)
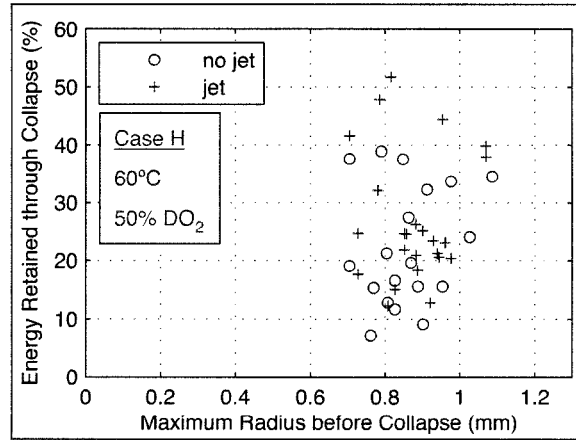
(h)
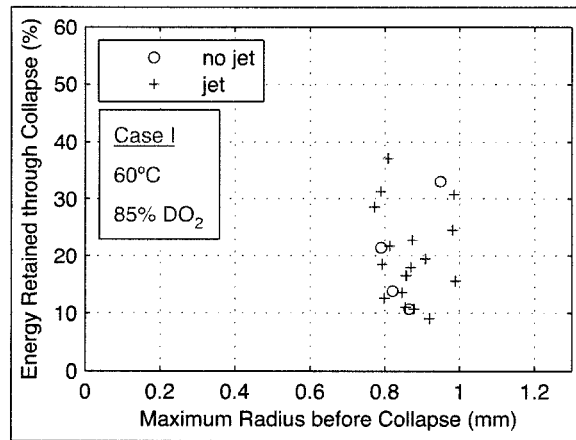
(i)

Figure 6.9. (figure continuation)
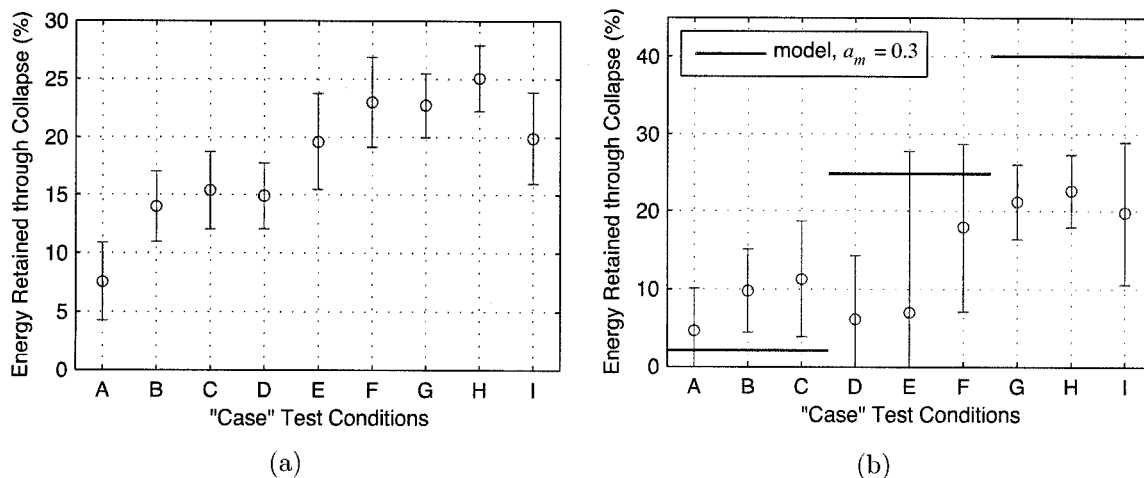
Figure 6.10. Comparison of one-way ANOVA results using (a) all data, and (b) only data for which no jet was observed. For each test case, the circle represents the sample mean while the vertical bar represents a 95% confidence interval. More specifically, any two cases whose vertical bars do not overlap can be described as having different means at a 95% confidence level. In (b), the horizontal blue lines indicate model predictions with boundary-layer scaling $a_m = 0.3$.
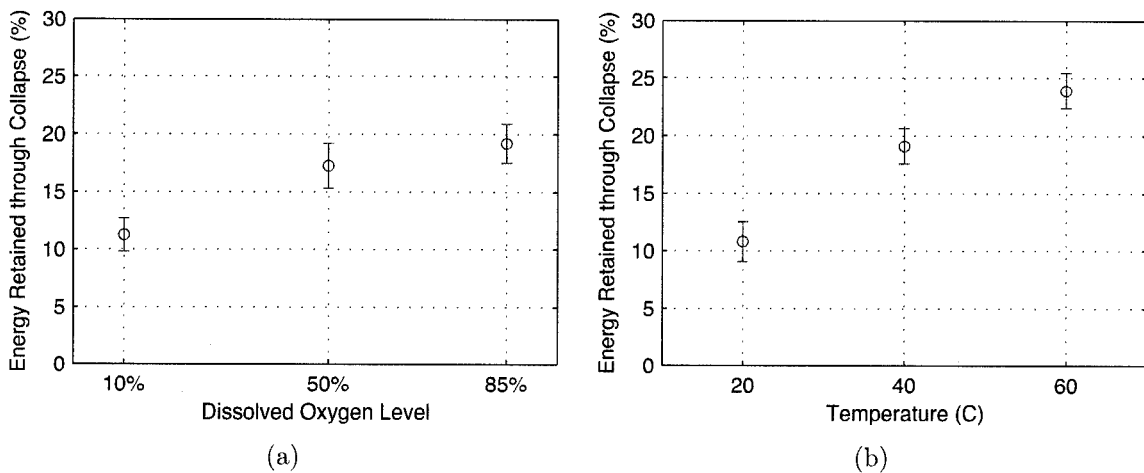
Figure 6.11. Comparison of two-way ANOVA results to isolate the effects of (a) dissolved oxygen level, and (b) temperature. In (a), Cases G, H, and I are omitted from the analysis, while Cases C, F, and I are omitted in (b). As above, for each test case, the circle represents the sample mean while the vertical bar represents a 95% confidence interval. Any two non-overlapping bars represent different means at the stated confidence level.

Table 6.1. Experimental observations of bubble rebounds.

	% Energy Retained through Collapse			
	Average (all) [# samples]	Average (no jet) [# samples]	Minimum (no jet)	Maximum (no jet)
Case A 20°C, 10% DO$_2$	7.6% [31]	4.7% [12]	1.3%	8.4%
Case B 20°C, 50% DO$_2$	14.0% [37]	9.8% [13]	2.6%	26.6%
Case C 20°C, 85% DO$_2$	15.4% [30]	11.3% [6]	4.8%	14.1%
Case D 40°C, 10% DO$_2$	14.9% [42]	6.1% [5]	0.4%	10.8%
Case E 40°C, 50% DO$_2$	19.6% [20]	7.0% [1]	7.0%	7.0%
Case F 40°C, 85% DO$_2$	23.0% [23]	18.0% [3]	13.9%	21.7%
Case G 60°C, 10% DO$_2$	22.8% [46]	21.2% [17]	7.1%	48.8%
Case H 60°C, 50% DO$_2$	25.1% [43]	22.6% [19]	7.2%	39.0%
Case I 60°C, 85% DO$_2$	19.9% [22]	19.8% [4]	10.7%	33.2%

non-condensable gases in their experiments with laser-induced bubbles. Aside from vapor trapping *per se*, an examination of the symmetric and asymmetric collapses in Figure 6.9 suggests that acoustic radiation ceases to be the dominant damping mechanism when bubble rebounds retain ~25% of the energy prior to collapse. Specifically, the 'jet' and 'no jet'

data points become fairly uniformly mixed for Cases G and H. With this observation, we can reasonably speculate that the energy dissipated from the excitation of non-volumetric oscillation modes is comparable in magnitude to the energy radiated acoustically from the bubble.

In addition to global evaluations of the experimental data, specific comparisons can also be made with model predictions. As described in Section 4.3, the collapses of lithotripsy bubbles are controlled by the mechanical rather than the thermal aspects of vapor transport. Accordingly, relevant model predictions involve the impact of the scaling parameter a_m on bubble rebounds. In the context of acquired experimental data, model predictions at 20°C, 40°C, and 60°C are plotted in Figure 6.10 for $a_m = 0.3$. As is evident in the figure, the model does not distinguish among levels of dissolved gases beyond the parameter a_m. The selection of $a_m = 0.3$ was based upon comparisons with prior data for spherical bubbles. Vogel and Lauterborn[43] found that 3.5 mm laser-induced bubbles retained only about of 17% of their energy after the initial collapse. In similar experiments, Akhatov et al.[42] found the normalized rebound energy to be about 2.4% for a spherical 1 mm bubble. Using equivalent conditions for the Rayleigh collapse of a bubble with an initial molar fraction of vapor of 0.999, the present model matches these data quite well with $a_m = 0.3$. It predicts normalized rebounds of 16% and 2.4% for 3.5 mm and 1 mm bubbles, respectively. Note that the cited experimental data involved test conditions that were not fully specified; apparently, degassed water at room temperature was used, thereby approximately representing the Case A test conditions from this effort.

In comparing model predictions with $a_m = 0.3$ to acquired test data at 20°C, good quantitative agreement occurs at a 10% dissolved oxygen level (Case A). The experimental data for symmetric rebounds under Case A conditions imply normalized rebound energies of 4.7% (see Table 6.1). Although this value is somewhat higher than the 2.4% reported by Akhatov et al.[42] for 1 mm bubbles, 2.4% remains well within the 95% confidence interval shown in Figure 6.10(b). Moreover, it is likely that many of the bubble rebounds in which no jet was observed did indeed possess some asymmetry. Hence, an average rebound slightly greater than 2.4% is consistent with the prior data in which symmetry was carefully controlled. Still considering data at 20°C, the ANOVA plots suggest that rebounds at higher levels of

dissolved gases for Cases B and C should lead to longer rebounds. Accordingly, because the model can simulate the impact of dissolved gas content only through the parameter a_m, the data from Cases B and C are best simulated with a_m ranging up to 0.55. Overall, the scaling model quantitatively captures the observed rebound data at 20°C, where vapor trapping behavior is modeled by scaling the diffusive boundary-layer thickness as the dissolved gas level changes. In addition, it is interesting to note that the lithotripsy bubbles observed in this effort seem to behave very similarly to the laser-induced bubbles studied previously.

From Figure 6.10(b), the model with $a_m = 0.3$ overpredicts the observed rebounds at 40°C and 60°C. Two explanations are suggested to explain this discrepancy: (1) acoustic radiation is no longer the predominant damping mechanism at higher temperatures, thereby implying that energy losses due to asymmetries decreased rebound amplitudes relative to the spherical model; and (2) the scaling approach used in the model does not effectively capture the rapid condensation rate required at higher temperatures (*i.e.*, very small values of a_m would be necessary to match the experimental data). In support of the first explanation, a spherical rebound with a rebound energy of 49% was observed for Case G. Such a rebound actually exceeds the model prediction at 60°C with $a_m = 0.3$. Moreover, while this data point is unique for Case G, a number of spherical rebounds between 30–40% were observed for Case H. Ultimately, both of the proposed explanations may contribute to the observed discrepancies between model predictions and experimental data at higher temperatures.

To summarize the range of rebounds predicted by the model for the conditions tested, Figure 6.12 depicts predicted rebound energies as a function of the parameter a_m. Separate curves are included for each test temperature, as sorted by color. Predictions were generated from simulated Rayleigh collapses for which the initial radius was either 0.7 mm or 1.2 mm to bracket the range of maximum radii observed experimentally. Lastly, the initial molar fraction of vapor inside the bubble was assumed to be 0.999 in order to be consistent with simulations of rectified diffusion for a millimeter-sized lithotripsy bubble. Although these calculations tend to be numerically unstable at very small scaling values ($a_m \lesssim 0.2$), it is clear from part (a) of the figure that each curve approaches an asymptote at large a_m. Moreover, the closeness of the asymptotes at 40°C and 60°C suggests that vapor trapping leads to maximum rebound energies of about 60–70%. By way of comparison, the largest

Table 6.2. Inferred values of the scaling parameter a_m from experimental data.

	Water Conditions	a_m
Case A	20°C, 10% DO_2	0.4
Case B	20°C, 50% DO_2	0.52
Case C	20°C, 85% DO_2	0.55
Case D	40°C, 10% DO_2	[< 0.2]
Case E	40°C, 50% DO_2	[< 0.2]
Case F	40°C, 85% DO_2	0.25
Case G	60°C, 10% DO_2	[< 0.2]
Case H	60°C, 50% DO_2	[< 0.2]
Case I	60°C, 85% DO_2	[< 0.2]

symmetric rebound observed experimentally was 49% (Case G). If the data are taken to be representative of the types of rebounds physically achievable, we can conclude that boundary layer thickness for lithotripsy bubbles should not be scaled by values of a_m larger than about 1. For convenience, the plot in part (b) provides an overlay of experimental results for the various test conditions for $a_m \leq 1$. The plotted experimental values represent the average values of symmetric rebounds for a given test case, as listed in Table 6.1. From this plot, the values of a_m listed in Table 6.2 can be inferred based on experimental observations. As discussed above, for temperatures above 20°C, it is unclear that the inference of values of a_m for spherical collapses is appropriate.
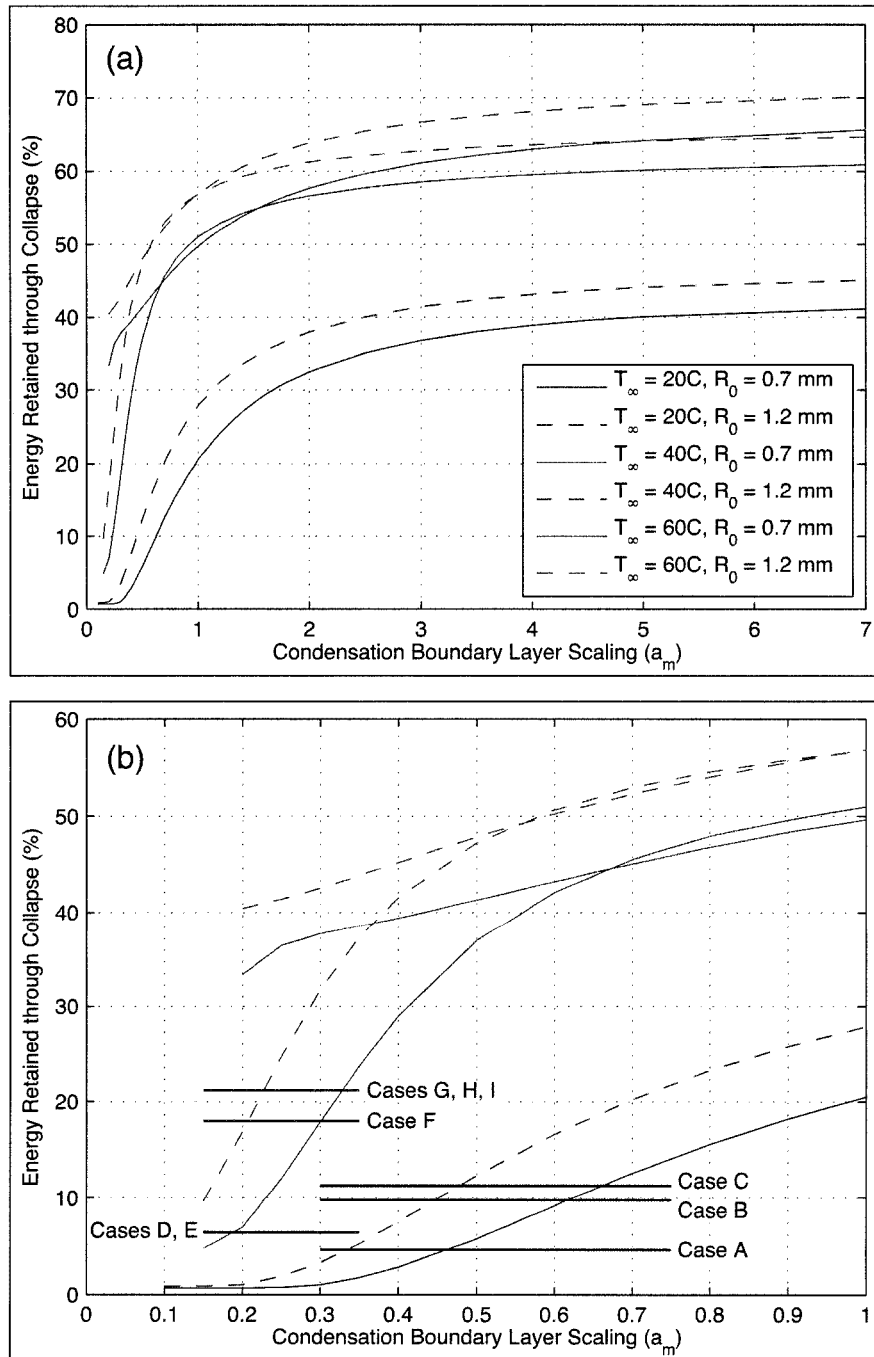
Figure 6.12. Model predictions of vapor trapping during a Rayleigh collapse. In (a), energy retained through collapse is plotted as a function of the scaling parameter a_m, while variation with temperature (T_∞) and initial radius (R_0) are also considered. In (b), experimental data are overlaid on top of these same model-prediction curves as thick horizontal lines. The plotted experimental data are an average of symmetric rebounds observed under given test conditions.

Chapter 7

TEST CONDITIONS FOR LITHOTRIPSY BUBBLES

In the experiments described in previous chapters, the number and location of cavitation nuclei were not explicitly controlled and some degree of randomness remained inevitable. However, significant efforts were undertaken to understand and control the sources of variability; ultimately, consistent data were collected. Below, these efforts are discussed in more detail. As guided by observations of the cavitation field, variations in test conditions were inferred from the characteristics of bubble growth and collapse (*i.e.*, $R_{max,1}$ and t_1 from Figure 5.1). First, maintaining very clean water was found to be necessary in order to avoid the excitation of dense clusters of bubbles rather than isolated bubbles. The water system described in Chapter 5 was instrumental in preparation of the water. Aside from the water itself, variabilities in shock-wave generation and propagation were also identified.

In the first two sections below, direct observations pertinent to the generation and reflection of the focal shock wave are discussed. Subsequent sections are devoted to consideration of the observed growth and collapse characteristics of bubbles. For context, the collapse time (*i.e.*, t_1 from Figure 5.1) of SWL bubbles has been associated with the clinically relevant issue of shock-wave delivery rate;[10] however, experimentally observed times have exceeded those predicted analytically.[51,81] Attempted explanations of the experimental observations have included multi-bubble interactions and possible inaccuracies in measuring of the tensile portion of shock waves; both of these issues are addressed below. In addition, an alternate explanation for the longer collapse times is proposed in terms of secondary acoustic waves radiated from the ellipsoidal reflector.

7.1 Shock-Wave Variability

Given that an electrohydraulic lithotripter was used in this work, significant shot-to-shot variability was expected. The variability is caused by the stochastic nature of a high-voltage

breakdown between electrodes and the corresponding impact on the generated acoustic wave. However, an additional trend was noted from observations of the cavitation field. Although a weaker acoustic wave should be expected with newer and more closely spaced electrodes, a qualitative change in the cavitation field was noted as electrodes aged. Brand new electrodes produced smaller regions of cavitation and fewer bubbles. As dozens of shots were fired, this qualitative behavior could be maintained by reducing the charging voltage of the lithotripter to account for the generation of stronger acoustic waves. However, as electrodes aged to approach about 200 shots, the cavitation field typically began to change as more bubbles were excited. Upon inspection of such electrodes, it was apparent that the electrical discharge path did not occur consistently between the tips of the electrodes. As electrodes became worn, the discharge path may have become less consistent, thereby altering the assumed geometry in which the shock wave is initiated at a focus of the ellipsoidal reflector. It is speculated here that geometric effects associated with the location of the 'spark' between electrodes may account for the observed changes in the cavitation field.

To better understand shock-wave variability, the focal acoustic field was explicitly measured and characterized with regard to both the geometry of the ellipsoidal reflector as well as the state of the electrodes. More specifically, beamwidths of individual shock waves were measured using a prototype hydrophone array. This work has been written in a manuscript recently submitted to the *Journal of the Acoustical Society of America* and is included here in Appendix B. While signficant shot-to-shot variability was observed in these measurements, it remains difficult to interpret them in terms of the qualitative descriptions of the cavitation field given above. However, with regard to reflector geometry, it was found that a more highly focused ellipsoidal reflector did indeed produce a narrower focal beamwidth; however, the observed cavitation behavior (perhaps associated with secondary waves as discussed in Section 7.4) precluded this reflector from being especially useful in the study of Rayleigh collapses.

7.2 Surface Reflections

In the previous section, variability of the focused shock wave is discussed. However, in addition to the primary focal wave, a reflection of this wave from the surface of the water

surface in the test tank was observed to affect bubbles. The presence of this reflection was first identified by the appearance of a 'ringing' on the signal of the PCD that was connected to the analog high-pass filter. It is speculated that this ringing represents a type of impulsive filter response that is induced by the impingement of a reflected wave on the PCD. Regardless of the characterization of the ringing signal, its timing was predictably changed with the water level. Moreover, high-speed photographs indicate the presence of such a reflected wave in that gas bodies that had disappeared after passage of the primary focal wave are re-excited.

This effect is depicted in Figure 7.1; the timing suggests that the focal wave was scattered at the geometric focus of the lithotripter and that this scattered wave traveled to the water surface and back. As observed by both the filter 'ringing' and the photographs, this reflection occurred repeatably and was not fully absorbed or re-directed by the placement of an angled metal or plastic plate beneath the water's surface. The plates used for re-direction were roughly the same size as the opening of the HM3-style reflector. Ultimately, this reflection was addressed by building a taller tank and raising the water level to delay arrival of the reflected wave until well after the bubble rebound had occurred. However, it is worthwhile to note that typical lithotripter tanks are much smaller and likely exhibit similar reflections.

7.3   Modeling Bubble Collapse Times in a Cluster

To aid interpretation of experimentally observed bubble collapse times, multi-bubble interactions were simulated using two recently published models. One model takes an 'averaged medium' approach and assumes a uniform bubble cluster.[86] The other explicitly simulates the dynamics of all bubbles in a finite cluster.[87] Because liquid compressibility does not strongly affect collapse times, incompressible versions of both models were implemented. Before describing each model, it is instructive to recall the basic, incompressible Rayleigh-Plesset equation (2.25), which is repeated below for convenience:

$$R\ddot{R} + \frac{3}{2}\dot{R}^2 = \frac{1}{\rho_0}\left(p_w - p_\infty\right)$$
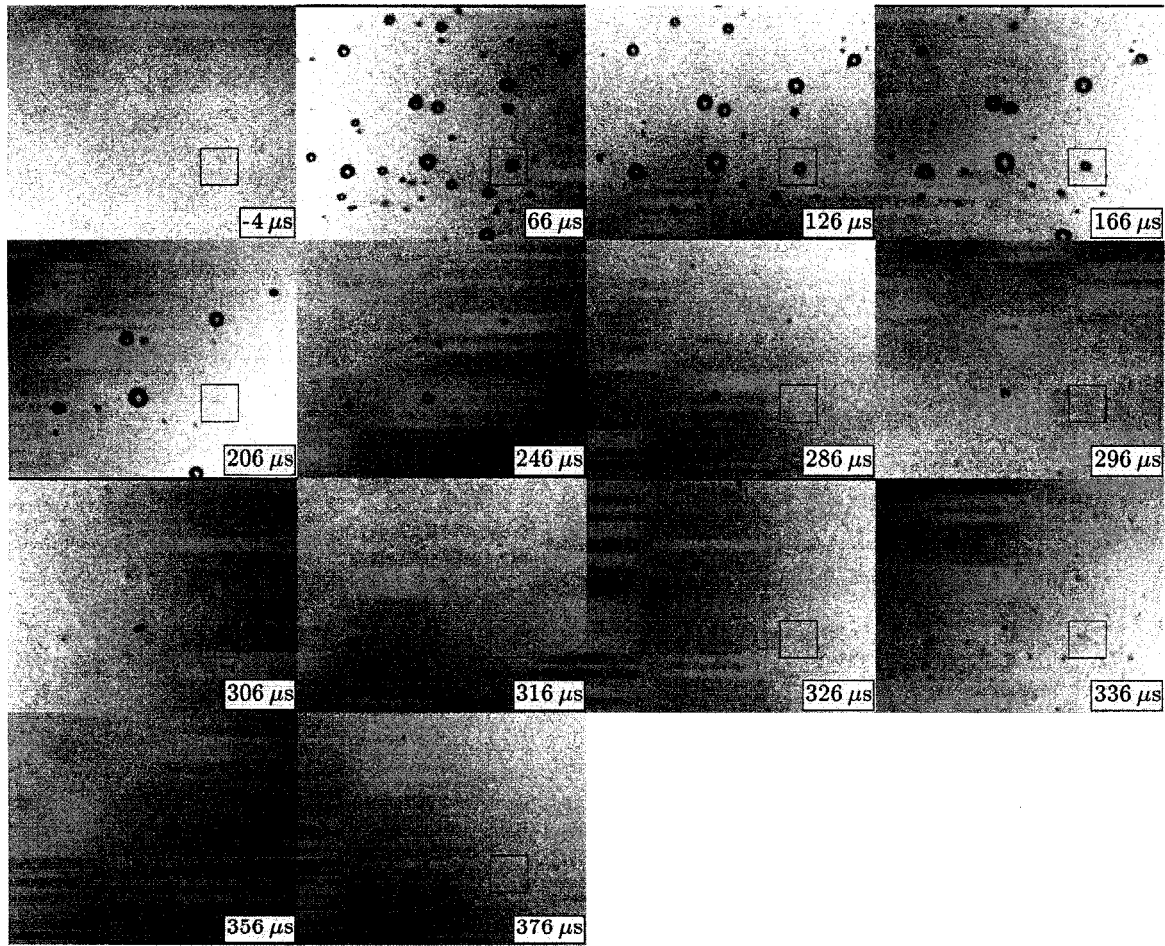
Figure 7.1. Sequential images of bubbles to demonstrate surface-reflection effects. In the referenced time scale, the focal shock wave arrived at the center of the field of view at time zero, while the direct wave arrived 37 μs earlier. The water level in the tank was measured to be vertically 248 mm above the center of the field of view. Given water at 20°C with a sound speed of 1,482 m/s, reflection of the direct wave from the water's surface arrived back in the field of view at ~298 μs; moreover, surface reflection of the focused wave arrived at ~335 μs. Visible excitation of bubble remnants suggests a nontrivial effect from the reflection of the focused wave.

Above, p_w and p_∞ are again defined from Equations (2.23) and (2.29). This basic relation for a single bubble is adapted for the cluster models discussed below. For simplicity, the radial dynamics of each bubble are closed by using a polytropic expression for the pressure inside the bubble:

$$p_i = p_{i0} \left(\frac{R_0}{R}\right)^{3\gamma} \tag{7.1}$$

Above, p_{i0} is the initial pressure inside the bubble, R_0 is the initial bubble radius, and γ is the ratio of specific heats. Considering an adiabatic approximation for air inside the bubble, we use $\gamma = 1.4$. Although this polytropic approximation is not well suited for violent collapse phenomena, it predicts essentially the same collapse time for a single bubble as the model presented in Chapter 2. Accordingly, the single-bubble model described by the previous two equations is a suitable starting point for modeling bubble clusters in the context of collapse times.

Arora et al.[86] have derived a modified form of the two-degree-of-freedom Rayleigh-Plesset equation. In their approach, all bubbles within a uniform cluster behave identically and the radial dynamics are represented as follows:

$$\left(1 + 2\pi R \mathcal{N}^{1/3}\right) R\ddot{R} + \left(3/2 + 4\pi R \mathcal{N}^{1/3}\right) \dot{R}^2 = \frac{p_w - p_\infty}{\rho_0} \tag{7.2}$$

Here, $\mathcal{N}$ represents the uniform number density of bubbles; hence, nearby bubbles contribute terms proportional to both $R\ddot{R}$ and $\dot{R}^2$. Given this formulation, all bubble interactions occur instantaneously inasmuch as liquid incompressibility implies an infinite sound speed. In addition, it should be noted that the derivation of this model includes the assumption that bubbles only interact with one another over distances less than the average bubble-to-bubble spacing. First, this assumption is necessary on boundedness considerations. Assuming a calculation of the radial dynamics of a bubble at the origin of a spherical coordinate system, the influence of any single neighboring bubble will decline as $1/r$ in terms of the radial distance r to the neighbor bubble. However, because the number of bubbles in a homogeneous cluster will increase with the cluster volume and r^3, the cumulative influence of all bubbles in an infinite cluster is not bounded. Since the radial dynamics should clearly remain bounded, imposition of a finite bubble interaction distance is necessary. Moreover, as discussed by Arora et al.,[86] ignoring distant bubbles in the model can be justified physically by considering finite acoustic propagation delays as well as shielding effects of intervening bubbles.

In a different approach, Hamilton et al.[87] represented each bubble in a cluster with its own two-degree-of-freedom equation. For the ith bubble in the cluster, the governing

equation can be written as

$$R_i\ddot{R}_i + \frac{3}{2}\dot{R}_i^2 + \sum_{j\neq i} \frac{R_j}{d_{ij}}\left(R_j\ddot{R}_j + 2\dot{R}_j^2\right) = \frac{p_w - p_\infty}{\rho_0} \tag{7.3}$$

where d_{ij} is the distance between the ith and j^{th} bubbles in the cluster. Using this approach, a cluster comprising N bubbles in any geometry can be simulated by simultaneously solving N of the above equations. Even using the assumption of liquid incompressibility and instantaneous bubble interactions, implementation of such a model becomes computationally challenging for more than 10–20 bubbles. However, the computational limits of this approach are balanced by the arguments described above for limiting the bubble interaction distance and the number of relevant 'neighboring' bubbles.

To understand the impact of multi-bubble interactions on the collapse times of lithotripsy bubbles, both of the above models were used to calculate the response of bubble clusters excited by an analytic shock wave. For the former model, the simulations were executed by assuming initial bubble radii of 3 μm and specifying a number density $\mathcal{N}$. For the latter model, 3 μm bubbles were assumed to populate a 3×3×3 Cartesian grid (27 total bubbles). The initial radii of the bubbles were chosen to be constant at 3 μm, though the results were not sensitive for initial radii up to about 10 μm. Moreover, it is very likely that cavitation nuclei were no larger than 3 μm in the experimental work given the absolute filtration of particulates above 2 μm. The spacing between bubbles in the grid was then determined by the specified number density $\mathcal{N}$. In this case, the relevant collapse time was taken to be that of the bubble at the center of the grid. Assuming simultaneous excitation of all bubbles by an analytic shock wave [see Equation (4.2), $A = 25$ MPa, $\alpha = 6.5 \times 10^5$ rad/s, and $f = 100$ kHz], radius-time curves were calculated using both models with varying bubble densities.

As shown in Figure 7.2, both models demonstrate that higher bubble densities lead to longer collapse times. Simulations suggest that even low bubble densities of 1/cm^3 can affect the collapse time by a notable amount relative to that of an isolated bubble. In comparing the models, a qualitative difference is apparent. While the uniform medium involves symmetric bubble growth and collapse, 'edge' effects for the explicit cluster introduce an

asymmetry between growth and collapse phases. Moreover, this asymmetry becomes more prominent for higher densities at which the cluster boundaries are closer to the center bubble. In addition to the asymmetry that begins during bubble growth, early collapses by bubbles at the periphery of the cluster emit large compressive waves that accelerate the collapse of the center bubble. Because the explicit cluster model does not accurately simulate bubble collapses or the propagation of shock waves emitted during collapse, some artifacts associated with nearby collapses are unavoidable.

Although higher bubble densities do increase collapse times, quantitative evaluation of model predictions implies that bubble interactions alone do not account for the longer collapse times observed experimentally. From the data presented in Chapter 6 at a temperature of 20°C, bubbles achieving a maximum radius of about 0.8 mm consistently collapsed about 250 μs after shock-wave arrival. Although model simulations do not account for vapor pressure, these data at 20°C should closely represent the conditions simulated in the calculations from Figure 7.2. From the cavitaton fields photographed experimentally (see Figures 6.2, 6.3, 6.7, 6.8), it is typical to observe on the order of 5 'significant' bubbles in the field of view. Because not all bubbles are the same size, 'significant' bubbles are assumed to be similar in size to the target bubble. Considering that the optical depth of field in the photographs is larger than the transverse width of the lithotripter's focal region, it's reasonable to estimate the viewed cavitation volume as height of the field of view times the transverse width squared. Assuming a transverse width consistent with the −6-dB focal region of the tensile portion of the shock wave,[82] the viewed cavitation volume is roughly $1.9 \times 1.5^2 = 4.3$ cm³. Consequently, observation of 5 'significant' bubbles in the photographs is comparable to a bubble density of $5/4.3 \approx 1/\text{cm}^3$. At this low of a bubble density, the uniform medium model predicts a collapse time less than 200 μs. At 1 bubble per cm³, the explicit cluster model predicts a collapse time near the observed 250 μs, especially when considering that the collapse time is accelerated by nearby collapses. However, this model includes 27 'significant' bubbles with a grid spacing of 1 cm along each axis—a photograph of comparable conditions would likely include at least 12 such bubbles. Ultimately, the discrepancies in simulated collapse times between models highlight the different assumptions used regarding the maximum bubble interaction distance. In light of these differences,

(a) uniform bubbly medium

(b) explicit 3×3×3 cluster
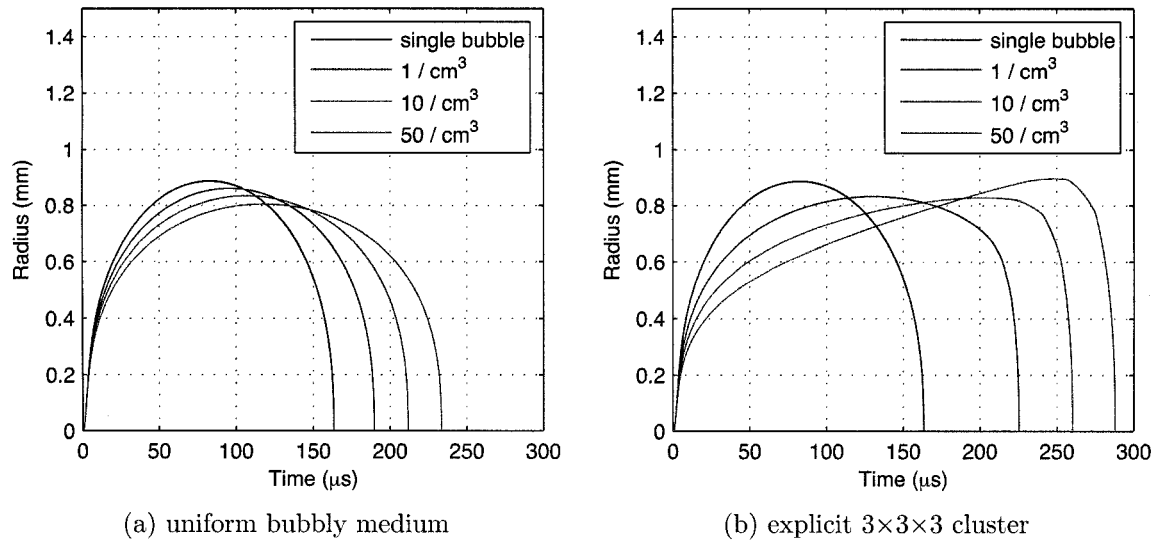
Figure 7.2. Growth and collapse of bubbles exposed to a lithotripter shock wave. Simulation results for (a) a bubble within a uniform, 'averaged' bubbly medium, and (b) a bubble at the center of a 3×3×3 cluster of 27 bubbles. Typical cavitation fields such as those depicted in Figures 6.2 and 6.3 correspond to densities on the order of $1/cm^3$.

it seems likely that the uniform-medium simulation at $1/cm^3$ is a better representation of experimental test conditions.

Despite some ambiguities in interpreting simulated collapse times, the longer times observed experimentally do not appear to be caused solely by multi-bubble interactions. In addition to collapse times *per se*, the shape of the radius-time curves is also telling. Experimental observations consistently exhibited the presence of an asymmetry (see Figure 6.4); however, neither bubble-cluster model predicts similar asymmetries at bubble densities near $1/cm^3$. While bubble interactions likely did play a role in increasing bubble collapse times, an alternate hypothesis provides a credible explanation for the observed radial dynamics. As discussed further in the next section, secondary pressure waves radiated from the ellipsoidal reflector may have affected the dynamics of bubbles initially excited by the primary focal shock wave.

7.4 Secondary Waves

As mentioned above, the characteristic shape and collapse times of experimentally observed radius-time curves imply that secondary acoustic waves not attributable to other bubbles were present. To further elucidate this point of view, the radial dynamics of an isolated bubble are illustrated in Figures 7.3 and 7.4. From the high-speed photographs, only a single 'significant' bubble was visible. Although a second small bubble appeared in early frames, the oversized amplitude of this bubble's rebound suggests that its dynamics were dominated by the target bubble. Because the isolated target bubble still possessed an asymmetry in its growth and collapse phases, it is reasonable to infer the presence of a secondary excitation.

The asymmetry evident in Figure 7.4 appears to represent an inflection point in the radial dynamics. As discussed in Appendix B, this behavior was exaggerated when a more highly focused ellipsoidal reflector was used (see Figure B.6). This link to the ellipsoidal reflector in conjunction with recent modeling work by Sapozhnikov et al.[88] strongly suggests that reverberations inside an HM3-style ellipsoidal reflector play a role in the observed bubble dynamics. Although not previously considered, such waves may be relevant to studies that either try to quantify the cavitation potential of a lithotripter[89] or to control cavitation effects with multiple acoustic pulses.[90]

7.5 Impact of Bubbles on Shock-Wave Measurements

In trying to match analytically predicted bubble collapse times with experimental data, a final aspect involves hydrophone measurements of the tensile component of lithotripter shock waves. Because this tensile component drives the subsequent bubble growth and collapse, accurate measurement of the energy in this portion of the shock wave is critical. In previous work, such hydrophone measurements have been speculated to be inaccurate as a means of explaining experimental collapse times.[81] In related work, researchers have attempted to characterize how the tensile component of a shock-wave is attenuated as it propagates through a bubbly medium.[14,91,92] While these efforts have used models and/or hydrophone measurements to evaluate attenuation of the traveling shock wave, the impact on hydrophone measurements of nearby bubbles has not been explored.
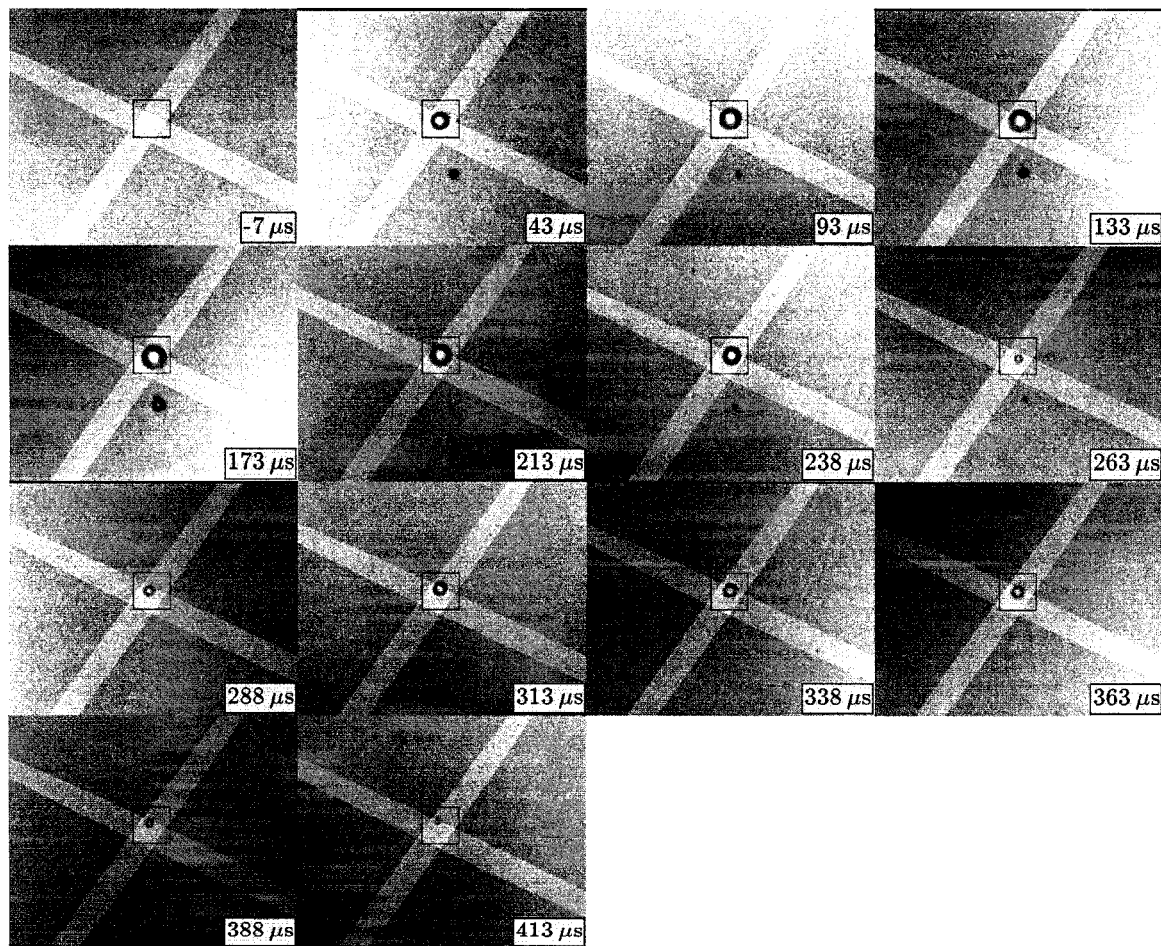
Figure 7.3. Sequential images of bubbles [reference: Case G, shot #60]. Each frame includes a time stamp, two highlighted regions, and a square box outlining a target bubble for analysis. In the referenced time scale, the shock wave arrives at the center of the field of view at time zero. The highlighted regions each correspond to the −6 dB sensitive region of a PCD. The target bubble is almost completely isolated. Although a second bubble is visible in the early frames, it is clear that this bubble was very small and primarily excited by pressures radiated from the much bigger target bubble.

To better understand hydrophone measurements of shock waves that induce cavitation, the simple Rayleigh-Plesset models from Section 7.3 for a single bubble as well as for a bubble cluster were utilized. First, assuming an incompressible liquid, the pressure radiated by a
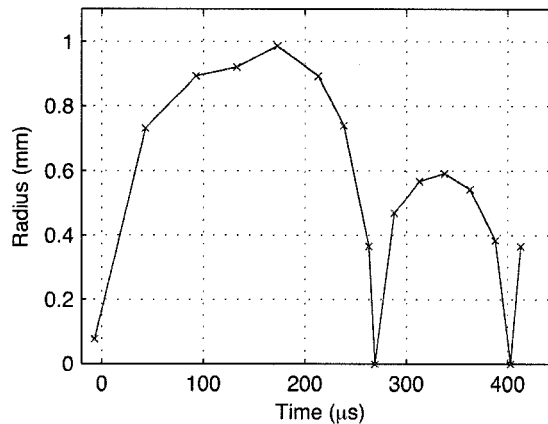
Figure 7.4. Radius-time curve derived from image sequences of a bubble from Case G conditions [reference shot #60]. Each red 'x' indicates a measurement from a single frame while the blue lines connect measurements. Note that measurements from image frames are supplemented by the PCD data—at measured collapse times, a radius of zero is assumed and plotted. Asymmetry associated with a point of inflection near the frame at 173 μs implies the presence of secondary acoustic waves that alter the radial dynamics.

single bubble can be expressed as[69]

$$p_{rad}(r,t) = \rho_0 \left[\frac{R}{r} \left(\ddot{R} + 2\dot{R}^2 \right) - \frac{R^4}{r^4} \left(\frac{\dot{R}^2}{2} \right) \right] \tag{7.4}$$

where t is time and r is the radial coordinate with the origin at the bubble's center. For a single 3 μm bubble excited by an analytic shock wave, the radiated (or 'scattered') pressure from the bubble was calculated as shown in Figure 7.6(a). The simulated shock wave approximates the tensile wave from a Doli-50 lithotripter[93] by using Equation (4.2) with $A = 6$ MPa, $\alpha = 3 \times 10^5$ rad/s, and $f = 90$ kHz. Although the radiated pressures calculated from Equation (7.4) inherently assume incompressibility, the plotted pressures at the indicated radial locations include an acoustic delay estimated from the linear sound speed in water. Considering these radiated pressures, algebraic superposition of the incident shock wave and the scattered wave yields the plots in Figure 7.6(b). Assuming that the incident shock wave arrives simultaneously at both the bubble and measurement locations either 1 mm or 5 mm away, these curves approximate the shock wave as it would be measured in the vicinity of

a single bubble. Notably, even a single nearby bubble can measurably attenuate the tensile portion of the measurement. In addition, we note that at 5 mm away, the acoustic delay of the scattered wave is large enough that its compressive phase reinforces the compressive 'ringing' that follows the tensile part of the incident shock wave. Both of these qualitative effects have been observed for hydrophone measurements in bubbly media,[92-94] though they have been attributed to shock-wave attenuation during propagation through bubbles.

The insight gained above from a single bubble suggests that bubbles can locally affect hydrophone measurements of a lithotripter shock wave independent of propagation effects. However, to go a step further, the multi-bubble models from Section 7.3 were also considered. First, for a uniform medium as modeled by Equation (7.2), the effects of bubble interactions can be qualitatively evaluated. As illustrated in Figure 7.6, stronger interactions at higher bubble densities lead to two competing effects. The scattered pressure of any individual bubble is less at higher densities, as can be inferred from the mutual inhibition of radial growth for closely spaced bubbles. However, the reduced scattering of each bubble is offset by the presence of more bubbles when densities are higher. To address these competing effects, the explicit cluster model defined by Equation (7.3) was used to study a $2 \times 2 \times 2$ grid of bubbles as depicted in Figure 7.7(a). Using the approach from Figure 7.6(b), a hydrophone measurement at the center of the 8-bubble grid was estimated by superposition of the incident shock wave and the pressures radiated from each of the bubbles. Again, the shock wave was assumed to simultaneously excite all bubbles while propagation delays of the scattered pressures were accounted for in the superposition of pressures at the center of the grid. Results of these calculations at various densities are presented in Figure 7.7(b). From these simulations, higher bubble densities indeed reduce the tensile portion of the measured wave, while densities as low as $10/cm^3$ produce noticeable effects. Note that the 'spikes' on the blue, red, and green curves correspond to the initial bubble collapses induced by the leading compressive phase of the incident shock wave.

In prior studies of the effects of bubbles on the attenuation of tensile component of lithotripter shock waves, bubble densities from a few bubbles per cm^3 to thousands per cm^3 have been considered.[91-94] Each of these prior studies noted the attenuative effects of bubbles on the energy in tensile part of the shock wave. However, to the extent that
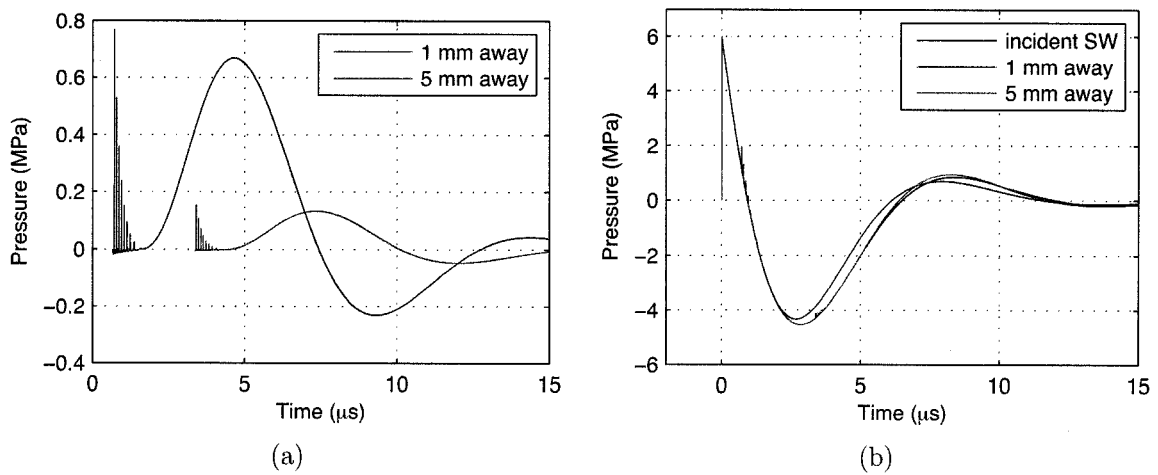
Figure 7.5. Scattering from a single bubble excited by an analytic shock wave that simulates the output of a Doli-50 lithotripter.[93] Part (a) shows pressures radiated by a single bubble at nearby distances, while part (b) shows algebraic superposition of the radiated pressures with the incident shock wave.

mechanisms were discussed, the attenuation was associated with propagation through a bubbly medium. In this section, a mechanism has been identified through which bubbles can locally affect hydrophone measurements without attenuating the energy actually maintained in the tensile component of the shock wave. As such, care should be exercised in interpreting hydrophone measurements of lithotripter shock waves when bubbles may be present. Ideally, standard procedures used to characterize the acoustics of clinical lithotripters should include measures for controlling and/or observing cavitation during the measurement. While the curves plotted in Figure 7.7 provide an estimate of the magnitude of the local effects of bubbles on hydrophone measurements, these results are clearly dependent on the exact geometry of the bubbles. Moreover, effects including acoustic propagation delays among interacting bubbles, spatial and temporal variation of the incident shock wave, and liquid compressibility in the formulation of the radial bubble dynamics have not been considered. A model including a more detailed accounting of bubble interactions is currently under development by collaborators at the University of Texas at Austin. Overall, this work has led to ongoing collaborations with researchers at the University of Texas at Austin and Indiana University–Purdue University Indianapolis.[93,95]
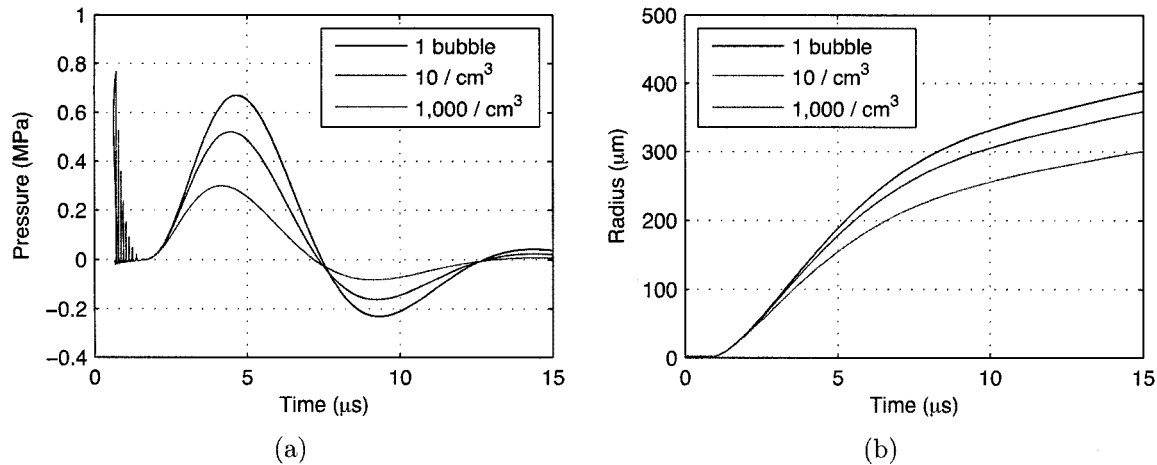
Figure 7.6. Scattering from a single bubble within a uniform bubble cluster. (a) Pressures radiated 1 mm away from a single bubble within a uniform cluster of various densities, and (b) radius-time curves depicting how the interaction with surrounding bubbles inhibits bubble growth. The plots illustrate competing effects whereby higher bubble densities imply both the superposition of radiated pressures from more bubbles as well as a diminished contribution from each bubble.
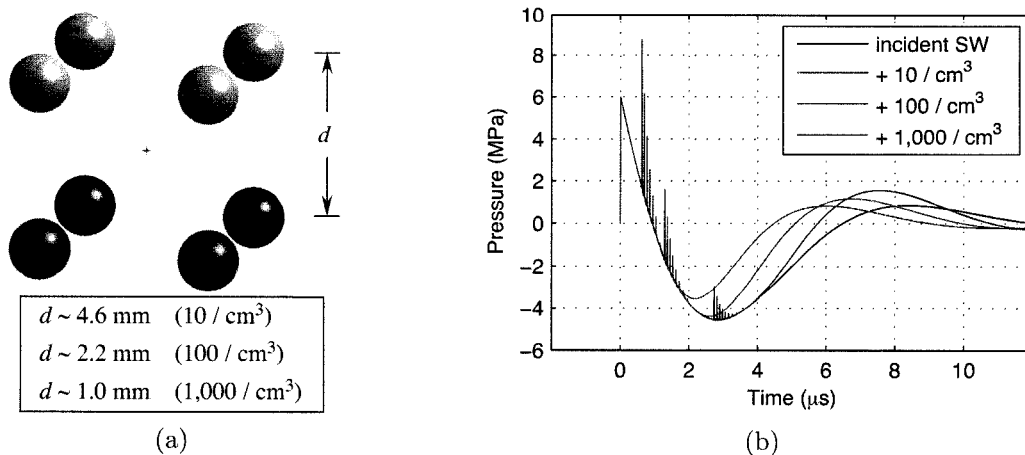
Figure 7.7. Effects of bubble clusters on shock-wave measurements. In (a), the simulated grid of 8 bubbles is depicted along with the assumed measurement location in the center of the grid. Accounting for local scattering within the cluster, calculated pressure measurements of the incident shock wave at the center of the cluster are plotted in (b).

Chapter 8

CONCLUSIONS

8.1 Summary

The overarching goal of this effort was to advance the paradigm that vapor plays an important role in the bubble dynamics associated with therapeutic ultrasound. Here, therapeutic ultrasound is used to describe both high-intensity focused ultrasound (HIFU) and shock-wave lithotripsy (SWL). Both a numerical model as well as experiments were used to elucidate the influence of vapor.

The motivation for studying vapor in HIFU is self-evident: as acoustic energy heats tissue, boiling can and does occur in some treatments. As such, bubbles excited under temperatures at or near boiling will involve vapor. However, due to the difficulty of modeling vapor transport behaviors, previous modeling related to HIFU has either ignored vapor[19] or analyzed only low-amplitude acoustic excitations.[26,32] For SWL, vapor has been implicated in the dynamics of bubble collapse and has been treated with a reduced-order model.[36] However, this previous work did not characterize the influence of vapor beyond the presence of an arbitrary scaling parameter. Given this context, the present effort has aimed to provide a framework for addressing gas-vapor bubble dynamics under the thermodynamic conditions characteristic of therapeutic ultrasound.

Using a model based on scaling principles, the effects of vapor and vapor transport on inertially collapsing bubbles were categorized as thermal and mechanical. In the model, thermal effects are identified through scaling parameters for heat conduction in the gas and the liquid, while mechanical effects are identified with a scaling parameter for mass diffusion among vapor and gas molecules. The thermal effects of vapor were not studied in detail in this work; rather, related calculations were used to tune the associated scaling parameters. From there, model predictions were used to conclude that Rayleigh collapses of millimeter-sized bubbles are primarily sensitive to the mechanical effects of vapor transport. With this

determination, experiments to test this aspect of the model were designed and executed.

Experiments involved observation of the collapse and rebound of individual lithotripsy bubbles. By varying liquid conditions with regard to temperature and dissolved gas content, the experiments were designed to alter gas-vapor diffusion during collapse, thereby elucidating the associated vapor-trapping behavior. The acquired data statistically confirmed that both dissolved gas content and temperature affected bubble rebounds. In itself, this result is meaningful in that it demonstrates a higher sensitivity to dissolved gases than previously thought.[42] Moreover, these data represent the first data collected to systematically understand vapor trapping under various liquid conditions. Another significant result of the experiments concerns the impact of bubble symmetry on the energy retained in volumetric bubble oscillation. Especially in cold and degassed water, asymmetric collapses were found to produce much larger rebounds despite the energy consumed by formation of a re-entrant jet. This phenomenon can be explained by noting that the energy retained through such a collapse is primarily controlled by the damping associated with acoustic radiation. Because asymmetric collapses generate lower pressures and temperatures inside a bubble,[96] the accompanying acoustic radiation is limited and the bubble retains more energy. However, at higher temperatures and/or levels of dissolved gas content, the correlation of asymmetric collapses and larger rebounds did not hold in the data collected here. As such, we conclude that acoustic radiation ceases to be the singularly dominant damping mechanism for lithotripsy bubbles under physiological conditions with higher temperatures and saturation of dissolved gases. Lastly, the presence of asymmetries in many of the observed collapses hindered direct comparison of experimental data from various test conditions with model predictions. However, the model was found to capture the larger trends observed in the data and to accurately simulate published results for spherical bubble collapses under cold and degassed conditions.

In addition to the aforementioned work on gas-vapor bubble dynamics, practical issues associated with cavitation during SWL were also addressed. In particular, insights were gained regarding shock-to-shock variability in an electrohydraulic lithotripter and the collapse times of lithotripsy bubbles. To assess both shock-wave repeatability and the impact of a more highly focused reflector, the beamwidths of individual shock waves were measured

using a prototype hydrophone array. These measurements demonstrated that both the age of the electrodes as well as the reflector geometry affected the characteristics of the acoustic field. Also, secondary effects associated with the cavitation field were documented to be stronger when the more highly focused reflector was used.[97] To better understand bubble collapse times, two models from the literature for bubble clusters were implemented.[86,87] These models were used to analyze bubble collapse times directly as well as to explore the effects of scattering on hydrophone measurements. Calculations suggested that observed collapse times cannot be explained solely by bubble interactions. Moreover, scattering within bubble clusters was identified as a mechanism by which the tensile portion of a measured shock wave can be reduced without attenuating the incident shock wave itself. Characterization of these scattering effects comprises an ongoing collaborative effort with other groups.[95] Lastly, an alternative mechanism for explaining experimentally observed collapse times was proposed. Based upon the shapes of experimental radius-time curves and preliminary calculations by Oleg Sapozhnikov,[88] acoustic reverberations inside the ellipsoidal reflector appear to be sufficient to lengthen bubble collapse times.

8.2 Future Work

The model developed and tested in this effort represents a tool that can be used to better understand bubble dynamics in therapeutic ultrasound. Considering that the complementary side of energy retained by a collapsing bubble is the energy deposited, the model and the experimental data yield insights into energy deposition during therapeutic ultrasound. To the extent that bubbles are implicated in a given therapy, the corresponding energy deposition can be clinically relevant. For example, cavitation has been particularly implicated in the comminution of small renal stones during SWL and this effect has been studied relative to pressures radiated from collapsing bubbles. However prior studies have typically not considered vapor trapping and the sensitivity to liquid conditions, as done here. Similarly, calculations that have been used to characterize bubble-enhanced heating during HIFU have been based upon acoustic radiation from inertially collapsing gas bubbles that remain symmetric. From the experimental results of Chapter 7, asymmetries during collapse can drastically reduce energy deposition caused by acoustic radiation. Overall,

the model and the experimental work associated with gas-vapor bubbles can be used to provide estimates of energy deposition by bubbles during SWL and HIFU. The modeling approach from Chapter 2 is well suited to such an anaylsis in that heat and mass transport are addressed while enforcing an energy balance on the contents of the bubble.

As discussed above, the scaling model presented in this work can be used to investigate energy deposition. This model is especially well suited to the analysis of a single collapse and rebound. However, as described in Section 2.2.3, solving the heat transport problem algebraically does not account for the evolution of a thermal boundary layer. Moreover, even though the Plesset-Zwick convolution implemented herein does simulate such a thermal boundary layer, this implementation is not numerically stable for more violent collapses. While the scaling model can be used to estimate energy deposition during an application of HIFU, it is insightful to further consider how the evolution of a thermal boundary layer over many acoustic cycles might affect the bubble dynamics. In an earlier modeling effort, the heat transport component of a model developed by Yasui[98] was used to study HIFU bubbles. Although Yasui's approach involved certain assumptions and limitations, it did provide a method for approximating cumulative effects in a thermal boundary layer. Simulations with this model suggested that vapor effects associated with elevated temperatures in a boundary layer could qualitatively alter the bubble's behavior.[56] More specifically, the simulations predicted that the bubble would achieve a larger maximum radius and collapse less frequently during HIFU excitation when a thermally significant boundary layer occurred. Such a change in the dynamics would affect the rate of rectified diffusion of non-condensable gases, which occurs on a time scale proportional to R^4 from Equation (2.42). Importantly, for treatments with repeated pulses of HIFU, non-condensable gases determine bubble dissolution times between pulses. One way to test these predictions experimentally would be to directly observe a bubble's maximum radius and/or its frequency of collapse during exposure to HIFU. Although such direct measurments remain challenging, related photographic observations have been obtained just after HIFU was stopped.[54] In these experiments, a bubble was observed to grow monotonically for a brief period *after* application of HIFU. If a superheated boundary layer evolved during exposure to HIFU, then the observed growth could be interpreted as 'transient boiling' whereby the bubble grew as a vapor bubble in a

superheated liquid until the energy in the boundary layer was exhausted. The possibility of such 'boilng' behavior emphasizes the necessity of considering vapor and heat transport in the liquid in the bubble model. Overall, further analytical and experimental work is needed to elucidate the role of thermal boundary layers for HIFU bubbles.

To date, chemistry has not been addressed in the energy balance enforced in the bubble model proposed in this effort. Based on work from Didenko and Suslick,[80] it is reasonable to expect that chemical reactions are not of primary importance to the energetics of violent collapses. However, further examination of the chemical and physiological environment of tissue may be of interest in the the context of cavitation and therapeutic ultrasound. In particular, research on decompression sickness has suggested that surface-active substances and metabolic effects likely play roles in the creation and stabilization of cavitation nuclei.[2] Because the size and location of these nuclei will clearly affect any cavitation behavior induced by SWL or HIFU, understanding and perhaps manipulating this chemistry may be useful for controlling cavitation effects.

END NOTES

1. M. R. Bailey, V. A. Khokhlova, O. A. Sapozhnikov, S. G. Kargl, and L. A. Crum. Physical mechanisms of the therapeutic effect of ultrasound (a review). *Acoustical Physics*, 49:369–388, 2003.

2. J. E. Blatteau, J. B. Souraud, E. Gempp, and A. Boussuges. Gas nuclei, their origin, and their role in bubble formation. *Aviation Space and Environmental Medicine*, 77 (10):1068–1076, Oct 2006.

3. L. Rayleigh. On the pressure developed in a liquid during the collapse of a spherical cavity. *Philosophical Magazine*, 34:94–98, 1917.

4. J. E. Kennedy, G. R. ter Haar, and D. Cranston. High intensity focused ultrasound: surgery of the future? *British Journal of Radiology*, 76:590–599, 2003.

5. F. Wu, Z.-B. Wang, Y.-D. Cao, Z.-L. Xu, Q. Zhou, H. Zhu, and W.-Z. Chen. Heat fixation of cancer cells ablated with high-intensity focused ultrasound in patients with breast cancer. *American Journal of Surgery*, 192(2):179–184, 2006.

6. Z. Xu, J. B. Fowlkes, E. D. Rothman, A. M. Levin, and C. A. Cain. Controlled ultrasound tissue erosion: The role of dynamic interaction between insonation and microbubble activity. *Journal of the Acoustical Society of America*, 117:424–435, 2005.

7. T. L. Hall, K. Kieran, K. Ives, J. B. Fowlkes, C. A. Cain, and W. W. Roberts. Histotripsy of rabbit renal tissue in vivo: temporal histologic trends. *Journal of Endourology*, 21(10):1159–1166, 2007.

8. S. L. Poliachik, W. L. Chandler, R. J. Ollos, M. R. Bailey, and L. A. Crum. The relation between cavitation and platelet aggregation during exposure to high-intensity focused ultrasound. *Ultrasound in Medicine and Biology*, 30(2):261–269, 2004.

9. V. Zderic, A. A. Brayman, S. R. Sharar, L. A. Crum, and S. Vaezy. Microbubble-enhanced hemorrhage control using high intensity focused ultrasound. *Ultrasonics*, 45 (1-4):113–120, 2006.

10. O. A. Sapozhnikov, V. A. Khokhlova, M. R. Bailey, J. C. Williams Jr., J. A. McAteer, R. O. Cleveland, and L. A. Crum. Effect of overpressure and pulse repetition frequency on cavitation in shock wave lithotripsy. *Journal of the Acoustical Society of America*, 112(3):1183–1195, 2002.

11. M. R. Bailey, Y. A. Pishchalnikov, O. A. Sapozhnikov, R. O. Cleveland, J. A. McAteer, N. A. Miller, I. V. Pishchalnikova, B. A. Connors, L. A. Crum, and A. P. Evan. Cavitation detection during shock-wave lithotripsy. *Ultrasound in Medicine and Biology*, 31(9):1245–1256, 2005.

12. A. P. Evan, J. A. McAteer, B. A. Connors, P. M. Blomgren, and J. E. Lingeman. Renal injury during shock wave lithotripsy is significantly reduced by slowing the rate of shock wave delivery. *BJU International*, 100(3):624–627, 2007.

13. F. Chavrier, J.-Y. Chapelon, A. Gelet, and D. Cathignol. Modeling of high-intensity focused ultrasound-induced lesions in the presence of cavitation bubbles. *Journal of the Acoustical Society of America*, 108:432–440, 2000.

14. Y. A. Pishchalnikov, O. A. Sapozhnikov, M. R. Bailey, I. V. Pishchalnikova, J. C. Williams Jr., and J. A. McAteer. Cavitation selectively reduces the negative-pressure phase of lithotripter shock pulses. *Acoustics Research Letters Online*, 6:280–286, 2005.

15. M. R. Bailey, L. N. Couret, O. A. Sapozhnikov, V. A. Khokhlova, G. ter Haar, S. Vaezy, X. G. Shi, R. Martin, and L. A. Crum. Use of overpressure to assess the role of bubbles in focused ultrasound lesion shape in vitro. *Ultrasound in Medicine and Biology*, 27:695–708, 2001.

16. B. A. Rabkin, V. Zderic, L. A. Crum, and S. Vaezy. Biological and physical mechanisms of hifu-induced hyperecho in ultrasound images. *Ultrasound in Medicine and Biology*, 32(11):1721–1729, 2006.

17. J. E. Kennedy, F. Wu, G. R. ter Haar, F. V. Gleeson, R. R. Phillips, M. R. Middleton, and D. Cranston. High-intensity focused ultrasound for the treatment of liver tumours. *Ultrasonics*, 42(1-9):931–935, 2004.

18. V. G. Zarnitsyn, A. R. Prausnitz, and Y. A. Chizmadzhev. Physical methods of nucleic acid delivery into cells and tissues. *Biologicheskie Membrany*, 21:355–373, 2004.

19. R. G. Holt and R. A. Roy. Measurements of bubble-enhanced heating from focused, mhz-frequency ultrasound in a tissue-mimicking material. *Ultrasound in Medicine and Biology*, 27:1399–1412, 2001.

20. C. C. Coussios, C. H. Farny, G. ter Haar, and R. A. Roy. Role of acoustic cavitation in the delivery and monitoring of cancer treatment by high-intensity focused ultrasound (hifu). *International Journal of Hyperthermia*, 23(2):105–120, 2007.

21. Y. A. Pishchalnikov, O. A. Sapozhnikov, M. R. Bailey, J. C. Williams Jr., R. O. Cleveland, T. Colonius, L. A. Crum, A. P. Evan, and J. A. McAteer. Cavitation bubble cluster activity in the breakage of kidney stones by lithotripter shockwaves. *Journal of Endourology*, 17:435–446, 2003.

22. T. Ikeda, S. Yoshizawa, M. Tosaki, J. S. Allen, S. Takagi, N. Ohta, T. Kitamura, and Y. Matsumoto. Cloud cavitation control for lithotripsy using high intensity focused ultrasound. *Ultrasound in Medicine and Biology*, 32(9):1383 – 1397, 2006. Cloud cavitation;Lithotripsy;High intensity focused ultrasound (HIFU);Low-frequency waves;.

23. Z. Xu, A. Ludomirsky, L. Y. Eun, T. L. Hall, B. C. Tran, J. B. Fowlkes, and C. A. Cain. Controlled ultrasound tissue erosion. *IEEE Transactions on Ultrasonics, Ferroelectrics, and Frequency Control*, 51(6):726–736, 2004.

24. Y. Kaneko, T. Maruyama, K. Takegami, T. Watanabe, H. Mitsui, K. Hanajiri, H. Nagawa, and Y. Matsumoto. Use of a microbubble agent to increase the effects of high intensity focused ultrasound on liver tissue. *European Radiology*, 15(7):1415–1420, 2005.

25. P. V. Chitnis and R. O. Cleveland. Quantitative measurements of acoustic emissions from cavitation at the surface of a stone in response to a lithotripter shock wave. *Journal of the Acoustical Society of America*, 119(4):1929–1932, 2006.

26. Y. Matsumoto, J. S. Allen, S. Yoshizawa, T. Ikeda, and Y. Kaneko. Medical ultrasound with microbubbles. *Experimental Thermal and Fluid Science*, 29:255–265, 2005.

27. V. A. Khokhlova, M. R. Bailey, J. A. Reed, B. W. Cunitz, P. J. Kaczkowski, and L. A. Crum. Effects of nonlinear propagation, cavitation, and boiling in lesion formation by high intensity focused ultrasound in a gel phantom. *Journal of the Acoustical Society of America*, 119(3):1834–1848, 2006.

28. U. Parlitz, R. Mettin, S. Luther, I. Akhatov, M. Voss, and W. Lauterborn. Spatio-temporal dynamics of acoustic cavitation bubble clouds. *Philosophical Transactions of the Royal Society of London Series A*, 357:313–334, 1999.

29. M. S. Plesset and D. Y. Hsieh. Theory of gas bubble dynamics in oscillating pressure fields. *Physics of Fluids*, 3(6):882–892, 1960.

30. Y. Matsumoto and F. Takemura. Influence of internal phenomena on gas bubble motion (effects of thermal-diffusion, phase-change on the gas-liquid interface and mass diffusion between vapor and noncondensable gas in the collapsing phase). *JSME International Journal Series B—Fluids and Thermal Engineering*, 37:288–296, 1994.

31. V. Q. Vuong and A. J. Szeri. Sonoluminescence and diffusive transport. *Physics of Fluids*, 8(9):2354–2364, Sep 1996.

32. A. T. Preston. *Modeling Heat and Mass Transfer in Bubbly Cavitating Flows and Shock Waves in Cavitating Nozzles*. PhD thesis, California Institute of Technology, Pasadena, California, 2004.

33. H. Lin, B. D. Storey, and A. J. Szeri. Inertially driven inhomogeneities in violently collapsing bubbles: the validity of the Rayleigh–Plesset equation. *Journal of Fluid Mechanics*, 452:145–162, 2002.

34. R. Toegel, B. Gompf, R. Pecha, and D. Lohse. Does water vapor prevent upscaling sonoluminescence? *Physical Review Letters*, 85(15):3165–3168, 2000.

35. B. D. Storey and A. J. Szeri. A reduced model of cavitation physics for use in sono-chemistry. *Proceedings of the Royal Society of London Series A*, 457:1685–1700, 2001.

36. T. J. Matula, P. R. Hilmo, B. D. Storey, and A. J. Szeri. Radial response of individual bubbles subjected to shock wave lithotripsy pulses *in vitro*. *Physics of Fluids*, 14(3): 913–921, 2002.

37. R. Lofstedt, B. P. Barber, and S. J. Putterman. Toward a hydrodynamic theory of sonoluminescence. *Physics of Fluids A—Fluid Dynamics*, 5(11):2911–2928, Nov 1993.

38. B. D. Storey and A. J. Szeri. Mixture segregation within sonoluminescence bubbles. *Journal of Fluid Mechanics*, 396:203–221, Oct 1999.

39. B. D. Storey and A. J. Szeri. Water vapour, sonoluminescence and sonochemistry. *Proceedings of the Royal Society of London Series A*, 456:1685–1709, 2000.

40. R. Toegel and D. Lohse. Phase diagrams for sonoluminescing bubbles: A comparison between experiment and theory. *Journal of Chemical Physics*, 118(4):1863–1875, Jan 2003.

41. K. Yasui. Alternative model of single-bubble sonoluminescence. *Physical Review E*, 56:6750–6760, 1997.

42. I. Akhatov, O. Lindau, A. Topolnikov, R. Mettin, N. Vakhitova, and W. Lauterborn. Collapse and rebound of a laser-induced cavitation bubble. *Physics of Fluids*, 13(10): 2805–2819, Oct 2001.

43. A. Vogel and W. Lauterborn. Acoustic transient generation by laser-produced cavitation bubbles near solid boundaries. *Journal of the Acoustical Society of America*, 84(2):719–731, Aug 1988.

44. A. Vogel, W. Lauterborn, and R. Timm. Optical and acoustic investigations of the dynamics of laser-produced cavitation bubbles near a solid boundary. *Journal of Fluid Mechanics*, 206:299–338, Sep 1989.

45. B. A. Rabkin, V. Zderic, and S. Vaezy. Hyperecho in ultrasound images of hifu therapy: Involvement of cavitation. *Ultrasound in Medicine and Biology*, 31:947–956, 2005.

46. X. M. Yang, R. A. Roy, and R. G. Holt. Bubble dynamics and size distributions during focused ultrasound insonation. *Journal of the Acoustical Society of America*, 116:3423–3431, 2004.

47. E. Johnsen, T. Colonius, W. Kreider, and M. R. Bailey. Axisymmetric collapse of an air bubble subjected to a lithotripter pulse. In *Proceedings of IMECE07 ASME 2007 International Mechanical Engineering Congress & Exposition, November 11-15, 2007, Seattle, USA*, 2007.

48. G. N. Sankin, W. N. Simmons, S. L. Zhu, and P. Zhong. Shock wave interaction with laser-generated single bubbles. *Physical Review Letters*, 95(3):034501, Jul 2005.

49. P. Zhong, Y. F. Zhou, and S. L. Zhu. Dynamics of bubble oscillation in constrained media and mechanisms of vessel rupture in swl. *Ultrasound in Medicine and Biology*, 27(1):119–134, Jan 2001.

50. S. P. Qin, Y. T. Hu, and Q. Jiang. Oscillatory interaction between bubbles and confining microvessels and its implications on clinical vascular injuries of shock-wave lithotripsy. *IEEE Transactions on Ultrasonics, Ferroelectrics, and Frequency Control*, 53(7):1322–1329, Jul 2006. ISSN 0885-3010.

51. C. C. Church. A theoretical study of cavitation generated by an extracorporeal shock wave lithotripter. *Journal of the Acoustical Society of America*, 86(1):215–227, 1989.

52. T. J. Matula, P. R. Hilmo, M. R. Bailey, and L. A. Crum. In vitro sonoluminescence and sonochemistry studies with an electrohydraulic shock-wave lithotripter. *Ultrasound in Medicine and Biology*, 28(9):1199–1207, 2002.

53. M. S. Canney, M. R. Bailey, V. A. Khokhlova, and L. A. Crum. Millisecond initiation of boiling by high-intensity focused ultrasound in tissue-mimicking phantoms. *Journal of the Acoustical Society of America*, 120:3110, 2006. (abstract for conference presentation).

54. M. S. Canney, W. Kreider, M. R. Bailey, V. A. Khokhlova, and L. A. Crum. Observations of cavitation and boiling in a tissue-mimicking phantom due to high intensity focused ultrasound. *Journal of the Acoustical Society of America*, 122:3079, 2007. (abstract for conference presentation).

55. C. C. Coussios and R. A. Roy. Applications of acoustics and cavitation to noninvasive therapy and drug delivery. *Annual Review of Fluid Mechanics*, 40:395–420, 2008.

56. W. Kreider, M. R. Bailey, and L. A. Crum. Modeling of initial bubble growth rates during high-intensity focused ultrasound. *Journal of the Acoustical Society of America*, 117(4):2474–2474, 2005. URL http://link.aip.org/link/?JAS/117/2474/3. (abstract for conference presentation).

57. W. Kreider, M. R. Bailey, and L. A. Crum. What is boiling during high-intensity focused ultrasound. *Journal of the Acoustical Society of America*, 119(5):3228–3228, 2006. (abstract for conference presentation).

58. P. K. Kundu and I. M. Cohen. *Fluid Mechanics*. Academic Press, San Diego, second edition, 2002.

59. A. Prosperetti and A. Lezzi. Bubble dynamics in a compressible liquid. Part 1. First-order theory. *Journal of Fluid Mechanics*, 168:457–478, 1986.

60. Y. Hao and A. Prosperetti. The dynamics of vapor bubbles in acoustic pressure fields. *Physics of Fluids*, 11:2008–2019, 1999.

61. A. Prosperetti, L. A. Crum, and K. W. Commander. Nonlinear bubble dynamics. *Journal of the Acoustical Society of America*, 83(2):502–514, 1988.

62. J. R. MacDonald. Some Simple Isothermal Equations of State. *Reviews of Modern Physics*, 38(4):669–679, 1966.

63. B. E. Poling, J. M. Prausnitz, and J. P. O'Connell. *The properties of gases and liquids*. McGraw-Hill, 2001.

64. V. P. Carey. *Liquid–vapor phase-change phenomena*. Series in Chemical and Mechanical Engineering. Hemisphere Publishing Corporation, Washington, 1992.

65. J. A. Fay. *Molecular Thermodynamics*. Addison-Wesley, Reading, MA, 1965.

66. S. K. Loyalka and J. H. Ferziger. Model Dependence of the Temperature Slip Coefficient. *Physics of Fluids*, 11(8):1668–1671, 1968.

67. M. M. van Iersel, J. Cornel, N. E. Benes, and J. T. F. Keurentjes. Inhibition of nonlinear acoustic cavitation dynamics in liquid co2. *Journal of Chemical Physics*, 126(6):064508, 2007.

68. F. Sharipov and D. Kalempa. Velocity slip and temperature jump coefficients for gaseous mixtures. iv. temperature jump coefficient. *International Journal of Heat and Mass Transfer*, 48(6):1076–1083, Mar 2005.

69. T. G. Leighton. *The Acoustic Bubble*. Academic Press, San Diego, 1994.

70. L. D. Rozenberg, editor. *High-Intensity Ultrasonic Fields*, pages 201–259. Plenum Press, New York, 1971. Part IV, "Pulsations of Cavitation Voids," by V. A. Akulichev.

71. J. B. Keller and M. Miksis. Bubble oscillations of large amplitude. *Journal of the Acoustical Society of America*, 68(2):628–633, 1980.

72. FR Gilmore. The growth or collapse of a spherical bubble in a viscous compressible liquid. Technical Report 26-4, California Institute of Technology, 1952.

73. H. Poritsky. The collapse or growth of a spherical bubble or cavity in a viscous fluid. In E. Sternberg, editor, *Proceedings of the First U.S. National Congress on Applied Mechanics, New York*, pages 813–821, 1952.

74. A. Eller and H. G. Flynn. Rectified diffusion during nonlinear pulsations of cavitation bubbles. *Journal of the Acoustical Society of America*, 37(3):493–503, 1965.

75. M. S. Plesset and S. A. Zwick. A nonsteady heat diffusion problem with spherical symmetry. *Journal of Applied Physics*, 23(1):95–98, 1952.

76. M. M. Fyrillas and A. J. Szeri. Dissolution or growth of soluble spherical oscillating bubbles. *Journal of Fluid Mechanics*, 277:381–407, 1994.

77. Free Software Foundation, Inc. GNU Fortran compiler, 2007. URL http://gcc.gnu.org/fortran/.

78. J. R. Cash and A. H. Karp. A variable order runge-kutta method for initial-value problems with rapidly varying right-hand sides. *ACM Transactions on Mathematical Software*, 16:201–222, 1990.

79. M. S. Plesset and S. A. Zwick. The growth of vapor bubbles in superheated liquids. *Journal of Applied Physics*, 25(4):493–500, 1954.

80. Y. T. Didenko and K. S. Suslick. The energy efficiency of formation of photons, radicals and ions during single-bubble cavitation. *Nature*, 418(6896):394–397, Jul 2002.

81. R. O. Cleveland, O. A. Sapozhnikov, M. R. Bailey, and L. A. Crum. A dual passive cavitation detector for localized detection of lithotripsy-induced cavitation in vitro. *Journal of the Acoustical Society of America*, 107:1745–1758, 2000.

82. R. O. Cleveland, M. R. Bailey, N. Fineberg, B. Hartenbaum, M. Lokhandwalla, J. A. McAteer, and B. Sturtevant. Design and characterization of a research electrohydraulic lithotripter patterned after the dornier HM3. *Review of Scientific Instruments*, 71:2514–2525, 2000.

83. Wayne Kreider, Michael R. Bailey, and Lawrence A. Crum. Modeling of bubble oscillations induced by a lithotripter pulse. In Anthony A. Atchley, Victor W. Sparrow, and

Robert M. Keolian, editors, *Innovations in Nonlinear Acoustics: ISNA17—17th International Symposium on Nonlinear Acoustics*, volume 838, pages 315–318, Melville, NY, USA, 2006. AIP. URL http://link.aip.org/link/?APC/838/315/1.

84. David R. Lide, editor. *CRC handbook of chemistry and physics, internet version 2007* <http://www.hbcpnetbase.com>. Taylor and Francis, Boca Raton, FL, 87th edition, 2007. URL http://www.hbcpnetbase.com.

85. C. E. Brennen. *Cavitation and bubble dynamics*. Oxford University Press New York, 1995.

86. M. Arora, C. D. Ohl, and D. Lohse. Effect of nuclei concentration on cavitation cluster dynamics. *Journal of the Acoustical Society of America*, 121(6):3432–3436, Jun 2007. ISSN 0001-4966.

87. M. F. Hamilton, Y. A. Ilinskii, G. D. Meegan, and E. A. Zabolotskaya. Interaction of bubbles in a cluster near a rigid surface. *Acoustics Research Letters Online*, 6: 207–213, 2005.

88. O. Sapozhnikov, W. Kreider, M. R. Bailey, V. A. Khokhlova, and F. Curra. Effect of elastic waves in the metal reflector on bubble dynamics at the focus of an electro-hydraulic lithotripter. To be presented at Acoustics'08 (joint meeting of ASA, EAA, SFA), June 29–July 4, 2008, Paris, France, 2008.

89. J. I. Iloreta, Y. F. Zhou, G. N. Sankin, P. Zhong, and A. J. Szeri. Assessment of shock wave lithotripters via cavitation potential. *Physics of Fluids*, 19(8):085103, Aug 2007. ISSN 1070-6631.

90. X. F. Xi and P. Zhong. Improvement of stone fragmentation during shock-wave lithotripsy using a combined EH/PEAA shock-wave generator—in vitro experiments. *Ultrasound in Medicine and Biology*, 26(3):457–467, Mar 2000. ISSN 0301-5629.

91. Michel Tanguay. *Computation of bubbly cavitating flow in shock wave lithotripsy*. PhD thesis, California Institute of Technology, Pasadena, CA, 2004.

92. M. Liebler, T. Dreyer, and R. E. Riedlinger. Nonlinear modeling of interactions between ultrasound propagation and cavitation bubbles. *Acta Acustica United with Acustica*, 92(1):165–167, Jan-Feb 2006.

93. Y. A. Pishchalnikov, J. A. McAteer, W. Kreider, J. C. Williams Jr., I. V. Pishchalnikova, and M. R. Bailey. Influence of cavitation on lithotripter shock waves. In A. Calvo-Manzano, A. Perez-Lopez, and J. S. Santiago, editors, *Proceedings of the 19th International Congress on Acoustics, Madrid, Spain, September 2–7, 2007*, pages 1–6, paper NLA–02–005–IP, 2007. URL http://www.sea-acustica.es/WEB_ICA_07/fchrs/contents.htm.

94. Y. A Pishchalnikov, J. S. Neucks, R. J. VonDerHaar, I. V. Pishchalnikova, J. C. Williams Jr., and J. A. McAteer. Air pockets trapped during routine coupling in dry head lithotripsy can significantly decrease the delivery of shock wave energy. *Journal of Urology*, 176(6 Pt 1):2706–2710, 2006.

95. W. Kreider, Y. A. Pishchalnikov, T. A. Hay, M. R. Bailey, J. A. McAteer, and M. F. Hamilton. Local effects of bubble clusters on measurements of lithotripter shock waves. Presentation at IMECE07 ASME 2007 International Mechanical Engineering Congress & Exposition, November 11-15, 2007, Seattle, USA, 2007.

96. A. J. Szeri, B. D. Storey, A. Pearson, and J. R. Blake. Heat and mass transfer during the violent collapse of nonspherical bubbles. *Physics of Fluids*, 15(9):2576–2586, Sep 2003.

97. W. Kreider, M. R. Bailey, and J. A. Ketterling. Beamwidth measurement of individual lithotripter shock waves. *Journal of the Acoustical Society of America*, submitted January 2008.

98. K. Yasui. Variation of liquid temperature at bubble wall near the sonoluminescence threshold. *Journal of the Physical Society of Japan*, 65(9):2830–2840, 1996.

99. W. Wagner and A. Pruß. The IAPWS formulation 1995 for the thermodynamic properties of ordinary water substance for general and scientific use. *Journal of Physical and Chemical Reference Data*, 31(2):387–535, 2002.

100. P. M. Silverberg and L. A. Wenzel. The variation of latent heat with temperature. *Journal of Chemical and Engineering Data*, 10(4):363–366, 1965.

101. N. Bilaniuk and G. S. K. Wong. Speed of sound in pure water as a function of temperature. *Journal of the Acoustical Society of America*, 93(3):1609–1612, 1993.

102. N. Bilaniuk and G. S. K. Wong. Erratum: Speed of sound in pure water as a function of temperature. *Journal of the Acoustical Society of America*, 99(5):3257, 1996.

103. R. C. Reid and T. K. Sherwood. *The properties of gases and liquids*. McGraw-Hill, New York, 2nd edition, 1966.

104. J. Kestin, J. V. Sengers, B. Kamgar-Parsi, and J. M. H. Levelt Sengers. Thermophysical properties of fluid H_2O. *Journal of Physical and Chemical Reference Data*, 13(1): 175–183, 1984.

105. J. Kestin and J. H. Whitelaw. Sixth international conference on the properties of steam—transport properties of water substance. *Journal of Engineering for Power—Transactions of the ASME*, 88(1):82–104, 1966.

106. R. Battino, T. R. Rettich, and T. Tominaga. The solubility of nitrogen and air in liquids. *Journal of Physical and Chemical Reference Data*, 13(2):563–600, 1984.

107. E. S. Domalski and E. D. Hearing. *NIST Chemistry WebBook, NIST Standard Reference Database Number 69*, chapter Condensed Phase Heat Capacity Data. National Institute of Standards and Technology, P. J. Linstrom and W. G. Mallard, Gaithersburg MD, 20899, June 2005. URL http://webbook.nist.gov/cgi/cbook.cgi?Name=water&Units=SI&cTC=on.

108. D. F. Othmer and M. S. Thakar. Correlating Diffusion Coefficient in Liquids. *Industrial and Engineering Chemistry*, 45(3):589–593, 1953.

109. J. O. Hirschfelder, C. F. Curtiss, and R. B. Bird. *Molecular theory of gases and liquids*. John Wiley & Sons, New York, 1954.

110. K. Yasui. Effects of thermal conduction on bubble dynamics near the sonoluminescence threshold. *Journal of the Acoustical Society of America*, 98:2772–2782, 1995.

111. M. S. Pearle, E. A. Calhoun, and G. C. Curhan. Urologic diseases in america project: urolithiasis. *Journal of Urology*, 173(3):848–857, 2005.

112. A. P. Evan, J. A. McAteer, J. C. Williams Jr., L. R. Willis, M. R. Bailey, L. A. Crum, J. E. Lingeman, and R. O. Cleveland. Shock wave physics of lithotripsy: Mechanisms of shock wave action and progress toward improved SWL. In R. Moore, J.T. Bishoff, S. Loening, and S.G. Docimo, editors, *Textbook of Minimally Invasive Urology*, pages 425–438. Martin Dunitz Limited, London, 2004.

113. K. Kerbl, J. Rehman, J. Landman, D. Lee, C. Sundaram, and R. V. Clayman. Current management of urolithiasis: progress or regress? *Journal of Endourology*, 16(5):281–288, 2002.

114. J. E. Lingeman. Extracorporeal shock wave lithotripsy devices: Are we making progress? In J. E. Lingeman and G. M. Preminger, editors, *New Developments in the Management of Urolithiasis*, pages 79–96. Igaku-Shoin, New York, 1996.

115. J. A. McAteer, M. R. Bailey, J. C. Williams Jr., R. O. Cleveland, and A. P. Evan. Strategies for improved shock wave lithotripsy. *Minerva Urologica e Nefrologica*, 57(4):271–287, 2005.

116. R. O. Cleveland, R. Anglade, and R. K. Babayan. Effect of stone motion on in vitro comminution efficiency of Storz Modulith SLX. *Journal of Endourology*, 18(7):629–633, 2004.

117. R. O. Cleveland and O. A. Sapozhnikov. Modeling elastic wave propagation in kidney stones with application to shock wave lithotripsy. *Journal of the Acoustical Society of America*, 118(4):2667–2676, 2005.

118. W. Eisenmenger. The mechanisms of stone fragmentation in ESWL. *Ultrasound in Medicine and Biology*, 27(5):683–693, 2001.

119. O. A. Sapozhnikov, A. D. Maxwell, B. MacConaghy, and M. R. Bailey. A mechanistic analysis of stone fracture in lithotripsy. *Journal of the Acoustical Society of America*, 121(2):1190–1202, 2007.

120. A. J. Coleman, J. E. Saunders, R. C. Preston, and D. R. Bacon. Pressure waveforms generated by a Dornier extra-corporeal shock-wave lithotripter. *Ultrasound in Medicine and Biology*, 13(10):651–657, 1987. ISSN 0301-5629 (Print).

121. J. A. Ketterling, O. Aristizábal, D. H. Turnbull, and F. L. Lizzi. Design and fabrication of a 40-MHz annular array transducer. *IEEE Transactions on Ultrasonics, Ferroelectrics, and Frequency Control*, 52(4):672–681, 2005. ISSN 0885-3010 (Print).

122. W. Kreider, L. A. Crum, M. R. Bailey, T. J. Matula, V. A. Khokhlova, and O. A. Sapozhnikov. Acoustic cavitation and medical ultrasound. In *Proceedings of the Sixth International Symposium on Cavitation (CAV2006)*, 2006. online only, Paper #9.

123. O. A. Sapozhnikov, M. R. Bailey, and L. A. Crum. Shot-to-shot variability of acoustic axis of a spark-source lithotripter. *Journal of the Acoustical Society of America*, 105: 1269, 1999. (Abstract for presentation at the 137th Meeting of the Acoustical Society of America).

124. R. O. Cleveland, D. A. Lifshitz, B. A. Connors, A. P. Evan, L. R. Willis, and L. A. Crum. In vivo pressure measurements of lithotripsy shock waves in pigs. *Ultrasound in Medicine and Biology*, 24(2):293–306, 1998.

BIBLIOGRAPHY

Akhatov, I., Lindau, O., Topolnikov, A., Mettin, R., Vakhitova, N., and Lauterborn, W. (2001). Collapse and rebound of a laser-induced cavitation bubble. *Physics of Fluids*, 13(10):2805–2819.

Akhatov, I., Vakhitova, N., Topolnikov, A., Zakirov, K., Wolfrum, B., Kurz, T., Lindau, O., Mettin, R., and Lauterborn, W. (2002). Dynamics of laser-induced cavitation bubbles. *Experimental Thermal and Fluid Science*, 26(6-7):731–737.

Arora, M., Ohl, C. D., and Lohse, D. (2007). Effect of nuclei concentration on cavitation cluster dynamics. *Journal of the Acoustical Society of America*, 121(6):3432–3436.

Bailey, M. R., Couret, L. N., Sapozhnikov, O. A., Khokhlova, V. A., ter Haar, G., Vaezy, S., Shi, X. G., Martin, R., and Crum, L. A. (2001). Use of overpressure to assess the role of bubbles in focused ultrasound lesion shape in vitro. *Ultrasound in Medicine and Biology*, 27:695–708.

Bailey, M. R., Khokhlova, V. A., Sapozhnikov, O. A., Kargl, S. G., and Crum, L. A. (2003). Physical mechanisms of the therapeutic effect of ultrasound (a review). *Acoustical Physics*, 49:369–388.

Bailey, M. R., Pishchalnikov, Y. A., Sapozhnikov, O. A., Cleveland, R. O., McAteer, J. A., Miller, N. A., Pishchalnikova, I. V., Connors, B. A., Crum, L. A., and Evan, A. P. (2005). Cavitation detection during shock-wave lithotripsy. *Ultrasound in Medicine and Biology*, 31(9):1245–1256.

Battino, R., Rettich, T. R., and Tominaga, T. (1984). The solubility of nitrogen and air in liquids. *Journal of Physical and Chemical Reference Data*, 13(2):563–600.

Bilaniuk, N. and Wong, G. S. K. (1993). Speed of sound in pure water as a function of temperature. *Journal of the Acoustical Society of America*, 93(3):1609–1612.

Bilaniuk, N. and Wong, G. S. K. (1996). Erratum: Speed of sound in pure water as a function of temperature. *Journal of the Acoustical Society of America*, 99(5):3257.

Blake, J. R. and Gibson, D. C. (1987). Cavitation bubbles near boundaries. *Annual Review of Fluid Mechanics*, 19:99–123.

134

Blatteau, J. E., Souraud, J. B., Gempp, E., and Boussuges, A. (2006). Gas nuclei, their origin, and their role in bubble formation. *Aviation Space and Environmental Medicine*, 77(10):1068–1076.

Bourne, N. K. and Field, J. E. (1992). Shock-induced collapse of single cavities in liquids. *Journal of Fluid Mechanics*, 244:225–240.

Brennen, C. E. (1995). *Cavitation and bubble dynamics*. Oxford University Press New York.

Bridgman, P. W. (1935). The Pressure-Volume-Temperature Relations of the Liquid, and the Phase Diagram of Heavy Water. *Journal of Chemical Physics*, 3(10):597–605.

Brujan, E. A. (2004). The role of cavitation microjets in the therapeutic applications of ultrasound. *Ultrasound in Medicine and Biology*, 30:381–387.

Brujan, E. A., Ikeda, T., and Matsumoto, Y. (2004). Dynamics of ultrasound-induced cavitation bubbles in non-newtonian liquids and near a rigid boundary. *Physics of Fluids*, 16:2402–2410.

Canney, M. S., Bailey, M. R., Khokhlova, V. A., and Crum, L. A. (2006). Millisecond initiation of boiling by high-intensity focused ultrasound in tissue-mimicking phantoms. *Journal of the Acoustical Society of America*, 120:3110. (abstract for conference presentation).

Canney, M. S., Kreider, W., Bailey, M. R., Khokhlova, V. A., and Crum, L. A. (2007). Observations of cavitation and boiling in a tissue-mimicking phantom due to high intensity focused ultrasound. *Journal of the Acoustical Society of America*, 122:3079. (abstract for conference presentation).

Carey, V. P. (1992). *Liquid–vapor phase-change phenomena*. Series in Chemical and Mechanical Engineering. Hemisphere Publishing Corporation, Washington.

Cash, J. R. and Karp, A. H. (1990). A variable order runge-kutta method for initial-value problems with rapidly varying right-hand sides. *ACM Transactions on Mathematical Software*, 16:201–222.

Chappell, M. A. and Payne, S. J. (2006a). A physiological model of gas pockets in crevices and their behavior under compression. *Respiratory Physiology and Neurobiology*, 152(1):100–114.

Chappell, M. A. and Payne, S. J. (2006b). A physiological model of the release of gas bubbles from crevices under decompression. *Respiratory Physiology and Neurobiology*, 153(2):166–180.

Chavrier, F., Chapelon, J.-Y., Gelet, A., and Cathignol, D. (2000). Modeling of high-intensity focused ultrasound-induced lesions in the presence of cavitation bubbles. *Journal of the Acoustical Society of America*, 108:432–440.

Chitnis, P. V. and Cleveland, R. O. (2006). Quantitative measurements of acoustic emissions from cavitation at the surface of a stone in response to a lithotripter shock wave. *Journal of the Acoustical Society of America*, 119(4):1929–1932.

Church, C. C. (1989). A theoretical study of cavitation generated by an extracorporeal shock wave lithotripter. *Journal of the Acoustical Society of America*, 86(1):215–227.

Church, C. C. (1995). The effects of an elastic solid-surface layer on the radial pulsations of gas-bubbles. *Journal of the Acoustical Society of America*, 97:1510–1521.

Cleveland, R. O., Anglade, R., and Babayan, R. K. (2004). Effect of stone motion on in vitro comminution efficiency of Storz Modulith SLX. *Journal of Endourology*, 18(7):629–633.

Cleveland, R. O., Bailey, M. R., Fineberg, N., Hartenbaum, B., Lokhandwalla, M., McAteer, J. A., and Sturtevant, B. (2000a). Design and characterization of a research electrohydraulic lithotripter patterned after the dornier HM3. *Review of Scientific Instruments*, 71:2514–2525.

Cleveland, R. O., Lifshitz, D. A., Connors, B. A., Evan, A. P., Willis, L. R., and Crum, L. A. (1998). In vivo pressure measurements of lithotripsy shock waves in pigs. *Ultrasound in Medicine and Biology*, 24(2):293–306.

Cleveland, R. O. and Sapozhnikov, O. A. (2005). Modeling elastic wave propagation in kidney stones with application to shock wave lithotripsy. *Journal of the Acoustical Society of America*, 118(4):2667–2676.

Cleveland, R. O., Sapozhnikov, O. A., Bailey, M. R., and Crum, L. A. (2000b). A dual passive cavitation detector for localized detection of lithotripsy-induced cavitation in vitro. *Journal of the Acoustical Society of America*, 107:1745–1758.

Cole, R. H. (1948). *Underwater Explosions*. Princeton University Press, Princeton, NJ.

Coleman, A. J., Saunders, J. E., Preston, R. C., and Bacon, D. R. (1987). Pressure waveforms generated by a Dornier extra-corporeal shock-wave lithotripter. *Ultrasound in Medicine and Biology*, 13(10):651–657.

Colonius, T., d'Auria, F., and Brennen, C. E. (2000). Acoustic saturation in bubbly cavitating flow adjacent to an oscillating wall. *Physics of Fluids*, 12(11):2752–2761.

136

Coussios, C. C., Farny, C. H., ter Haar, G., and Roy, R. A. (2007). Role of acoustic cavitation in the delivery and monitoring of cancer treatment by high-intensity focused ultrasound (hifu). *International Journal of Hyperthermia*, 23(2):105–120.

Coussios, C. C. and Roy, R. A. (2008). Applications of acoustics and cavitation to noninvasive therapy and drug delivery. *Annual Review of Fluid Mechanics*, 40:395–420.

Dear, J. P. and Field, J. E. (1988). A study of the collapse of arrays of cavities. *Journal of Fluid Mechanics*, 190:409–425.

Didenko, Y. T. and Suslick, K. S. (2002). The energy efficiency of formation of photons, radicals and ions during single-bubble cavitation. *Nature*, 418(6896):394–397.

Domalski, E. S. and Hearing, E. D. (2005). *NIST Chemistry WebBook, NIST Standard Reference Database Number 69*, chapter Condensed Phase Heat Capacity Data. National Institute of Standards and Technology, P. J. Linstrom and W. G. Mallard, Gaithersburg MD, 20899.

Duraiswami, R., Prabhukumar, S., and Chahine, G. L. (1998). Bubble counting using an inverse acoustic scattering method. *Journal of the Acoustical Society of America*, 104(5):2699–2717. This method is implemented and marketed by Dynaflow, Inc. (Jessup, MD).

Eisenmenger, W. (2001). The mechanisms of stone fragmentation in ESWL. *Ultrasound in Medicine and Biology*, 27(5):683–693.

Eller, A. and Flynn, H. G. (1965). Rectified diffusion during nonlinear pulsations of cavitation bubbles. *Journal of the Acoustical Society of America*, 37(3):493–503.

Epstein, P. S. and Plesset, M. S. (1950). On the stability of gas bubbles in liquid-gas solutions. *Journal of Chemical Physics*, 18(11).

Evan, A. P., McAteer, J. A., Connors, B. A., Blomgren, P. M., and Lingeman, J. E. (2007). Renal injury during shock wave lithotripsy is significantly reduced by slowing the rate of shock wave delivery. *BJU International*, 100(3):624–627.

Evan, A. P., McAteer, J. A., Williams Jr., J. C., Willis, L. R., Bailey, M. R., Crum, L. A., Lingeman, J. E., and Cleveland, R. O. (2004). Shock wave physics of lithotripsy: Mechanisms of shock wave action and progress toward improved SWL. In Moore, R., Bishoff, J., Loening, S., and Docimo, S., editors, *Textbook of Minimally Invasive Urology*, pages 425–438. Martin Dunitz Limited, London.

Fatemi, M. and Greenleaf, J. F. (1999). Vibro-acoustography: An imaging modality based on ultrasound-stimulated acoustic emission. *Proceedings of the National Academy of Sciences of the United States of America*, 96:6603–6608.

Fay, J. A. (1965). *Molecular Thermodynamics*. Addison-Wesley, Reading, MA.

Field, J. E. (1991). The physics of liquid impact, shock-wave interactions with cavities, and the implications to shock-wave lithotripsy. *Physics in Medicine and Biology*, 36(11):1475–1484.

Flynn, H. G. (1975). Cavitation dynamics. i. a mathematical formulation. *Journal of the Acoustical Society of America*, 57(6):1379–1396.

Free Software Foundation, Inc. (2007). GNU Fortran compiler.

Fyrillas, M. M. and Szeri, A. J. (1994). Dissolution or growth of soluble spherical oscillating bubbles. *Journal of Fluid Mechanics*, 277:381–407.

Gilmore, F. (1952). The growth or collapse of a spherical bubble in a viscous compressible liquid. Technical Report 26-4, California Institute of Technology.

Gumerov, N. A. (2000). Dynamics of vapor bubbles with nonequilibrium phase transitions in isotropic acoustic fields. *Physics of Fluids*, 12:71–88.

Hall, T. L., Kieran, K., Ives, K., Fowlkes, J. B., Cain, C. A., and Roberts, W. W. (2007). Histotripsy of rabbit renal tissue in vivo: temporal histologic trends. *Journal of Endourology*, 21(10):1159–1166.

Hamilton, M. F., Ilinskii, Y. A., Meegan, G. D., and Zabolotskaya, E. A. (2005). Interaction of bubbles in a cluster near a rigid surface. *Acoustics Research Letters Online*, 6:207–213.

Hao, Y. and Prosperetti, A. (1999). The dynamics of vapor bubbles in acoustic pressure fields. *Physics of Fluids*, 11:2008–2019.

Hatsopoulos, G. N. and Keenan, J. H. (1965). *Principles of General Thermodynamics*. John Wiley & Sons, Inc., New York.

Hirschfelder, J. O., Curtiss, C. F., and Bird, R. B. (1954). *Molecular theory of gases and liquids*. John Wiley & Sons, New York.

Holt, R. G. and Roy, R. A. (2001). Measurements of bubble-enhanced heating from focused, mhz-frequency ultrasound in a tissue-mimicking material. *Ultrasound in Medicine and Biology*, 27:1399–1412.

Ikeda, T., Yoshizawa, S., Tosaki, M., Allen, J. S., Takagi, S., Ohta, N., Kitamura, T., and Matsumoto, Y. (2006). Cloud cavitation control for lithotripsy using high intensity focused ultrasound. *Ultrasound in Medicine and Biology*, 32(9):1383 – 1397. Cloud cavitation;Lithotripsy;High intensity focused ultrasound (HIFU);Low-frequency waves;.

Iloreta, J. I., Zhou, Y. F., Sankin, G. N., Zhong, P., and Szeri, A. J. (2007). Assessment of shock wave lithotripters via cavitation potential. *Physics of Fluids*, 19(8):085103.

Incropera, F. P. and DeWitt, D. P. (1990). *Fundamentals of Heat and Mass Transfer.* Wiley, 3rd edition.

Johnsen, E., Colonius, T., Kreider, W., and Bailey, M. R. (2007). Axisymmetric collapse of an air bubble subjected to a lithotripter pulse. In *Proceedings of IMECE07 ASME 2007 International Mechanical Engineering Congress & Exposition, November 11-15, 2007, Seattle, USA.*

Kamath, V. and Prosperetti, A. (1989). Numerical-integration methods in gas-bubble dynamics. *Journal of the Acoustical Society of America*, 85:1538–1548.

Kaneko, Y., Maruyama, T., Takegami, K., Watanabe, T., Mitsui, H., Hanajiri, K., Nagawa, H., and Matsumoto, Y. (2005). Use of a microbubble agent to increase the effects of high intensity focused ultrasound on liver tissue. *European Radiology*, 15(7):1415–1420.

Keller, J. B. and Miksis, M. (1980). Bubble oscillations of large amplitude. *Journal of the Acoustical Society of America*, 68(2):628–633.

Kennedy, J. E. (2005). High-intensity focused ultrasound in the treatment of solid tumours. *Nature Reviews Cancer*, 5(4):321–327.

Kennedy, J. E., ter Haar, G. R., and Cranston, D. (2003). High intensity focused ultrasound: surgery of the future? *British Journal of Radiology*, 76:590–599.

Kennedy, J. E., Wu, F., ter Haar, G. R., Gleeson, F. V., Phillips, R. R., Middleton, M. R., and Cranston, D. (2004). High-intensity focused ultrasound for the treatment of liver tumours. *Ultrasonics*, 42(1-9):931–935.

Kerbl, K., Rehman, J., Landman, J., Lee, D., Sundaram, C., and Clayman, R. V. (2002). Current management of urolithiasis: progress or regress? *Journal of Endourology*, 16(5):281–288.

Kestin, J., Sengers, J. V., Kamgar-Parsi, B., and Levelt Sengers, J. M. H. (1984). Thermophysical properties of fluid H_2O. *Journal of Physical and Chemical Reference Data*, 13(1):175–183.

Kestin, J. and Whitelaw, J. H. (1966). Sixth international conference on the properties of steam—transport properties of water substance. *Journal of Engineering for Power—Transactions of the ASME*, 88(1):82–104.

Ketterling, J. A., Aristizábal, O., Turnbull, D. H., and Lizzi, F. L. (2005). Design and fabrication of a 40-MHz annular array transducer. *IEEE Transactions on Ultrasonics, Ferroelectrics, and Frequency Control*, 52(4):672–681.

Khokhlova, V. A., Bailey, M. R., Reed, J. A., Cunitz, B. W., Kaczkowski, P. J., and Crum, L. A. (2006). Effects of nonlinear propagation, cavitation, and boiling in lesion formation by high intensity focused ultrasound in a gel phantom. *Journal of the Acoustical Society of America*, 119(3):1834–1848.

Kreider, W., Bailey, M. R., and Crum, L. A. (2005). Modeling of initial bubble growth rates during high-intensity focused ultrasound. *Journal of the Acoustical Society of America*, 117(4):2474–2474. (abstract for conference presentation).

Kreider, W., Bailey, M. R., and Crum, L. A. (2006a). Modeling of bubble oscillations induced by a lithotripter pulse. In Atchley, A. A., Sparrow, V. W., and Keolian, R. M., editors, *Innovations in Nonlinear Acoustics: ISNA17—17th International Symposium on Nonlinear Acoustics*, volume 838, pages 315–318, Melville, NY, USA. AIP.

Kreider, W., Bailey, M. R., and Crum, L. A. (2006b). What is boiling during high-intensity focused ultrasound. *Journal of the Acoustical Society of America*, 119(5):3228–3228. (abstract for conference presentation).

Kreider, W., Bailey, M. R., Johnsen, E., Colonius, T., and Crum, L. A. (2007a). Asymmetric collapses of free-field lithotripsy bubbles. Presentation at IMECE07 ASME 2007 International Mechanical Engineering Congress & Exposition, November 11-15, 2007, Seattle, USA.

Kreider, W., Bailey, M. R., and Ketterling, J. A. (submitted January 2008). Beamwidth measurement of individual lithotripter shock waves. *Journal of the Acoustical Society of America*.

Kreider, W., Crum, L. A., Bailey, M. R., Matula, T. J., Khokhlova, V. A., and Sapozhnikov, O. A. (2006c). Acoustic cavitation and medical ultrasound. In *Proceedings of the Sixth International Symposium on Cavitation (CAV2006)*. online only, Paper #9.

Kreider, W., Pishchalnikov, Y. A., Hay, T. A., Bailey, M. R., McAteer, J. A., and Hamilton, M. F. (2007b). Local effects of bubble clusters on measurements of lithotripter shock waves. Presentation at IMECE07 ASME 2007 International Mechanical Engineering Congress & Exposition, November 11-15, 2007, Seattle, USA.

Kundu, P. K. and Cohen, I. M. (2002). *Fluid Mechanics*. Academic Press, San Diego, second edition.

Lafon, C., Zderic, V., Noble, M. L., Yuen, J. C., Kaczkowski, P. J., Sapozhnikov, O. A., Chavrier, F., Crum, L. A., and Vaezy, S. (2005). Gel phantom for use in high-intensity focused ultrasound dosimetry. *Ultrasound in Medicine and Biology*, 31:1383–1389.

Leighton, T. G. (1994). *The Acoustic Bubble*. Academic Press, San Diego.

Lide, D. R., editor (2003–2004). *CRC Handbook of Chemistry and Physics*. CRC Press, 84th edition.

Lide, D. R., editor (2007). *CRC handbook of chemistry and physics, internet version 2007* <*http://www.hbcpnetbase.com*>. Taylor and Francis, Boca Raton, FL, 87th edition.

Liebler, M., Dreyer, T., and Riedlinger, R. E. (2006). Nonlinear modeling of interactions between ultrasound propagation and cavitation bubbles. *Acta Acustica United with Acustica*, 92(1):165–167.

Lin, H., Storey, B. D., and Szeri, A. J. (2002). Inertially driven inhomogeneities in violently collapsing bubbles: the validity of the Rayleigh–Plesset equation. *Journal of Fluid Mechanics*, 452:145–162.

Lingeman, J. E. (1996). Extracorporeal shock wave lithotripsy devices: Are we making progress? In Lingeman, J. E. and Preminger, G. M., editors, *New Developments in the Management of Urolithiasis*, pages 79–96. Igaku-Shoin, New York.

Lofstedt, R., Barber, B. P., and Putterman, S. J. (1993). Toward a hydrodynamic theory of sonoluminescence. *Physics of Fluids A—Fluid Dynamics*, 5(11):2911–2928.

Loyalka, S. K. and Ferziger, J. H. (1968). Model Dependence of the Temperature Slip Coefficient. *Physics of Fluids*, 11(8):1668–1671.

MacDonald, J. R. (1966). Some Simple Isothermal Equations of State. *Reviews of Modern Physics*, 38(4):669–679.

Matsumoto, Y., Allen, J. S., Yoshizawa, S., Ikeda, T., and Kaneko, Y. (2005). Medical ultrasound with microbubbles. *Experimental Thermal and Fluid Science*, 29:255–265.

Matsumoto, Y. and Takemura, F. (1994). Influence of internal phenomena on gas bubble motion (effects of thermal-diffusion, phase-change on the gas-liquid interface and mass diffusion between vapor and noncondensable gas in the collapsing phase). *JSME International Journal Series B—Fluids and Thermal Engineering*, 37:288–296.

Matsumoto, Y. and Yoshizawa, S. (2005). Behaviour of a bubble cluster in an ultrasound field. *International Journal for Numerical Methods in Fluids*, 47:591–601.

Matula, T. J., Hilmo, P. R., Bailey, M. R., and Crum, L. A. (2002a). In vitro sonoluminescence and sonochemistry studies with an electrohydraulic shock-wave lithotripter. *Ultrasound in Medicine and Biology*, 28(9):1199–1207.

Matula, T. J., Hilmo, P. R., Storey, B. D., and Szeri, A. J. (2002b). Radial response of individual bubbles subjected to shock wave lithotripsy pulses *in vitro*. *Physics of Fluids*, 14(3):913–921.

McAteer, J. A., Bailey, M. R., Williams Jr., J. C., Cleveland, R. O., and Evan, A. P. (2005). Strategies for improved shock wave lithotripsy. *Minerva Urologica e Nefrologica*, 57(4):271–287.

Moss, W. C. (1997). Understanding the periodic driving pressure in the Rayleigh-Plesset equation. *Journal of the Acoustical Society of America*, 101(2):1187–1190.

Moss, W. C., Levatin, J. L., and Szeri, A. J. (2000). A new damping mechanism in strongly collapsing bubbles. *Proceedings of the Royal Society of London Series A*, 456:2983–2994.

Neppiras, E. A. (1980). Acoustic cavitation. *Physics Reports—Review Section of Physics Letters*, 61(3):159–251.

Nigmatulin, R. I., Khabeev, N. S., and Nagiev, F. B. (1981). Dynamics, heat and mass transfer of vapour-gas bubbles in a liquid. *International Journal of Heat and Mass Transfer*, 24(6):1033–1044.

Othmer, D. F. and Thakar, M. S. (1953). Correlating Diffusion Coefficient in Liquids. *Industrial and Engineering Chemistry*, 45(3):589–593.

Parlitz, U., Mettin, R., Luther, S., Akhatov, I., Voss, M., and Lauterborn, W. (1999). Spatio-temporal dynamics of acoustic cavitation bubble clouds. *Philosophical Transactions of the Royal Society of London Series A*, 357:313–334.

Pearle, M. S., Calhoun, E. A., and Curhan, G. C. (2005). Urologic diseases in america project: urolithiasis. *Journal of Urology*, 173(3):848–857.

Pishchalnikov, Y. A., McAteer, J. A., Kreider, W., Williams Jr., J. C., Pishchalnikova, I. V., and Bailey, M. R. (2007). Influence of cavitation on lithotripter shock waves. In Calvo-Manzano, A., Perez-Lopez, A., and Santiago, J. S., editors, *Proceedings of the 19th International Congress on Acoustics, Madrid, Spain, September 2–7, 2007*, pages 1–6, paper NLA–02–005–IP.

Pishchalnikov, Y. A., Neucks, J. S., VonDerHaar, R. J., Pishchalnikova, I. V., Williams Jr., J. C., and McAteer, J. A. (2006). Air pockets trapped during routine coupling in dry head lithotripsy can significantly decrease the delivery of shock wave energy. *Journal of Urology*, 176(6 Pt 1):2706–2710.

142

Pishchalnikov, Y. A., Sapozhnikov, O. A., Bailey, M. R., Pishchalnikova, I. V., Williams Jr., J. C., and McAteer, J. A. (2005). Cavitation selectively reduces the negative-pressure phase of lithotripter shock pulses. *Acoustics Research Letters Online*, 6:280–286.

Pishchalnikov, Y. A., Sapozhnikov, O. A., Bailey, M. R., Williams Jr., J. C., Cleveland, R. O., Colonius, T., Crum, L. A., Evan, A. P., and McAteer, J. A. (2003a). Cavitation bubble cluster activity in the breakage of kidney stones by lithotripter shockwaves. *Journal of Endourology*, 17:435–446.

Pishchalnikov, Y. A., Sapozhnikov, O. A., Bailey, M. R., Williams Jr., J. C., Cleveland, R. O., Colonius, T., Crum, L. A., Evan, A. P., and McAteer, J. A. (2003b). Cavitation bubble cluster activity in the breakage of kidney stones by lithotripter shockwaves. *Journal of Endourology*, 17:435–446.

Plesset, M. and Prosperetti, A. (1977). Bubble dynamics and cavitation. *Annual Review of Fluid Mechanics*, 9:145–85.

Plesset, M. S. and Chapman, R. B. (1971). Collapse of an initially spherical vapour cavity in the neighbourhood of a solid boundary. *Journal of Fluid Mechanics*, 47pt2:283–290.

Plesset, M. S. and Hsieh, D. Y. (1960). Theory of gas bubble dynamics in oscillating pressure fields. *Physics of Fluids*, 3(6):882–892.

Plesset, M. S. and Zwick, S. A. (1952). A nonsteady heat diffusion problem with spherical symmetry. *Journal of Applied Physics*, 23(1):95–98.

Plesset, M. S. and Zwick, S. A. (1954). The growth of vapor bubbles in superheated liquids. *Journal of Applied Physics*, 25(4):493–500.

Poliachik, S. L., Chandler, W. L., Ollos, R. J., Bailey, M. R., and Crum, L. A. (2004). The relation between cavitation and platelet aggregation during exposure to high-intensity focused ultrasound. *Ultrasound in Medicine and Biology*, 30(2):261–269.

Poling, B. E., Prausnitz, J. M., and O'Connell, J. P. (2001). *The properties of gases and liquids*. McGraw-Hill.

Poritsky, H. (1952). The collapse or growth of a spherical bubble or cavity in a viscous fluid. In Sternberg, E., editor, *Proceedings of the First U.S. National Congress on Applied Mechanics, New York*, pages 813–821.

Preston, A. T. (2004). *Modeling Heat and Mass Transfer in Bubbly Cavitating Flows and Shock Waves in Cavitating Nozzles*. PhD thesis, California Institute of Technology, Pasadena, California.

Prosperetti, A. (2004). Bubbles. *Physics of Fluids*, 16:1852–1865.

Prosperetti, A., Crum, L. A., and Commander, K. W. (1988). Nonlinear bubble dynamics. *Journal of the Acoustical Society of America*, 83(2):502–514.

Prosperetti, A. and Lezzi, A. (1986). Bubble dynamics in a compressible liquid. Part 1. First-order theory. *Journal of Fluid Mechanics*, 168:457–478.

Qin, S. P., Hu, Y. T., and Jiang, Q. (2006). Oscillatory interaction between bubbles and confining microvessels and its implications on clinical vascular injuries of shock-wave lithotripsy. *IEEE Transactions on Ultrasonics, Ferroelectrics, and Frequency Control*, 53(7):1322–1329.

Rabkin, B. A. (2004). *High-Intensity Focused Ultrasound (HIFU) Induced Hyperechoic Regions for the Ultrasound Guidance of HIFU Therapy*. PhD thesis, University of Washington.

Rabkin, B. A., Zderic, V., Crum, L. A., and Vaezy, S. (2006). Biological and physical mechanisms of hifu-induced hyperecho in ultrasound images. *Ultrasound in Medicine and Biology*, 32(11):1721–1729.

Rabkin, B. A., Zderic, V., and Vaezy, S. (2005). Hyperecho in ultrasound images of hifu therapy: Involvement of cavitation. *Ultrasound in Medicine and Biology*, 31:947–956.

Rayleigh, L. (1917). On the pressure developed in a liquid during the collapse of a spherical cavity. *Philosophical Magazine*, 34:94–98.

Reid, R. C. and Sherwood, T. K. (1966). *The properties of gases and liquids*. McGraw-Hill, New York, 2nd edition.

Rozenberg, L. D., editor (1971). *High-Intensity Ultrasonic Fields*, pages 201–259. Plenum Press, New York. Part IV, "Pulsations of Cavitation Voids," by V. A. Akulichev.

Sankin, G. N., Simmons, W. N., Zhu, S. L., and Zhong, P. (2005). Shock wave interaction with laser-generated single bubbles. *Physical Review Letters*, 95(3):034501.

Sapozhnikov, O., Kreider, W., Bailey, M. R., Khokhlova, V. A., and Curra, F. (2008). Effect of elastic waves in the metal reflector on bubble dynamics at the focus of an electrohydraulic lithotripter. To be presented at Acoustics'08 (joint meeting of ASA, EAA, SFA), June 29–July 4, 2008, Paris, France.

Sapozhnikov, O. A., Bailey, M. R., and Crum, L. A. (1999). Shot-to-shot variability of acoustic axis of a spark-source lithotripter. *Journal of the Acoustical Society of America*, 105:1269. (Abstract for presentation at the 137th Meeting of the Acoustical Society of America).

144

Sapozhnikov, O. A., Khokhlova, V. A., Bailey, M. R., Williams Jr., J. C., McAteer, J. A., Cleveland, R. O., and Crum, L. A. (2002). Effect of overpressure and pulse repetition frequency on cavitation in shock wave lithotripsy. *Journal of the Acoustical Society of America*, 112(3):1183–1195.

Sapozhnikov, O. A., Maxwell, A. D., MacConaghy, B., and Bailey, M. R. (2007). A mechanistic analysis of stone fracture in lithotripsy. *Journal of the Acoustical Society of America*, 121(2):1190–1202.

Sharipov, F. and Kalempa, D. (2005). Velocity slip and temperature jump coefficients for gaseous mixtures. iv. temperature jump coefficient. *International Journal of Heat and Mass Transfer*, 48(6):1076–1083.

Silverberg, P. M. and Wenzel, L. A. (1965). The variation of latent heat with temperature. *Journal of Chemical and Engineering Data*, 10(4):363–366.

Storey, B. D. and Szeri, A. J. (1999). Mixture segregation within sonoluminescence bubbles. *Journal of Fluid Mechanics*, 396:203–221.

Storey, B. D. and Szeri, A. J. (2000). Water vapour, sonoluminescence and sonochemistry. *Proceedings of the Royal Society of London Series A*, 456:1685–1709.

Storey, B. D. and Szeri, A. J. (2001). A reduced model of cavitation physics for use in sonochemistry. *Proceedings of the Royal Society of London Series A*, 457:1685–1700.

Szeri, A. J., Storey, B. D., Pearson, A., and Blake, J. R. (2003). Heat and mass transfer during the violent collapse of nonspherical bubbles. *Physics of Fluids*, 15(9):2576–2586.

Takemura, F. and Matsumoto, Y. (1994). Influence of internal phenomena on gas bubble motion - (effects of transport phenomena and mist formation inside bubble in the expanding phase). *JSME International Journal Series B—Fluids and Thermal Engineering*, 37:736–745.

Tanguay, M. (2004). *Computation of bubbly cavitating flow in shock wave lithotripsy.* PhD thesis, California Institute of Technology, Pasadena, CA.

Toegel, R., Gompf, B., Pecha, R., and Lohse, D. (2000). Does water vapor prevent upscaling sonoluminescence? *Physical Review Letters*, 85(15):3165–3168.

Toegel, R. and Lohse, D. (2003). Phase diagrams for sonoluminescing bubbles: A comparison between experiment and theory. *Journal of Chemical Physics*, 118(4):1863–1875.

Tran, B. C., Seo, J., Hall, T. L., Fowlkes, J. B., and Cain, C. A. (2003). Microbubble-enhanced cavitation for noninvasive ultrasound surgery. *IEEE Transactions on Ultrasonics, Ferroelectrics, and Frequency Control*, 50(10):1296–1304.

Vaezy, S., Shi, X. G., Martin, R. W., Chi, E., Nelson, P. I., Bailey, M. R., and Crum, L. A. (2001). Real-time visualization of high-intensity focused ultrasound treatment using ultrasound imaging. *Ultrasound in Medicine and Biology*, 27:33–42.

van Iersel, M. M., Cornel, J., Benes, N. E., and Keurentjes, J. T. F. (2007). Inhibition of nonlinear acoustic cavitation dynamics in liquid co2. *Journal of Chemical Physics*, 126(6):064508.

Vogel, A. and Lauterborn, W. (1988). Acoustic transient generation by laser-produced cavitation bubbles near solid boundaries. *Journal of the Acoustical Society of America*, 84(2):719–731.

Vogel, A., Lauterborn, W., and Timm, R. (1989). Optical and acoustic investigations of the dynamics of laser-produced cavitation bubbles near a solid boundary. *Journal of Fluid Mechanics*, 206:299–338.

Vuong, V. Q. and Szeri, A. J. (1996). Sonoluminescence and diffusive transport. *Physics of Fluids*, 8(9):2354–2364.

Wagner, W. and Pruß, A. (2002). The IAPWS formulation 1995 for the thermodynamic properties of ordinary water substance for general and scientific use. *Journal of Physical and Chemical Reference Data*, 31(2):387–535.

Weisstein, E. W. (2007a). Divergence theorem, from MathWorld—a Wolfram web resource. URL: http://mathworld.wolfram.com/DivergenceTheorem.html.

Weisstein, E. W. (2007b). Leibniz integral rule, from MathWorld—a Wolfram web resource. URL: http://mathworld.wolfram.com/LeibnizIntegralRule.html.

Wu, F., Wang, Z.-B., Cao, Y.-D., Xu, Z.-L., Zhou, Q., Zhu, H., and Chen, W.-Z. (2006). Heat fixation of cancer cells ablated with high-intensity focused ultrasound in patients with breast cancer. *American Journal of Surgery*, 192(2):179–184.

Xi, X. F. and Zhong, P. (2000). Improvement of stone fragmentation during shock-wave lithotripsy using a combined EH/PEAA shock-wave generator—in vitro experiments. *Ultrasound in Medicine and Biology*, 26(3):457–467.

Xu, Z., Fowlkes, J. B., Rothman, E. D., Levin, A. M., and Cain, C. A. (2005). Controlled ultrasound tissue erosion: The role of dynamic interaction between insonation and microbubble activity. *Journal of the Acoustical Society of America*, 117:424–435.

Xu, Z., Ludomirsky, A., Eun, L. Y., Hall, T. L., Tran, B. C., Fowlkes, J. B., and Cain, C. A. (2004). Controlled ultrasound tissue erosion. *IEEE Transactions on Ultrasonics, Ferroelectrics, and Frequency Control*, 51(6):726–736.

146

Yang, X. M. and Church, C. C. (2005). Nonlinear dynamics of gas bubbles in viscoelastic media. *Acoustics Research Letters Online*, 6:151–156.

Yang, X. M., Roy, R. A., and Holt, R. G. (2004). Bubble dynamics and size distributions during focused ultrasound insonation. *Journal of the Acoustical Society of America*, 116:3423–3431.

Yasui, K. (1995). Effects of thermal conduction on bubble dynamics near the sonoluminescence threshold. *Journal of the Acoustical Society of America*, 98:2772–2782.

Yasui, K. (1996). Variation of liquid temperature at bubble wall near the sonoluminescence threshold. *Journal of the Physical Society of Japan*, 65(9):2830–2840.

Yasui, K. (1997). Alternative model of single-bubble sonoluminescence. *Physical Review E*, 56:6750–6760.

Yasui, K. (2001). Effect of liquid temperature on sonoluminescence. *Physical Review E*, 64:Art. No. 016310.

Young, F. R. (1976). Sonoluminescence from water containing dissolved gases. *Journal of the Acoustical Society of America*, 60(1):100–104.

Zarnitsyn, V. G., Prausnitz, A. R., and Chizmadzhev, Y. A. (2004). Physical methods of nucleic acid delivery into cells and tissues. *Biologicheskie Membrany*, 21:355–373.

Zderic, V., Brayman, A. A., Sharar, S. R., Crum, L. A., and Vaezy, S. (2006). Microbubble-enhanced hemorrhage control using high intensity focused ultrasound. *Ultrasonics*, 45(1-4):113–120.

Zhong, P. and Zhou, Y. F. (2001). Suppression of large intraluminal bubble expansion in shock wave lithotripsy without compromising stone comminution: Methodology and in vitro experiments. *Journal of the Acoustical Society of America*, 110(6):3283–3291.

Zhong, P., Zhou, Y. F., and Zhu, S. L. (2001). Dynamics of bubble oscillation in constrained media and mechanisms of vessel rupture in swl. *Ultrasound in Medicine and Biology*, 27(1):119–134.

Zhou, Y. F. and Zhong, P. (2006). The effect of reflector geometry on the acoustic field and bubble dynamics produced by an electrohydraulic shock wave lithotripter. *Journal of the Acoustical Society of America*, 119(6):3625–3636.

Appendix A

CALCULATION OF FLUID PROPERTIES

In the succeeding sections, the equations used to calculate fluid properties are stated. For convenience, a number of pertinent constants are cited in Table A.1 for use throughout.

Table A.1. Fluid Constants

Constant	Value	Units
Boltzmann constant (k_B)	$1.3806503 \times 10^{-23}$	$J/^\circ K$
universal gas constant $(\mathcal{R})$	8.314472	$J/(mol\,^\circ K)$
Avogadro's constant (N_A)	$6.02214179 \times 10^{23}$	$1/mol$
from Wagner and Pruß[99]		
critical pressure, water (P_c)	22.064	MPa
critical volume, water (V_c)	55.95×10^{-6}	m^3/mol
critical temperature, water (T_c)	647.096	$^\circ K$
triple point, water (T_{melt})	273.16	$^\circ K$
boiling point, water (T_{boil})	373.12	$^\circ K$
from Poling et al.[63]		
molecular weight, water (M_{H_2O})	18.015	g/mol
molecular weight, air (M_{air})	28.97	g/mol
hard-sphere diameter, water (d_{H_2O})	2.641×10^{-10}	m^3
hard-sphere diameter, air (d_{air})	3.711×10^{-10}	m^3
second virial coefficient, water (b_{vap})	$\frac{2}{3}\pi N_A d_{H_2O}^3$	m^3/mol
second virial coefficient, air (b_{air})	$\frac{2}{3}\pi N_A d_{air}^3$	m^3/mol
Lennard-Jones parameter, water (ϵ_0/k_B)	809.1	$^\circ K$
Lennard-Jones parameter, air (ϵ_0/k_B)	78.6	$^\circ K$

A.1   Vapor Pressure of Water

The saturated vapor pressure of water varies as a function of temperature. In the context of the present model, the vapor pressure is calculated from the liquid temperature T as

follows:[99]

$$p_{sat} = P_c \exp\left(\frac{a_1\tau + a_2\tau^{1.5} + a_3\tau^3 + a_4\tau^{3.5} + a_5\tau^4 + a_6\tau^{7.5}}{T_r}\right) \qquad (A.1)$$

where all temperatures are in units of °K and the calculated pressure is in Pa. The reduced temperatures T_r and τ along with the constants a_i are defined as follows:

$$T_r = \frac{T}{T_c} \quad \begin{vmatrix} a_1 = -7.85951783 \\ a_2 = 1.84408259 \\ a_3 = -11.7866497 \end{vmatrix} \begin{matrix} a_4 = 22.6807411 \\ a_5 = -15.9618719 \\ a_6 = 1.80122502 \end{matrix}$$
$$\tau = 1 - T_r$$

This correlation for vapor pressure is valid anywhere on the vapor-liquid phase boundary, from the triple point at T_{melt} to the critical point at T_c. For any temperatures outside this range, vapor transport is taken to be identically zero and p_{sat} need not be evaluated.

A.2   Latent Heat of Vaporization of Water

The latent heat associated with evaporation and/or condensation of water can be expressed as the following function of temperature:[100]

$$\mathcal{L} = 4400.74 \left[\frac{9}{5}(T_c - T)\right]^{0.358} \qquad (A.2)$$

where the liquid temperature T is in °K and $\mathcal{L}$ is in J/mol.

A.3   Density of Liquid Water

The density of water in the liquid phase is in general a function of temperature and pressure. However, it is convenient to split these dependencies into an isothermal relation for density (*i.e.*, a form of the Tait equation) and an isobaric relation. The isothermal relation is used in the Gilmore equation for the radial dynamics of the bubble and accounts for compressibility effects near the bubble. In contrast,the isobaric relation is useful for calculating variations in density at atmospheric pressure as the ambient temperature changes.

The isobaric relation is actually a formula developed to estimate density along the liquid-vapor saturation curve. According to the international standard set forth by Wagner and

Pruß,[99] saturation density can be calculated for temperature T as follows:

$$\rho = \frac{M_{H_2O}}{V_c} \left(1 + b_1\tau^{1/3} + b_2\tau^{2/3} + b_3\tau^{5/3} + b4\tau^{16/3} + b_5\tau^{43/3} + b_6\tau^{110/3}\right) \qquad \text{(A.3)}$$

$$
\begin{array}{l|l|l}
T_r = \frac{T}{T_c} & b_1 = 1.99274064 & b_4 = -1.75493479 \\
\tau = 1 - T_r & b_2 = 1.09965342 & b_5 = 45.5170352 \\
& b_3 = -0.510839303 & b_6 = -6.74694450 \times 10^5
\end{array}
$$

The isothermal relation for density is based upon a Tait equation of state. By inverting Equation (2.11), density as a function of pressure is expressed as[62]

$$\rho = \rho_0 \left[1 + \frac{\Gamma}{\rho_0^2 c_0^2}(p - p_0)\right]^{1/\Gamma} \qquad \text{(A.4)}$$

Here the reference state defined by p_0 and ρ_0 can be estimated from the above relation for density along the saturation curve. The Tait exponent $\Gamma = 6.5$ is an empirically defined constant, while the reference sound speed (c_0) at a given temperature completes the formulation. From referenced data,[62] this relation is valid across a range of pressures from 0.1–1180 MPa and is used as a liquid equation of state in the description of the radial dynamics from Section 2.2.1.

A.4 Sound Speed in Liquid Water

For the Tait equation defined in the previous section, it is necessary to define an equilibrium sound speed as a function of temperature. To this end, a correlation valid for liquid water at 1 atm and for temperatures between 273 and 373°K is utilized:[101,102]

$$c_0 = a_0 + a_1\tau + a_2\tau^2 + a_3\tau^3 + a_4\tau^4 + a_5\tau^5 \qquad \text{(A.5)}$$

$$
\begin{array}{l|l}
\tau = T - T_{melt} & \\
a_0 = 1.40238744 \times 10^3 & a_3 = 3.34638117 \times 10^{-4} \\
a_1 = 5.03836171 & a_4 = -1.48259672 \times 10^{-6} \\
a_2 = -5.81172916 \times 10^{-2} & a_5 = 3.16585020 \times 10^{-9}
\end{array}
$$

where the reference temperature T is in °K.

A.5 Surface Tension of Water

The surface tension of water is considered to be a function of temperature only. At high pressures, surface tension may change; however, the makeup of the pressurizing gas and its dissolution at the surface would have to be accounted for under these conditions, making any estimation of surface tension very difficult. An alternate approach is to assume that surface tension vanishes at supercritical temperatures that are consistent with high gas pressures inside the bubble during collapse. Such an assumption is reasonable given that typical measurements under pressurized conditions indicate a reduction in surface tension.[103] As a function of temperature alone, the following correlation is used at temperatures less than T_c:[104]

$$\sigma = 0.2358 \left(1 - \frac{T}{T_c}\right)^{1.256} \left[1 - 0.625\left(1 - \frac{T}{T_c}\right)\right] \tag{A.6}$$

where σ has units of N/m.

A.6 Viscosity of Liquid Water

The viscosity of liquid water is typically calculated as a function of temperature and pressure. From Kestin and Whitelaw,[105] a correlation is available for temperatures and pressures within the respective ranges $T_{melt} < T < 573.15$°K and $p_{sat} < p < 80$ MPa, where p_{sat} is the saturated vapor pressure at the liquid temperature T. For temperatures or pressures outside of the prescribed range, an effective value at the range boundary is assumed. This correlation may be written as

$$\mu = 2.414(10^{-5})\, 10^{247.8/(T-140)} \left[1 + 1.04673(10^{-11})\,(p - p_{sat})(T - 305)\right] \tag{A.7}$$

where the units of μ are Pa·s. Note that the viscosity relative to the bubble is evaluated at the liquid-gas interface, where the pressure $p = p_w$ is related to the pressure inside the bubble by Equation (2.29).

A.7 Solubility of Air in Water

The dissolution of a gas in a liquid is governed by Henry's law as defined by Equation (2.17). From this definition, we seek to calculate the solubility of air in water as a function of temperature. Variations in Henry's constant with pressure are ignored. Based on the correlated data of Eichelberger,[106] solubility at 20 MPa is overestimated by about 30% when atmospheric pressure is assumed; the impact of such overestimation will be minimal for a collapsing bubble since mass diffusion occurs on a much slower time scale than bubble motion. The correlation presented by Battino et al.[106] can be expressed as

$$\mathcal{H} = \frac{\rho_w}{101.325\, M_{H_2O}} \exp\left(A + B/\tau + C\ln\tau + D\tau\right) \tag{A.8}$$

where ρ_w indicates the liquid density at the bubble wall in kg/m^3, $\tau = T_w/100$ in units of $^\circ$K, and the units for $\mathcal{H}$ are mol/(m^3 Pa). The alphabetical constants are given by

$$A = -104.208 \quad B = 137.296 \quad C = 58.7394 \quad D = -5.7669$$

This correlation is applicable for temperatures between T_{melt} and T_{boil}; for temperatures outside this range, the correlation is evaluated at an effective temperature taken to be the boundary of the aforementioned range.

A.8 Thermal Conductivity of Liquid Water

Following Kestin and Whitelaw,[105] we calculate the thermal conductivity of water as a function of both temperature T and pressure p. The valid ranges for this correlation are $T_{melt} < T_w < 623^\circ$K and $p_{sat} < p_w < 50$ MPa. As done for other properties, values falling outside of this range are pinned at the range boundary before use in the correlation. Considering a normalized tmeperature $\tau = T/T_{melt}$ and a pressure difference $p' = p - p_{sat}$ in units of bars, the correlation is

$$k_L = \sum_{i=0}^{4} a_i \tau^i + p' \sum_{i=0}^{3} b_i \tau^i + (p')^2 \sum_{i=0}^{3} c_i \tau^i \tag{A.9}$$

where k_L is in units of W/m °K and the alphabetic constants are

$$
\begin{array}{lll}
a_0 = -0.92247 & b_0 = -9.4730 \times 10^{-4} & c_0 = 1.6563 \times 10^{-6} \\
a_1 = 2.8395 & b_1 = 2.5186 \times 10^{-3} & c_1 = -3.8929 \times 10^{-6} \\
a_2 = -1.8007 & b_2 = -2.0012 \times 10^{-3} & c_2 = 2.9323 \times 10^{-6} \\
a_3 = 0.52577 & b_3 = 5.1536 \times 10^{-4} & c_3 = -7.1693 \times 10^{-7} \\
a_4 = -0.073440
\end{array}
\tag{A.10}
$$

Although an enhancement of thermal conductivity occurs near the critical region, the above correlation will not capture such enhancement given the ranges of validity stated above.

A.9 Heat Capacity of Liquid Water

A correlation for heat capacity is available from the National Institute of Standards and Technology.[107] The correlation is in the form of a Shomate equation and is applicable over a temperature range from 298–500°K as a standard. Here, we use the correlation from T_{melt} to 500°K and evaluate the correlation at these limits for temperatures outside this range. The Shomate equation for water is expressed as

$$
c_{pL} = \left(A + B\tau + C\tau^2 + D\tau^3 + \frac{E}{\tau^2} \right) \frac{1000}{M_{H_2O}}
\tag{A.11}
$$

where c_{pL} is in units of J/kg °K and the alphabetical constants are

$$
\begin{array}{lll}
A = -203.6060 & C = -3196.413 & E = 3.855326 \\
B = 1523.290 & D = 2474.455
\end{array}
\tag{A.12}
$$

A.10 Diffusivity of Air in Liquid Water

The diffusivities of gases in liquids are generally correlated with the liquid viscosity. As with viscosity, relevant methods for estimating diffusivities depend upon both temperature and pressure. Here we use the following equation from Othmer and Thakar:[108]

$$
\mathcal{D} = \frac{1.4 \times 10^{-8}}{mu^{1.1} V_{air}^{0.6}}
\tag{A.13}
$$

where μ is the viscosity evaluated by Equation (A.7) in units of centipoise. In addition, V_{air} is the molar volume of air in cm^3/mol, which is taken to be 29.9 from Reid and Sherwood.[103] The above relation for diffusivity is an empirical correlation and is used here over a temperature range from 283–363°K. Temperatures outside this range are accordingly pinned at the limits of this range.

A.11 Diffusivity among Gas Species

As opposed to the diffusion of gases dissolved in liquids, diffusion among gas species also occurs. At low densities, a diffusion coefficient for two ideal gases can be derived from kinetic theory.[63,65] While this approach accounts for the impact of temperature, it does address changes in density of the gases. Because bubbles can achieve high gas pressures and densities during collapse, it is of interest to address the impact of density. To this end, a high-density correction based on Chapman-Enskog theory is used.[109]

The low-density estimate can be expressed as

$$\mathcal{D}'_{12} = \left(\frac{8k_B T}{\pi m}\right)^{1/2} \frac{3}{32\,\rho_m\,N_A\,d^2\Omega_D} \tag{A.14}$$

where k_B is the Boltzmann constant, N_A is Avogadro's number, T is temperature in °K, ρ_m is the molar density of the entire gas mixture, and Ω_D is a collision integral discussed below. In addition, m and d represent averaged properties of molecular mass and diameter and are calculated as

$$
\begin{aligned}
m &= \frac{M_{H_2O} M_{air}}{M_{H_2O} + M_{air}} \frac{1}{N_A} \\
d &= \frac{1}{2}\left(d_{air} + d_{H_2O}\right)
\end{aligned}
$$

The high-density correction can then be calculated as

$$\mathcal{D}_{1}2 = \frac{\mathcal{D}'_{12}}{Y_{12}} \tag{A.15}$$

where Y_{12} is is estimated from the molar vapor fraction f_v as

$$Y_{12} = 1 + \frac{2}{3}\rho_m N_A f_v d_{H_2O}^3 \left(\frac{d_{H_2O} + 4d_{air}}{4d_{H_2O} + 4d_{air}}\right) + \frac{2}{3}\rho_m N_A (1 - f_v) d_{air}^3 \left(\frac{4d_{H_2O} + d_{air}}{4d_{H_2O} + 4d_{air}}\right) \quad \text{(A.16)}$$

A.12 Thermal Conductivity of an Air-Water Vapor Mixture

To estimate the thermal conductivity of an air-vapor mixture, we follow several references to account for variations with both temperature (T) and density (ρ_m). First, we follow Yasui[110] and define low-density conductivities as linear functions of temperature:

$$k'_{air} = \alpha_{air}T + \beta_{air} \quad \text{where } \alpha_{air} = 5.39 \times 10^{-5}, \ \beta_{air} = 0.0108$$

$$k'_{vap} = \alpha_{vap}T + \beta_{vap} \quad \text{where } \alpha_{vap} = 9.98 \times 10^{-5}, \ \beta_{vap} = -0.0119$$

In these relations, T is in °K and the low-density thermal conductivities (k') have units of W/m°K. Using a quadratic mixing rule[63] and considering a mixture with a mole fraction of vapor f_v, the low-density conductivity of the mixture is

$$k'_{mix} = \left[f_v\sqrt{k'_{vap}} + (1 - f_v)\sqrt{k'_{air}}\right]^2 \quad \text{(A.17)}$$

Adjustment for high density concentrations is formulated in terms of the second virial coefficient b of the gas mixture.[109] Using a mixing rule from Poling et al.,[63] we have

$$b = b_{air}(1 - f_v)^2 + 2b_{av}(1 - f_v)f_v + b_{vap}f_v^2 \quad \text{(A.18)}$$

where $b_{av} = \frac{2}{3}\pi N_A d^3$ and d is defined in the previous section. Using this relation for the second virial coefficient, the thermal conductivity k_g is calculated from the following equations:

$$y = b\rho_m + 0.625(b\rho_m)^2 + 0.2869(b\rho_m)^3 + 0.115(b\rho_m)^4$$

$$k_g = k'_{mix}\left[b\rho_m\left(1/y + 1.2 + 0.755\,y\right)\right]$$

where ρ_m is the molar density of the mixture.

A.13 Heat Capacity of Air-Water Vapor Mixture

The heat capacity at constant volume of a gas can be derived from the kinetic theory of ideal gases.[65] Moreover, the heat capacity of a mixture can calculated as a mole-fraction average of the values for each type of gas. For polyatomic gases, kinetic theory implies that the specific heat is proportional to the universal gas constant $\Re$. Including translational and vibrational energies of polyatomic molecules, the specific heat can be written in terms of temperature T as

$$c_v' = \Re \left[A + \sum_m \frac{(\theta_m/T)^2 \, e^{\theta_m/T}}{(e^{\theta_m/T} - 1)^2} \right] \tag{A.19}$$

where $A = 5/2$ for linear molecules or $A = 3$ for nonlinear molecules and θ_m represents temperatures associated with one or more vibrational modes. Here, we consider an air-vapor mixture so that the molecular properties of oxygen, nitrogen, and water are considered. As linear molecules, nitrogen and oxygen have a single vibrational mode; as a nonlinear molecule, water possesses three modes. The pertinent vibrational temperatures are provided below:

	θ_m (°K)		
nitrogen	3393		
oxygen	2273		
water	2295	5255	5400

Moreover, considering a vapor fraction f_v and air as 78.5% nitrogen and 21.5% oxygen, the specific heat (c_v) of the mixture is calculated as a weighted average of the c_v' as calculated with the above formula. In additioan , we recognize that for an ideal gas, $c_p = c_v + \Re$. Hence, the ratio of specific heats can be written as $\gamma = \frac{c_p}{c_v} = 1 + \frac{\Re}{c_v}$

A.14 Diffusion Collision Integral

A diffusion collision integral Ω_D based on Lennard-Jones potentials is used above in Section A.11 for the diffusivity among gas species. This integral is approximated with the following expression:[63]

$$\Omega_D = \frac{A}{\tau^B} + \frac{C}{e^{D\tau}} + \frac{E}{e^{F\tau}} + \frac{G}{e^{H\tau}} \tag{A.20}$$

where τ is a normalized temperature. The temperature T is normalized by the molecular property ϵ_0/k_B such that

$$\tau = \frac{k_B\,T}{\epsilon_0}$$

Here, k_B is the Boltzmann constant while ϵ_0 represents a minimum energy of attraction.[103] While ϵ_0/k_B is tabulated for specific gases, the corresponding value for a two-component mixture can be calculated as

$$\epsilon_0/k_B = [(\epsilon_{01}/k_B)(\epsilon_{02}/k_B)]^{1/2}$$

Lastly, the alphabetic constants from Equation (A.20) are

$A = 1.06036$	$D = 0.47635$	$G = 1.76474$
$B = 0.15610$	$E = 1.03587$	$H = 3.89411$
$C = 0.19300$	$F = 1.52996$	

Appendix B

MEASUREMENTS OF INDIVIDUAL SHOCK WAVES

The material included in this appendix was submitted to *The Journal of the Acoustical Society of America* in January 2008 for publication.[97] At present, the manuscript remains under review. The title was 'Beamwidth measurement of individual lithotripter shock waves,' while the authors were listed as Wayne Kreider, Michael R. Bailey, and Jeffrey A. Ketterling. The manuscript comprised the contents of this appendix in addition to an abstract and acknowledgments.

B.1   Introduction

Shock wave lithotripsy (SWL) is the most common treatment for uncomplicated renal stones.[111] Several recent studies have reported that when compared to outcomes with the original Dornier HM3 electrohydraulic lithotripter, new lithotripters have lower stone-free rates, increased re-treatment rates, and increased severity and frequency of trauma to surrounding tissue.[112-115] The differences in clinical outcomes may relate to the method of acoustic coupling to the patient (newer machines utilize a water filled pillow while the HM3 utilizes a water bath).[94] However, it is generally accepted that the tigher focal geometries and higher peak pressures of the newer machines have had great impact on clinical outcomes. More specifically, tissue injury is known to correlate with peak pressure, while the efficacy of targeting stones is likely reduced for shock waves with narrower focal regions.[116] Moreover, experiments have also found that lithotripters with focal regions that are wide relative to the stone (*e.g.*, the HM3) produce more effective stone fragmentation. The utility of a broad focal beamwidth lies in the ability of a shock wave traveling along the stone perimeter to generate shear waves within the stone.[117-119] In response to clinical outcomes and experimental results, many manufacturers have released new lithotripters specifically marketed as 'broad-focus.'

The inherent shock-to-shock variability of the acoustic field in spark-source, electro-hydraulic lithoptripters makes it very difficult to characterize instantaneous beamwidths. Typically, beamwidths are estimated from the sequential acquisition of point measurements within the focal plane using single-element hydrophones. However, shock waves change significantly due to variations in spark energy and in location of the spark between the electrodes.[120] These variabilities can alter the waveform shape in terms of rise time and pulse width. Moreover, the location of the focal region may shift. Accordingly, the combination of single-element hydrophone measurements from a series of different shock waves may yield broader estimates of beamwidth than are actually present. Given the clinical motivation described above for knowing the shock-wave beamwidth in lithotripsy, improved measurement tools are needed.

In this work, a linear array hydrophone was constructed and used to make instantaneous beamwidth measurements of individual lithotripter shock waves. Measurements were made with broad- and narrow-focus electrohydraulic lithotripters as well as with new and worn electrodes at different charging potentials. The different conditions tested were designed to ensure variability in both focal beamwidths and peak pressures.

B.2 Methods

B.2.1 Hydrophone Array

The linear hydrophone array utilized in these studies was fabricated using a technique described by Ketterling et al.[121] The array consisted of a 9 μm polyvinylidene fluoride (PVDF) membrane with one side electroded with gold (Ktech Corp., Albuquerque, NM) and the other bonded to a copper-clad polyimide (CCP) film (RFlex 1000L810, Rogers Corp., Chandler, AZ) using a thin layer of non-conductive epoxy. The epoxy layer typically remains about 1 μm thick after curing. The actual array pattern was etched onto the CCP using standard printed circuit board techniques. Electrical trace lines linking each element to a connection pad were also etched onto the CCP and the trace pads were spaced to fit into a standard zero-insertion force (ZIF) flex connector. During the bonding process, the films were clamped between two aluminum plates. After the bonding epoxy cured, a Teflon

mold of 15 mm depth was attached to the back of the membranes and filled with additional epoxy. The operating characteristics (*e.g.*, center frequency, bandwidth, etc.) of a device similar to the linear array are described by Ketterling et al.

The electrical and mechanical characteristics of the linear array were designed to span a distance greater than the −6 dB beamwidth of the HM3 geometry with a sufficient number of elements to resolve spatial variation in the focal beam. Moreover, the surface area of each element was chosen to be sufficiently high for impedance matching considerations. The final assembled linear array consisted of 20 elements, each 4 mm long by 0.5 mm wide, as illustrated in Fig. B.1. The center-to-center element spacing was 0.9 mm for a total array width of 17.6 mm. A custom printed circuit board linked the ZIF connector to 20 BNC connectors. The 20 elements were connected to the inputs of six digital oscilloscopes via BNC cables with no preamplification.

Given the design details described above, it is instructive to consider expected operational characteristics of the hydrophone array. Since the bandwidth of PVDF is greater than 70 MHz, shock fronts with rise times of at least 14 ns can theoretically be resolved. However, angular misalignment of the array with the shock front will effectively average the shock over the element surface and increase its apparent rise time. For example, a 5 degree inclination of the 4 mm long elements would lead to an apparent 200-ns rise time for a planar shock wave. In addition, averaging across the 0.5 mm width of each element will occur due to misalignment as well as spatial variability across the beamwidth of the shock wave. Such transverse averaging should remain relatively small since the width of each element is much less than its length and is only about 3% of the −6 dB beamwidth for the HM3 reflector geometry.[82]

B.2.2 SWL Measurements

Measurements were made in degassed water with the hydrophone array placed at the focus of the APL-UW research lithotripter modeled after the Dornier HM3.[82] The array was oriented at the focus such that the 4×0.5 mm area of each element was approximately perpendicular to the axis of propagation of the shock wave. Moreover, the array was centered such that
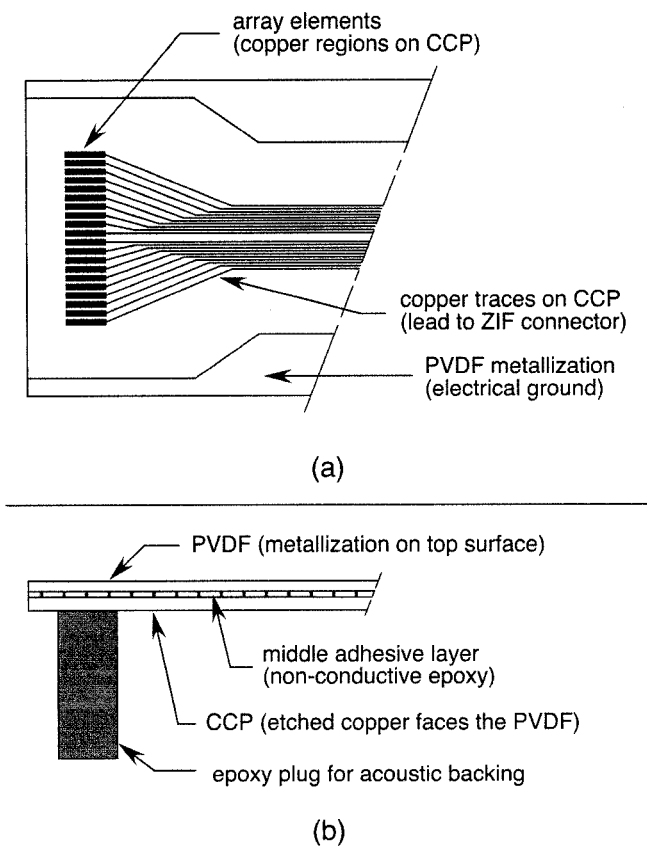
array elements
(copper regions on CCP)

copper traces on CCP
(lead to ZIF connector)

PVDF metallization
(electrical ground)

(a)

PVDF (metallization on top surface)

middle adhesive layer
(non-conductive epoxy)

CCP (etched copper faces the PVDF)

epoxy plug for acoustic backing

(b)

Figure B.1. Schematic of the hydrophone array in (a) plan view and (b) elevation view. Note that only the array elements are strictly drawn to scale. The array consisted of 20 PVDF elements that were 0.5 mm by 4 mm, with a center-to-center element spacing of 0.9 mm.

the middle elements were aligned at the geometric focus of the lithotripter. A charging potential of 15, 18, or 23 kV was used to trigger single shock waves at a rate slower than one per minute. Two ellipsoidal reflectors were used: an HM3-style reflector (semimajor and semiminor axes: $a = 13.80$ cm, $b = 7.75$ cm) and a reflector insert that fit inside the HM3-style reflector ($a = 9.30$, $b = 6.24$). Both reflectors were axisymmetric in that they did not possess cutouts to accommodate fluoroscopy that typically exist in clinical lithotripters. The reflector insert was designed to create a tighter focus, as illustrated in Fig. B.2. New electrodes ($<$ 200 shock waves) and worn electrodes at the end of their prescribed clinical lifetime ($>$ 2000 shock waves) were used. Worn electrodes possessed larger spark gaps and
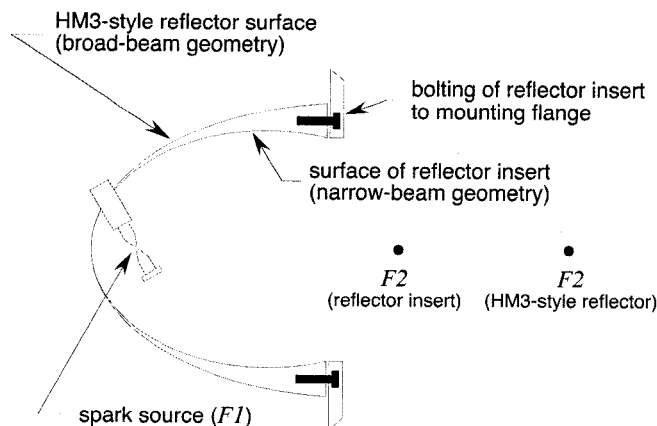
Figure B.2. Scaled drawing of the lithotripter geometries tested. The ellipsoidal reflectors possess two foci, where $F1$ denotes the focus corresponding to the spark source and $F2$ denotes the remote focus corresponding to the treatment site and the central location at which beamwidth measurements were acquired.

exhibited damage caused by arcing along a broad portion of their surface. As mentioned above, testing with both new and worn electrodes ensured variability in the focal pressures.

Voltage measurements from the array elements were captured on six digital oscilloscopes with sampling rates of at least 50 MHz. Measurements were collected using an input impedance of 1 MΩ on the oscilloscopes and no preamplification. A custom LabVIEW program (National Instruments, Austin, TX) was used to digitally store select waveforms. Oscilloscope measurements corresponding to peak positive pressures of the focal wave were manually recorded for all array elements. For select shock waves, oscilloscope settings were adjusted to resolve the peaks corresponding to the direct wave (*i.e.,* the spherically diverging wave generated by the spark that precedes the focal wave).

Measurements were analyzed in two steps. First, given that the direct wave diverges spherically from the spark at one focus of the ellipsoidal reflector, the relative amplitude of the direct wave as experienced by each array element was calculated from geometric considerations. Considering that the array width was 17.6 mm and the distance from the spark to the nearest measurement location was 138 mm, the amplitude of the direct wave varied across the width of the array by no more than 0.2%. Next, the direct-wave measurements
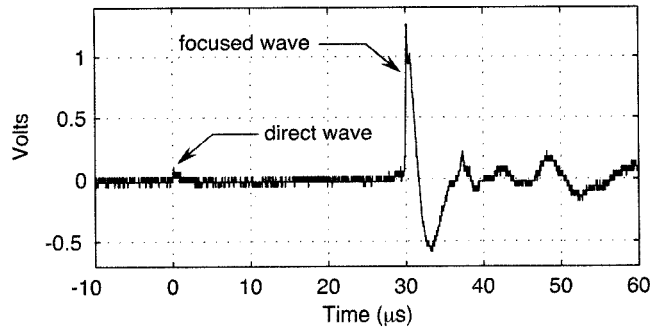
Figure B.3. Measured direct and focal shock waves from a single array element.

were used to normalize measurements of the focal wave on an element-by-element basis. In this manner, variations in the sensitivity of each element were accounted for, thereby enabling quantitative measurement of the relative pressure amplitude of individual shock waves across the focal width of the lithotripter. Although not measured explicitly in this effort, absolute pressures for the Dornier HM3 reflector have been measured previously. For this geometry, the maximum peak positive amplitudes have been reported to be about 1 MPa for the direct wave and 29.9±4.7 MPa for the focused wave.[82] The ratio of these reported amplitudes can be directly compared to the data presented below for the HM3-style reflector.

B.3 Results

An example of a waveform measured on a single element of the array hydrophone while using the HM3-style reflector and new electrode is shown in Fig. B.3. The sensitivity of the hydrophone array was sufficient to reveal the direct wave seen at $t = 0$ as well as the focused wave at $t \approx 30$ μs. The measured focal waveforms show a peak positive spike of about 1 μs duration followed by a negative trough of about 4 μs, which is the commonly described classic lithotripter waveform.[82,120] The shock front was slightly rounded and not strongly shocked. As discussed above, misalignment of the array such that the elements are not perpendicar to the acoustic axis and parallel to the shock front is a likely explanation for the slow rise times observed.
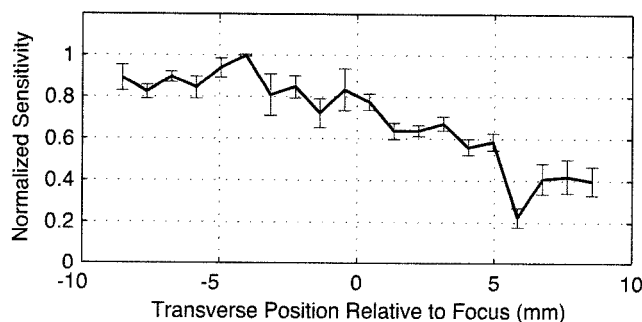
Figure B.4. Normalized element sensitivities. The thick line indicates the element-by-element mean of measurements from 6 shock waves, while the vertical bars indicate ±1 standard deviation at each element.

In order to resolve the direct waveforms across the array elements, alternate oscilloscope settings were used to acquire data at 18 and 23 kV charging potentials for the HM3-style reflector and at 15 and 18 kV for the reflector insert. While element sensitivities were consistent for measurements from both reflector geometries, one element appeared to become damaged during acquisition of direct-wave measurements with the reflector insert. Accordingly, direct-wave measurements with the HM3-style reflector were normalized relative to the most sensitive element for each shock wave. These normalized responses for six separate shock waves were then averaged. As illustrated in Fig. B.4, element sensitivities tended to decrease across the width of the array. Possible explanations for this behavior include different cabling impedances among elements and/or other variables in the fabrication process. Because only a single prototype of the array was constructed, issues of fabrication consistency were not investigated in this effort.

After correcting for individual element sensitivities as described above, the beam profiles of individual shock waves are presented in Fig. B.5. Because all measurements are normalized relative to the direct wave from the HM3-style reflector at 18 kV, the plotted amplitudes can be directly compared. As shown, measured profiles are sorted based on the test conditions used to generate shock waves. Focused beams were produced using four distinct combinations of either the HM3-style or the insert reflector, a charging potential of

18 kV or 23 kV, and new or worn electrodes. In Fig. B.5(a), the -6 dB beamwidth of the profile corresponding to the thickest line is explicitly marked and labeled. Note that the array element at a transverse position of -0.45 mm (as labeled by the dashed circle) consistently measured lower pressures than its neighbors in all profiles. Accordingly, this element was ignored in the estimation of beamwidths. Since it is possible that damage or bubbles could transiently alter element sensitivity, the lower reading might have been corrected if each element were normalized to the simultaneously measured direct wave rather than the profile displayed in Fig. B.4. However, simultaneous measurement of the direct and focal waves would require oscilloscopes capable of capturing longer time traces and resolving a larger dynamic range.

Each of the profiles plotted in Fig. B.5 was used to estimate the -6 dB beamwidth and the transverse location of the peak pressure. These data for independently measured shock waves are provided in Table B.1, in which 'Range' denotes the extent of the range of measurements as the difference between the maximum and minimum values. Comparing the four separate groups of shock-wave measurements, several key differences are apparent. First, from test conditions (a) and (b), the insert reflector produced narrower beamwidths, higher peak pressures, and a more consistent localization of the peak pressure than did the HM3-style reflector. In Table B.1, the range of zero for peak pressure locations indicates that the peak was measured at the same element for all shock waves. Moreover, despite measuring a low number of shock waves, the beamwidths measured for conditions (a) and (b) are statistically different at a 95% confidence level ($p \approx 0.04$). Considering conditions (b), (c), and (d) for the HM3-style reflector, worn electrodes altered the shape of the beam profiles and generated slightly higher peak pressures than new electrodes at a charging potential of 18 kV.

At a charging potential of 23 kV with new electrodes, the HM3-style reflector tended to produce higher peak pressures than at 18 kV, as expected. However, shock waves generated at 23 kV also exhibited much greater variability as indicated by the plotted profiles as well as by the reported 14.4 mm range for peak pressure locations. Assuming that the measured locations of peak pressure are normally distributed, the variances of the distributions corresponding to conditions (b) and (d) are different with a statistical confidence level of
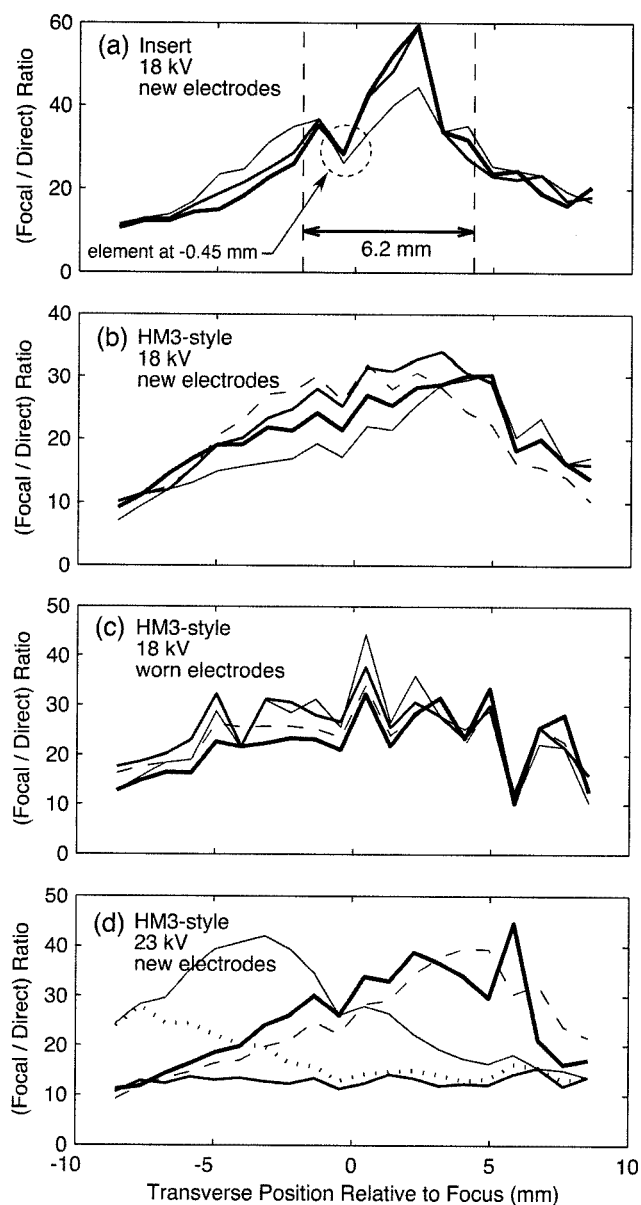
Figure B.5. Beam profiles measured for individual shock waves. Shock waves were generated using (a) the reflector insert, a charging potential of 18 kV, and new electrodes [3 shock waves]; (b) the HM3-style reflector, 18 kV, and new electrodes [4 shock waves]; (c) the HM3-style reflector, 18 kV, and worn electrodes [4 shock waves]; and (d) the HM3-style reflector, 23 kV, and new electrodes [5 shock waves]. Note that direct-wave measurements at 18 kV were used for all normalizations, thereby allowing direct comparison of the amplitudes in all plots. The −6 dB beamwidth of the thickest-line profile is marked in (a).

Table B.1. Measurements from individual shock waves.

Conditions	Beamwidth (mm)		Peak Location (mm)
	Mean	Range*	Range*
(a) Insert reflector 18 kV, new electrodes [3 shock waves]	8.1	6.3	0.0
(b) HM3-style reflector 18 kV, new electrodes [4 shock waves]	13.1	2.6	5.4
(c) HM3-style reflector 18 kV, worn electrodes [4 shock waves]	11.9	4.5	5.4
(d) HM3-style reflector 23 kV, new electrodes [5 shock waves]	12.4	6.9	14.4

*Denotes the extent of the range of observed measurements as given by the maximum value minus the minimum.

89%. This result again demonstrates that the array can be used to discern system variability based on only a few shock wave measurements. In this case, higher charging potential affected the repeatability of the location of peak pressure.

In addition to the above comparisons among test conditions used in this effort, measurements with the HM3-style reflector can also be compared to data derived from single-point hydrophone measurements. The −6 dB beamwidth of the HM3-style reflector was previously reported to be about 14 mm.[82,120] Under all conditions tested in this effort, the beamwidths were 1–2 mm less than the previously reported value for the HM3-style reflector. Although this discrepancy may not be statistically significant, these observations are consistent with the expectation that averaging of single-point measurements from multiple shock waves leads to an overestimation of beamwidth. Aside from beamwidth, Cleveland et al.[82] used a single-point hydrophone to measure peak positive pressures of 29.9±4.7 MPa at 18 kV for the device used in this effort. Assuming a direct-wave amplitude of 1 MPa as mentioned in Section B.2.2, the expected range of normalized peak pressures from 25–35 is confirmed by the profiles in Fig. B.5(b).

The primary focus of this effort was to explore the use of a novel hydrophone array for
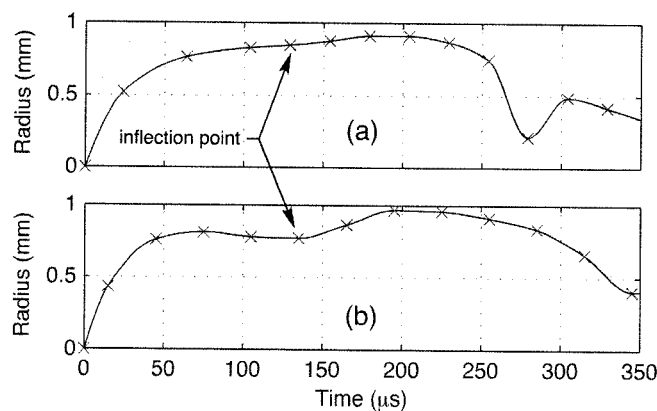
Figure B.6. Radius-time curves showing representative bubble behaviors when excited by shock waves corresponding to (a) the HM3-style reflector and (b) the reflector insert.

single-shot measurements of lithotripter shock waves. One particular use of this array in lithotripsy research is to enable quick and accurate comparisons of the beamwidths produced by various reflector geometries. In acquiring such measurements for the HM3-style and insert reflectors in this effort, a noteworthy observation was made regarding the behavior of cavitation bubbles. To document this observation, high-speed photographs of bubbles excited by shock waves from both reflector geometries were captured. Radius-time curves for a typical bubble corresponding to each reflector were generated from the photographs[122] and are presented in Fig. B.6. For both reflectors, the bubbles go through a prolonged growth and collapse phase that lasts hundreds of microseconds after the focal shock wave has passed. Considering shock-wave arrival at $t = 0$, both radius-time curves possess a point of inflection at about $t = 130$ μs. Because such inflection points are typical, the consistent presence of a secondary expansion wave can be inferred.

While the radius-time curves corresponding to each reflector are qualitatively similar, it appears that the secondary expansion wave was considerably stronger for the more highly focused reflector. The secondary bubble growth starting at about 130 μs was more prominent and the overall collapse time was nearly a hundred microseconds longer with the narrow-beamwidth reflector. Although the origin of the secondary waves has not been explicitly investigated, such waves may arise from the excitation of elastic waves in the reflectors. Ul-

timately, the observed difference in bubble behavior highlights the potential for unintended consequences when explicitly attempting to manipulate the acoustic field through the reflector geometry. Because both beamwidth and cavitation dynamics are affected, caution should be exercised when comparing the relative bioeffects induced by different reflector geometries.

B.4   Discussion and Conclusions

The linear hydrophone array proved to be a useful tool for quickly and accurately measuring the beamwidths of focused shock waves. The measurements presented above represent the first simultaneous acoustic field measurements in an electrohydraulic lithotripter. Previous measurements consisted of point measurements at a single spatial location for each shock wave. Using 20 elements, the beam profiles measured with the array were relatively smooth. Although some variabilities persisted after compensation for the sensitivities of individual elements, the instantaneous measurements did enable at least a qualitative distinction of the acoustic fields generated under different test conditions. Notably, the beamwidths of the HM3-style and the insert reflectors were determined to be statistically different after acquiring measurements from only a few shock waves.

While spark jitter did not strongly affect the observed focal locations for either reflector geometry at a charging potential of 18 kV, considerably more scatter in the focal locations was found at 23 kV for the HM3-style reflector. The good repeatability is consistent with previous measurements using the fountain produced by the shock wave on this lithotripter at 18 kV.[123] The focal-zone variability at 23 kV is qualitatively consistent with high-speed camera images of cavitation clouds in other electrohydraulic lithotripters.[93] Beyond the explicit effects of spark jitter, shock-wave propagation through tissue inhomogeneities and/or cavitation clouds may affect the ultimate location of the focal region under clinical conditions. Scattering associated with such random variations in the propagation path has been demonstrated to reduce the amplitudes of portions of the focal waveforms.[14,94,124] However, it is not known if the scattered energy is refocused elsewhere in the tissue. Given such persistent questions regarding the spatial characteristics of lithotripter shock waves, hydrophone arrays promise to be a useful tool for instantaneous measurement of focal location

and beamwidth.

The prototype hydrophone array designed and fabricated in this effort proved fairly consistent and robust. Although not mechanistically explained, the element sensitivities reported in Fig. B.4 were repeatably observed. One apparent inconsistency in the measurements was the questionably low readings yielded by the element at -0.45 mm (even after applying the sensitivity correction). With regard to robustness, another element stopped functioning after approximately 100 shock waves. The damage is presumed to have been caused by cavitation. In addition, it is speculated that the aforementioned inconsistency and perhaps other measurement variabilities were caused by the collection of cavitation bubbles on the hydrophone's surface. Modifications of the array to include a protective coating or immersion in oil might be useful to improve the consistency and robustness of the device. As a final comment on array design, the fabrication technique allows adjustment of the number of elements, the element size, and the element spacing for optimal performance in a given lithotripter.

VITA

After growing up in Delaware, Wayne Kreider attended Virginia Tech in Blacksburg, Virginia. At Virginia Tech, he earned B. S. and M. S. degrees from the Department of Engineering Science and Mechanics (1993, 1995). After this initial stint in graduate school, he worked as an engineer at the Naval Surface Warfare Center (1996–1997; Dahlgren, VA) and at Dominion Engineering, Inc. (1997–2001; Reston, VA). While at Dominion Engineering, he became a licensed professional engineer in the Commonwealth of Virginia (2000, Mechanical Engineering). In 2008, he earned a Doctor of Philosophy at the University of Washington in Bioengineering.